



# LUND UNIVERSITY

## Performance Limits for Microstrip Patch Antennas

Nel, Ben

2025

*Document Version:*

Publisher's PDF, also known as Version of record

[Link to publication](#)

*Citation for published version (APA):*

Nel, B. (2025). *Performance Limits for Microstrip Patch Antennas*. Department of Electrical and Information Technology, Lund University.

*Total number of authors:*

1

### General rights

Unless other specific re-use rights are stated the following general rights apply:

Copyright and moral rights for the publications made accessible in the public portal are retained by the authors and/or other copyright owners and it is a condition of accessing publications that users recognise and abide by the legal requirements associated with these rights.

- Users may download and print one copy of any publication from the public portal for the purpose of private study or research.
- You may not further distribute the material or use it for any profit-making activity or commercial gain
- You may freely distribute the URL identifying the publication in the public portal

Read more about Creative commons licenses: <https://creativecommons.org/licenses/>

### Take down policy

If you believe that this document breaches copyright please contact us providing details, and we will remove access to the work immediately and investigate your claim.

LUND UNIVERSITY

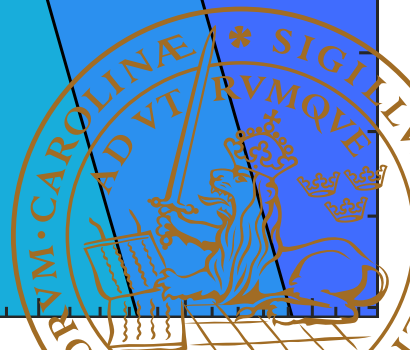
PO Box 117  
221 00 Lund  
+46 46-222 00 00





# Performance Limits for Microstrip Patch Antennas

BEN ABRAHAM PIETER NEL  
DEPARTMENT OF ELECTRICAL AND INFORMATION TECHNOLOGY  
FACULTY OF ENGINEERING | LTH | LUND UNIVERSITY



# Performance Limits for Microstrip Patch Antennas

Doctoral Thesis

*Ben Abraham Pieter Nel*



**LUND**  
UNIVERSITY

Department of Electrical and  
Information Technology  
Lund, February 2025

Ben Abraham Pieter Nel  
Department of Electrical and Information Technology  
Electromagnetics and Nanoelectronics  
Lund University  
Ole Römers Väg 3, 223 63 Lund, Sweden

Series of licentiate and doctoral theses  
ISSN: 1654-790X, No.182  
ISBN: 978-91-8104-356-3 (print)  
ISBN: 978-91-8104-357-0 (pdf)

©2025 Ben Nel, except where otherwise stated.  
Typeset in Computer Modern 10 pt using  $\text{\LaTeX}$  and  $\text{\BibTeX}$ .  
Printed by Tryckeriet i E-huset, Lund University, Lund, Sweden.

No part of this thesis may be reproduced or transmitted in any form or by any means without written permission from the author. Distribution of the original thesis in full, however, is permitted without restriction.

Vir *Oupa*



# Abstract



ICROSTRIP patch antennas have become essential in modern communication systems due to their compact size and ease of fabrication. However, their performance is often constrained by narrow bandwidth, low radiation efficiency, and low gain, especially in miniaturized designs. The performance limits of microstrip patch antennas are helpful in understanding and overcoming these challenges. These performance limits are determined for three key metrics in this thesis, Q-factor (which is inversely proportional to bandwidth), radiation efficiency, and gain. Limits on these metrics provide insights into the maximum achievable performance for these antennas, guiding the design process beyond traditional optimization methods.

The performance bounds are determined through a current optimization approach, utilizing a method of moment implementation. This implementation makes use of specific Green's functions for layered media, determined using Sommerfeld integrals. This approach ensures that only the currents within the region where the patch is designed are required. Additionally, the currents are restricted to only components parallel to the ground plane, further refining the optimization process.

The results demonstrate that these theoretical bounds closely match the performance of traditional microstrip patch antenna designs in terms of Q-factor, radiation efficiency, and gain. Additionally, the derived Q-factor bounds are shown to be orders of magnitude tighter than the classical Chu limit for microstrip patch antennas. A central focus of this thesis is the balance between the electrical and/or physical size of the design region and performance. It explores whether enhancing radiation efficiency in miniaturized antennas is more effectively achieved by increasing the dielectric substrate between the patch and ground plane's relative permittivity or by refining the patch's geometry.

To make the presented bounds more accessible to a larger part of the antenna design community, this thesis introduces simple scaling rules. These rules allow designers to approximate lower Q-factor bounds using standard simulation tools. Additionally, by utilizing a new connection between Q-factor and radiation efficiency, the scaling rules are extended to estimate bounds on radiation efficiency

as well. This approach translates complex theoretical insights into easy-to-use practical guidelines. The established relationship between lower Q-factor bounds and maximum radiation efficiency opens up new possibilities in antenna design. In specific scenarios, this relationship can improve the design process and simplify measurements by allowing one parameter to be inferred from the other.

A crucial part of understanding the Q-factor is the concept of stored energy. This thesis connects the stored energy in radiating systems to derivatives of the reactive power and/or dissipated power with respect to background material properties. More specifically, the stored electric energy is linked to the derivative with respect to permittivity, and stored magnetic energy is linked to the derivative with respect to permeability. Through this, a link between material losses and stored energies in radiating systems is established. This provides physical insights into stored energies and how they affect the performance of microstrip patch antennas.

Finally, this thesis investigates the use of a metasurface combined with an infrared camera as a method for imaging radio frequency fields. The measurement setup relies on the heat dissipated on metasurface elements due to the field from the device under test. A better understanding of this design setup requires an investigation into the effect of the metasurface elements on the measurement. This is done by simulating different metasurface element designs and assessing how their dissipated power correlates with the field in the absence of the metasurface.

# Popular Science Summary



LECTROMAGNETIC waves are all around us. We can easily see some of them when they manifest as light and color, but it is far less intuitive to understand how we manipulate the invisible ones at lower frequencies. Antennas engineered to transmit and receive these signals are built into our smartphones, each type serving a specific purpose. Unlike visible light, we cannot directly observe how these antennas work, so their effectiveness must be judged through precise, objective measures tied to their data transfer capabilities. This thesis explores the fundamental limits of a particular class of antennas called microstrip patch antennas, revealing how well they can perform under certain design constraints.

Microstrip patch antennas are widely used for their versatility and compact design. Much like musical instruments that produce sound by exciting resonances/oscillations, in the case of microstrip patch antennas, resonances lead to electromagnetic radiation as opposed to sound. These antennas are used in numerous electronic systems, from mobile phones to satellites, owing in part to their compatibility with existing technologies such as printed circuits.

Despite their widespread use, achieving high performance in microstrip patch antenna design remains challenging. To help overcome this, traditional optimization methods can benefit from leveraging fundamental physical limits on antenna performance. Without these performance limits or a starting design that satisfies the requirements, designers face the daunting task of searching through an infinite design space without knowing whether their goals are even achievable. This thesis addresses these challenges by introducing a systematic approach to determine fundamental performance limits of microstrip patch antennas, enabling more focused and efficient design strategies.

The motion of charged particles (electrons) often leads to the emission of photons as electromagnetic waves, forming the basis of antenna operation. This electron movement creates electrical currents along the antenna. Consequently, understanding antenna performance depends on examining how its current distribution affects its ability to radiate efficiently. By identifying the optimal current distribution within a specific design area, this thesis establishes theoretical

performance limits for microstrip patch antennas. It highlights the trade-offs between the size of the design region and the achievable performance. That the optimal currents are achievable through a realistic design is not guaranteed. However, it is shown that practical designs can often approach these theoretical limits, effectively bridging the gap between idealized performance and real-world performance.


This thesis investigates three critical performance metrics for microstrip patch antennas: Q-factor, radiation efficiency, and gain. Bounds on these metrics define the antenna's capabilities and provide benchmarks for practical designs. The first metric, the Q-factor, is related to the antenna's bandwidth (the range of frequencies it can receive or transmit effectively). A lower Q-factor corresponds to a wider bandwidth, enabling higher data rates. This thesis establishes a lower bound for the Q-factor, demonstrating how material properties and stored energy influence bandwidth. The second metric, radiation efficiency, measures the proportion of input power converted into useful radiation, with the thesis providing a maximum achievable efficiency for these antennas. The thesis also reveals a previously unexplored relationship between radiation efficiency and bandwidth, offering insights for future designs. Lastly, the gain metric is explored, which measures the antenna's ability to focus its radiated power in a specific direction. The maximum gain for microstrip patch antennas is calculated, setting an upper limit on how well these antennas can direct input power.

Together, these performance bounds provide a clearer understanding of what microstrip patch antennas can achieve, offering new perspectives on the trade-offs when considering bandwidth, efficiency, and gain. The findings not only help improve existing designs but also pave the way for smarter, more compact, and efficient antennas, addressing the increasing demands of modern communication systems.

A crucial part of understanding the Q-factor and, thus, the bandwidth of an antenna is the concept of stored energy. Think of it like a compressed spring, holding energy that can later be released or the mechanical energy not dissipated in a vibrating string. This thesis connects, in the case of microstrip patch antennas, the stored energy to the properties of the materials surrounding the antennas, providing deeper physical insights into the antenna performance.

Finally, this thesis also explores how electromagnetic waves from a radiating device can be measured using a surface. Similar to electromagnetic radiation from the sun and how it heats up our skin, the electromagnetic field from the radiating device heats up the surface. The change in temperature on the surface (metasurface) can be imaged using an infrared camera. Since the heat change on the metasurface is proportional to the strength of the electromagnetic field, this can be correlated to the electromagnetic field distribution. The metasurface design is critical, as it affects how the surface converts the electromagnetic field to heat. This thesis compares the power absorbed by the metasurface to the expected power from the device, thus assessing the potential of the method and providing valuable insights into improving how electromagnetic fields are measured and understood in practical applications.

# Acknowledgments

 I would like to thank my main supervisor, Mats Gustafsson, for offering me this opportunity and for guidance and wisdom throughout this journey. Your feedback and encouragement have been pivotal in shaping my research. To my co-supervisor, Anja Skrivervik, your expertise and support, whether near or from afar, have added depth and clarity to my work; thank you also for the warm hospitality during my visit to EPFL, I thoroughly enjoyed it.

I would like to thank my co-supervisor, Johan Lundgren, for your keen eye for detail and excellent input into the structure and language of this thesis, which has significantly improved its quality. Beyond that, your support in helping me settle in during my early days in Sweden made all the difference, I am truly grateful. Further, I want to thank my co-supervisor, Daniel Sjöberg, for your continued support. Then, to my Master's thesis supervisor at Stellenbosch University, Matthys Botha, I am grateful for the introduction you provided to my research.

To the funding agencies who have made my research at Lund University possible, I would like to thank the Swedish Research Council and the Excellence Center at Linköping–Lund in Information Technology (ELLIIT). Further, I would also like to thank the Royal Physiographic Society of Lund for funding the NVIDIA A100 Tensor Core GPU for my research.

I would also like to thank my colleagues at EIT, whose support and camaraderie have made this journey all the more fulfilling. In no particular order, Saketh Ram Mamidala, thank you for the many good memories both at EIT organizing events as PhD representatives and your eagerness for after-work activities. Then, Hannes Dahlberg, your adventurous spirit and positive approach to life have really rubbed off on me. Thank you, Paula Wich-Glasen. Your presence at the office is such a breath of fresh air, and our road trips together are always fun. Also, I would like to thank Karthik Ram Mamidala and Gautham Rangasamy, our shared love of cricket has led to a more enjoyable working environment. Then, André Andersen, our thought-provoking discussions are greatly valued. Thank you, Marcus Sandberg, for the many lunchtime discussions. Neharika Valecha, thank you for your humor and for ensuring my birthday was

celebrated with a delicious home-baked cake.

Thank you also to the Lund University Rice Box team, Elias, Linus, and Oskar, for our first place in the AP-S student design contest. It was fun.

To the new colleagues in the EMN division who have made a significant impression in the short time we have known each other, I would like to thank Davide, Erik, Philip, Simon, Johan, and Avinas. Further, a big thank you to all the colleagues from EIT for all the chats over coffee and lunch. Thank you, Duc, Mattias, Lars, Anders, Erik, Anette, Louise, Alexandros, Lars-Erik, Niklas, Zhongyunshen, Ufuk, Guoda, Anton, Stefan, Adam, Abinaya, Christer, Michiel, Lasse, Heera, Navya, Patrik, Ilayda, Buon, Christian, Hanieh, Yuyan, Qiuyan, Philipp, Karl-Magnus, Johannes, Hedieh, and Robin.

For my stay at EPFL and other collaborative work with the MAG group, I would like to thank Ismael Triviño for helping me with measurements and Hannes Bartle for not only supporting me with my measurements but also teaching me to ski. I am also grateful to Erik for making my time in Lausanne more enjoyable.

To all the friends outside of work who have made my time in Lund thoroughly enjoyable, thank you so much! Then, I would like to thank my family and, especially my brother, for contributing to my competitive spirit. A heartfelt thanks to my grandfather for sharing his fascination with electromagnetic waves with me at an early age. Last, but not least, I would like to thank my loving mother for her unwavering support and encouragement.

Lund, February 2025



*Ben Abraham Pieter Nel*



# Contents

<b>Abstract</b>	<b>v</b>
<b>Popular Science Summary</b>	<b>vii</b>
<b>Acknowledgments</b>	<b>ix</b>
<b>Contents</b>	<b>xii</b>
<b>Preface</b>	<b>xv</b>
Structure of the Thesis . . . . .	xv
List of Included Papers . . . . .	xv
Related Work . . . . .	xvi
<b>Acronyms and Symbols</b>	<b>xix</b>
Acronyms and Abbreviations . . . . .	xix
Latin Symbols . . . . .	xx
Greek Symbols . . . . .	xxi
 <b>INTRODUCTION</b>	 <b>1</b>
<b>1 Background and Motivation</b>	<b>3</b>
<b>2 Microstrip Patch Antennas</b>	<b>7</b>
<b>3 Cavity Model</b>	<b>9</b>
<b>4 Method of Moments</b>	<b>11</b>
4.1 Layered Green’s Functions and Sommerfeld Integrals . . . . .	13
4.2 Singularity when Determining the Self Integral . . . . .	14

4.3	Interpreting the Impedance Matrix of Microstrip Patch Antennas	16
4.4	Radiation Efficiency and Gain . . . . .	17
4.5	Radiated Power for Microstrip Patch Antennas . . . . .	18
4.6	Ratio of Surface Wave Power to Radiated Power . . . . .	19
4.7	Q-factor . . . . .	20
4.8	Stored Energies . . . . .	21
4.9	Stored Energies of Microstrip Patch Antennas . . . . .	22
<b>5</b>	<b>Material Parameters and Stored Energies</b>	<b>25</b>
5.1	Relating Q-factor to Radiation Efficiency . . . . .	25
5.2	Material Derivatives and Stored Energies . . . . .	26
<b>6</b>	<b>Physical Limits on Antennas</b>	<b>33</b>
6.1	Quadratically Constrained Quadratic Program . . . . .	34
6.2	Maximum Radiation Efficiency . . . . .	35
6.3	Maximum Self-resonant Radiation Efficiency . . . . .	36
6.4	Lower Bounds on Q-factor . . . . .	37
6.5	Maximum Gain . . . . .	38
<b>7</b>	<b>Microstrip Patch Antenna Bounds Results</b>	<b>39</b>
7.1	Lower Q-factor Bounds . . . . .	39
7.2	Maximum Radiation Efficiency . . . . .	43
7.3	Maximum Gain . . . . .	46
<b>8</b>	<b>Metasurface Element Designs for Infrared-Based Antenna Measurements</b>	<b>47</b>
<b>9</b>	<b>Summary and Future Work</b>	<b>53</b>
	<b>Bibliography</b>	<b>57</b>
	<b>PAPERS</b>	<b>67</b>
<b>I</b>	<b>Q-factor Bounds for Microstrip Patch Antennas</b>	<b>69</b>
<b>II</b>	<b>Radiation Efficiency and Gain Bounds for Microstrip Patch Antennas</b>	<b>99</b>
<b>III</b>	<b>Stored Energies and Q-factor Expressed in Material Derivatives</b>	<b>127</b>
<b>IV</b>	<b>Impact of Metasurface Element Designs on Infrared-Based Antenna Near-Field Measurements</b>	<b>141</b>



# Preface



HIS thesis is the culmination of five years of work in the Electromagnetics and Nanoelectronics (EMN) division at Lund University and investigates performance limits of microstrip patch antennas. The work was supervised by Prof. Mats Gustafsson, and co supervised by Prof. Anja K Skrivervik, Asst. Prof. Johan Lundgren, and Prof. Daniel Sjöberg.

## STRUCTURE OF THE THESIS

This thesis consists of a collection of research papers with an introductory section providing broader context and perspective.

- **INTRODUCTION**

The main body of the thesis is the published papers appended at the back. The introduction provides context and a broader view than the focused publications.

- **PAPERS**

The published papers form the main body of the thesis and are appended in the back.

## INCLUDED PAPERS

- I. Ben A. P. Nel, Anja K. Skrivervik and Mats Gustafsson, “Q-Factor Bounds for Microstrip Patch Antennas”, *IEEE Transactions on Antennas and Propagation*, Vol. 71, No. 4, pp. 3430 - 3440, IEEE, 2023.

**Contributions of the author:** I am the main contributor to this paper, having written code, performed simulations, and wrote the paper.<sup>1</sup>.

---

<sup>1</sup>This paper was presented in IEEE “WHAP: What’s Hot in Antennas and Propagation?”. Watch this on the IEEE Transactions on Antennas and Propagation **YouTube channel**

- II. Ben A. P. Nel, Anja K. Skrivervik and Mats Gustafsson, “Radiation Efficiency and Gain Bounds for Microstrip Patch Antennas”, *IEEE Transactions on Antennas and Propagation*, Early Access, 2024.

**Contributions of the author:** I am the main contributor to this paper, writing code, performing simulations, and I wrote the paper. I was actively involved in fabricating the H-shaped patch and the measurement setup while at EPFL.

- III. Ben A. P. Nel, Anja K. Skrivervik and Mats Gustafsson, “Stored Energies and Q-factor expressed in Material derivatives”, *IEEE Antennas and Wireless Propagation Letters*, Vol. 23, No. 1, pp. 19-23, IEEE, 2024.

**Contributions of the author:** I am the main contributor of this paper. I conceptualized using material derivatives as outlined in the paper, and I wrote the paper.

- IV. Ben A. P. Nel, Anja K. Skrivervik, Johan Lundgren and Mats Gustafsson, “Impact of Metasurface Element Designs on Infrared-Based Antenna Near-Field Measurements”, *19th European Conference on Antennas and Propagation (EuCAP 2025)*, accepted.

**Contributions of the author:** I am the main contributor of the paper. I ran the simulations, and I wrote the paper.

## RELATED WORK

The author of this dissertation is also the author or co-author of the following publications and scientific work, which are related to but not considered part of the dissertation:

- V. Ben A. P. Nel and Mats Gustafsson, “Elementwise Constraints for Tighter Antenna Bounds”, *15th European Conference on Antennas and Propagation (EuCAP 2021)*, Düsseldorf, Germany, 22 to 26 March 2021.
- VI. Ben A. P. Nel, Anja K. Skrivervik and Mats Gustafsson, “Minimum Q-factor for Microstrip Antennas”, *16th European Conference on Antennas and Propagation (EuCAP 2022)*, Madrid, Spain, 27 March to 1 April 2022.
- VII. Ben A. P. Nel, Anja K. Skrivervik and Mats Gustafsson, “Stored Energies Derived from Material Perturbation”, *17th European Conference on Antennas and Propagation (EuCAP 2023)*, Florence, Italy, 26 to 31 March 2023.
- VIII. Ben A. P. Nel, Anja K. Skrivervik and Mats Gustafsson, “Q factor Bounds for Microstrip Patch Antennas”, *Swedish Microwave Days, KTH Royal Institute of Technology*, Stockholm, Sweden, 23 to 24 May 2023.

- IX. Elias Björk, Linus von Ekensteen Löfgren, Oskar Watsfeldt, Ben A. P. Nel and Johan Lundgren, 2023 IEEE AP-S Student Design Contest Winners (First Place) Rice Box Group for Lund University, *IEEE International Symposium on Antennas and Propagation and USNC-URSI Radio Science Meeting*, Portland, Oregon, USA, 23 to 28 July 2023.

## **Workshop Contributions**

- Ben A. P. Nel, “Optimal Design for Microstrip Antennas”, *Modern Optimization and Machine Learning in Acoustics, EM, Radar, and Sonar*, Online, 19 May 2021.
- Ben A. P. Nel, “Q-factor and Radiation Efficiency Bounds for Microstrip Patch Antennas”, *Workshop on Stored Energy, Losses and Other Antenna Limitations*, Les Marécottes, Switzerland, 23 June 2023.



# Acronyms and Symbols

## ACRONYMS AND ABBREVIATIONS

<b>5G</b>	Fifth generation mobile networks
<b>FDTD</b>	Finite-difference time-domain
<b>FEM</b>	Finite element method
<b>HED</b>	Horizontal electric (Hertzian) dipole
<b>IR</b>	Infrared
<b>MPIE</b>	Mixed-potential integral equation
<b>MoM</b>	Method of moments
<b>PEC</b>	Perfect electric conductor
<b>PIFA</b>	Planar inverted-F antenna
<b>PMC</b>	Perfect magnetic conductor
<b>QCQP</b>	Quadratically constrained quadratic programs
<b>RF</b>	Radio frequency

## LATIN SYMBOLS

Boldface italic is used for vectors and boldface roman is used for matrices.

$A$	—	Absorptance
$B_{I_0}$	—	Fractional bandwidth
$c_0$	$\text{m s}^{-1}$	Speed of light in free space
$D$	—	Directivity
$\mathbf{E}$	$\text{V m}^{-1}$	Electric field
$f$	Hz	Frequency
$\mathbf{F}_s$	—	Far-field integration matrix
$\mathbf{F}$	—	Far-field matrix
$G$	—	Gain
$h$	m	Substrate thickness
$\mathbf{H}$	—	Hermitian transpose
$\mathbf{H}$	$\text{A m}^{-1}$	Magnetic field
$\mathbf{I}$	A	Current column vector
$\mathbf{J}$	$\text{A m}^{-2}$	Current density
$P_r$	W	Radiated power
$P_d$	W	Dissipated power
$P_\Omega$	W	Ohmic losses (power)
$P_\varepsilon$	W	Dielectric losses (power)
$R$	—	Reflectance
$\mathbf{R}$	$\Omega$	MoM resistance matrix
$\mathbf{R}_r$	$\Omega$	MoM radiation resistance matrix
$R_{\text{in}}$	$\Omega$	Input resistance
$\mathbf{R}_\varepsilon$	$\Omega$	MoM matrix for dielectric resistance
$R_{\text{in}}$	$\Omega$	Input resistance
$T$	—	Transmittance
$U$	$\text{W sr}^{-1}$	Radiation intensity
$\mathbf{V}$	V	Voltage column vector
$\mathbf{X}$	$\Omega$	MoM reactance matrix
$\mathbf{X}_e$	$\Omega$	MoM stored electric energy matrix
$\mathbf{X}_m$	$\Omega$	MoM stored magnetic energy matrix
$X_{\text{in}}$	$\Omega$	Imaginary parts of the input impedance
$\mathbf{Z}$	$\Omega$	MoM impedance matrix
$Z_0$	$\Omega$	Free-space impedance
$Z_{\text{in}}$	$\Omega$	Input impedance

## GREEK SYMBOLS


$\Gamma$	—	Reflection coefficient
$\Gamma_0$	—	Reflection coefficient threshold
$\varepsilon_0$	F m <sup>-1</sup>	Permittivity of free space
$\varepsilon_r$	—	Relative permittivity
$\eta$	—	Radiation efficiency
$\lambda$	m	Free space wavelength
$\lambda_\varepsilon$	m	Dielectric wavelength
$\mu_0$	H m <sup>-1</sup>	Permeability of free space
$\rho_{\min}$	m	Minimum radial distance between source and observer points
$\rho_{\max}$	m	Maximum radial distance between source and observer points
$\psi_m$	—	Basis functions
$\omega$	rad s <sup>-1</sup>	Angular frequency
$\Omega$	—	Design region



# INTRODUCTION



# Background and Motivation

NTENNAS have been widely used for many decades, playing a vital role across various applications, including cellular and satellite communication, broadcasting, and radar systems [43, 45, 96]. Achieving high performance and efficiency in antenna design is essential for ensuring reliable and effective communication [34, 89]. Although antennas are often just a component in larger systems, the demand for higher data rates and reduced power consumption makes it increasingly important to develop optimal or near-optimal antenna designs [9, 23, 27, 28, 36, 111].

To quantify the performance of antennas, there are several important performance metrics to consider [48]. For example, bandwidth or Q-factor [9, 10, 24, 26, 44, 67, 105, 114] (inversely proportional to bandwidth), radiation efficiency [49], and gain [112]. In simple terms, a wider bandwidth allows for higher data rates, increased radiation efficiency means more input power is radiated leading to lower antenna losses, and gain is a measure of how transmitted power is concentrated in a specified direction [36] or power is received from a specific direction. All of these performance metrics need to be traded off against form factor [98] as design space is often limited.

Antenna performance metrics can be reliably simulated using commercially available software such as FEKO [2] or CST [11]. They can employ several numerical techniques to solve electromagnetic problems such as the method of moments (MoM) [37, 51], the finite element method (FEM) [52], the finite-difference time-domain (FDTD) [63] method and high-frequency techniques [46]. These simulation tools can be used in the design process of antennas. They can be used both to gain physical insight into a given design as well as to assess the performance of a potential new design.

There are a few approaches to optimizing performance metrics of antennas, for example, using topology optimization or heuristic methods [8, 41, 91]. However, these approaches may find local optima far from the global optimum [6]. These approaches may also struggle to assess the quality of the obtained design without benchmarking against a performance limit.

To assess whether a desired antenna performance is feasible given a set of design constraints, bounds can be used. Antenna bounds can be traced back to the Chu limit [9], introduced in the 1940s, which defines a fundamental physical constraint on the Q-factor of electrically small antennas. This remains crucial for understanding the limits of antenna performance. However, it assumes a spherical design region, and since most antennas are not spherical, these bounds may be far from achievable [80] in practice. Therefore, more recently bounds have been computed using current optimization [27, 30, 49, 53, 104] along with other approaches [28, 113]. By restricting the problem to a design region, these bounds can be tighter to practical design performance. Using current optimization to establish antenna performance bounds requires linking the currents within the design region to the specific performance metric under consideration. A MoM formulation [37, 51] is ideally suited as it relates antenna currents and performance through the MoM impedance matrix.

One way of assessing the tightness of a determined bound is by comparing it to antenna designs, given the same design constraints. If a design's performance is close to these bounds, it indicates that the bounds are near achievable (tight). Conversely, if its performance differs significantly, it may reveal opportunities for improvement. In such cases, refining the bounds and/or exploring new optimized designs can help bring the bounds and design performance closer.

Also important to understanding the performance of antennas are stored electric and magnetic energies that have been investigated for several decades [16, 95]. The main reason why stored energies are relevant to antennas is that they are required to compute the Q-factor that can be determined at a single frequency from antenna currents. Q-factor is inversely proportional to fractional bandwidth and can be used to optimize the latter [29].

In this thesis, bounds are derived for microstrip patch antennas. These antennas have been in use for several decades [17, 48, 88] and remain popular due to their low profile, low cost, and ease of integration with other electronic components [59, 97, 108]. However, microstrip patch antennas have limitations, such as relatively narrow bandwidth and low radiation efficiency [13, 60], making investigating and understanding these parameters essential. A simple first-order approximation of these antennas' performance can be achieved using the cavity model [32, 47, 48, 94]. This simple model provides an intuitive way of understanding how the patch operates. The cavity model is useful for understanding half-wavelength resonant patches. Thus, while it is a reasonable method to gain insight and get a prediction, for performance analysis, a more complex approach that takes into account all the electromagnetic properties is required. This can be done using a full wave electromagnetic technique such as the MoM [37, 51].

One way of implementing MoM for microstrip patch antennas is by using Green's functions for layered media that can be evaluated using Sommerfeld integrals [75, 100]. The Sommerfeld integral formulation of Green's functions for these antennas [75] assumes that the dielectric substrate and the ground plane are infinite [75]. This formulation results in the currents on the patch being the only unknowns, all other currents being implicitly accounted for [100]. This

has a considerable computational advantage over not implicitly accounting for the currents on the ground plane and dielectric substrate [72]. Further, solving the Sommerfeld integrals over its infinite interval is not entirely straightforward. Fortunately, much work has been done in computing these integrals in fast and efficient ways [70, 75].

In this thesis, a single-layer dielectric substrate and infinite ground plane are assumed [80]. This is to achieve the goal of this thesis, which is to determine microstrip patch antenna performance limits. It should be noted that there are a few design variations that may improve the performance of microstrip patch antennas that are not examined in this thesis. Some examples are reducing the size of the ground plane and using stacked patches [47, 98, 115]. However, the presented bounds do include, for example, slot-loaded patches and some parasitic elements. These bounds serve as the first canonical case for antennas that are in wide use and can be extended in the future to consider more design variations.

Through using the layered Green's function that is implemented using Sommerfeld integrals [75, 100], this thesis extends existing far-field expressions [75] to the case of a lossy substrate where they can also be shown to be valid. Further, the conventional approach is to compute stored energies by taking frequency derivatives of the MoM reactance matrix. This is extended to Sommerfeld integrals in this thesis. Then, since there is still no agreement on how to compute stored energies of radiating systems, the question of how the material properties surrounding an antenna influence the understanding of stored energy is also addressed here [81, 82]. This is done by showing that for a radiating system, the stored electric energy can be related to a perturbation of permittivity, and stored magnetic energy can be related to a perturbation of permeability.

This thesis determines bounds on microstrip patch antenna performance using current optimization. This is done by using the computed MoM matrices using Sommerfeld integrals. These are then used to solve quadratically constrained quadratic programs (QCQPs) [6]. Using this, the lower bounds on Q-factor [80] are determined and shown to be tight over a range of electrical sizes. As they are tight, they are a good predictor of the performance of microstrip patch antennas' performance. Further bounds on maximum radiation efficiency [82] are also determined and are shown to be tight to both the simulations and the measurements of some practical antenna designs. Bounds on, maximum gain for microstrip patch antennas are also determined and shown to be tight.

The MoM matrices required to determine the bounds for microstrip patch antennas may not be easily accessible using commercial software. Therefore, an easy-to-use approximation of the lower Q-factor is derived and provided [80]. Further, after linking lower Q-factor bounds to maximum radiation efficiency this easy-to-use approach is extended to maximum radiation efficiency [82]. The approach relies on the simulation or measurement of a half-wavelength patch and uses a scaling rule to approximate the bounds for miniaturized designs.

Finally, the ability to measure the fields produced by radiating structures is often time-consuming and expensive. This thesis assesses the potential of using a metasurface to perform field measurements of a device under test [83]. This

method relies on using an infrared (IR) camera to image the metasurface in the presence of a radio frequency (RF) field [64]. IR cameras have been employed for several decades to perform indirect assessments of RF fields [7,14,22,57,78]. This thesis focuses on the metasurface elements' design performance. The performance of different metasurface elements is compared as potential candidates to be used in this measurement setup. The investigated elements are chosen for properties such as their polarization selectivity. The power dissipated on the metasurface elements is compared to the expected RF field in the absence of the metasurface.

The remainder of this thesis is structured as follows. First, the microstrip patch antenna geometry is described in Chapter 2. Then Chapter 3 provides a basic understanding of half-wavelength resonant microstrip patch antennas through the cavity model. Chapter 4 describes the MoM and how it can be used to simulate microstrip patch antennas. Further Chapter 5 describes how stored energies are related to material properties and how this can be used to relate Q-factor to radiation efficiency. The formulation of the optimization problem used is presented in Chapter 6. Results obtained with this formulation are presented in Chapter 7. Then the description and simulations of the metasurface used for electromagnetic measurements are described in Chapter 8. Finally, a summary of the thesis and potential future work is presented in Chapter 9.

## Microstrip Patch Antennas

**I**N this chapter, the microstrip patch antenna geometry considered is presented along with a basic discussion on functionality. Some classical patch designs are also shown.

An example of a microstrip patch antenna can be seen in Figure 1. The patch design region  $\Omega$  is on top of the infinite dielectric substrate of relative permittivity  $\epsilon_r$  and thickness  $h$ . The dielectric substrate is on top of an infinite PEC ground plane. The assumption of infinite dielectric and ground plane greatly reduces the computational cost as the currents on the patch region are the only unknowns, implicitly accounting for all other currents and fully characterizing the performance. This can be thought of as using image currents to characterize the ground plane where the patch currents are the only unknowns [51, 104]. For arbitrary substrate permittivity, this is done using layered Green's functions [75] as described in Chapter 4. It has also been shown that an infinite dielectric substrate and ground plane is a reasonable assumption to model microstrip patch antennas of moderate size [17, 82].

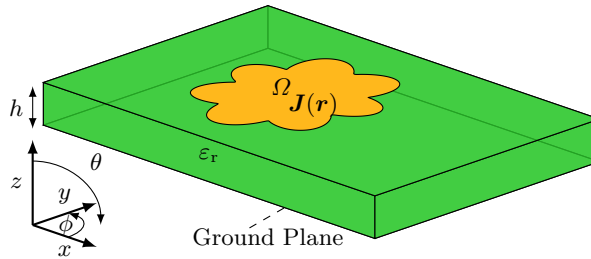


**Figure 1:** The design region for the microstrip patch antenna is defined as  $\Omega$ , which includes all possible metal patch geometries that fit within it. The surface current density over this region is denoted by  $\mathbf{J}(\mathbf{r})$ . An infinite dielectric substrate with a relative permittivity  $\epsilon_r$  and a thickness  $h$  is on top of an infinite PEC ground plane.

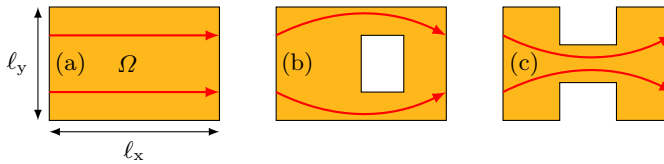


**Figure 2:** Three example patch geometries fitting within the rectangular design region  $\Omega$  with dimensions  $\ell_x \times \ell_y$ . They are (a) rectangular patch, (b) slot-loaded patch, and (c) H-shaped patch. Example current patterns are indicated by red arrows.

Example designs of microstrip patch antennas are shown in Figure 2. The patch region is a conductor placed on top of a dielectric layer with relative permittivity  $\varepsilon_r$ . Below the dielectric layer is the ground plane. The patch can be fed, for example, with a probe feed [69] or microstrip line [60]. The patch design region chosen for this thesis is rectangular with dimensions  $\ell_x$  and  $\ell_y$  (see Figure 2). Although design regions with other shapes could have been chosen, many classical designs are rectangular or well confined within a rectangular region with some geometry removed [47, 48]. Removing part of the conducting patch geometry within the rectangular region can be used for miniaturized or dual resonant applications [40, 48].

Some examples of classical patch antenna designs fitting within the design region ( $\Omega$ ) are the rectangular patch (a), slot-loaded patch (b), and H-shaped patch (c), as shown in Figure 2. The H-shaped and slot-loaded patch antennas are miniaturized designs with lower resonance frequencies for the same dimensions. The rectangular patch is resonant at around half a wavelength in the dielectric substrate [48]. The other patches can be resonant at a lower frequency [48] for the same design region as they lengthen the current path by bending it, as shown in Figure 2. This, however, comes at the cost of performance. The squeezed currents result in higher Ohmic losses compared to radiated power and, therefore, a design that spreads out the currents is generally desired. It should be noted that this thesis only considers Ohmic losses on the patch region and not on the ground plane.

The in-house code developed in this thesis uses layered Green's functions determined using Sommerfeld integrals [75]. By using these layered Green's functions, the currents on the patch design region ( $\Omega$ ) are the only unknowns and fully characterize the performance of the microstrip patch antenna. Therefore, all other currents are implicitly accounted for. In some other implementations, such as the volumetric MoM, the dielectric substrate and ground plane also need to be discretized.

## Cavity Model

**T**HE cavity model [32, 48, 54, 62, 85, 94] provides a basic description of the behavior of a half-wavelength resonant microstrip patch antenna by representing it as a rectangular cavity, as shown in Figure 3. The figure shows an approximation of the field distribution for a half-wavelength rectangular patch (see Figure 3 with patch geometry shown in Figure 2(a)).

In the cavity model, the patch and its ground plane are approximated as perfect electric conductors (PECs), and between them is the dielectric substrate with relative permittivity  $\epsilon_r$ . The cavity boundaries along the other four sides (see Figure 3) are approximated as perfect magnetic conductors (PMCs), meaning the tangential component of the magnetic field at these edges is assumed to be zero.

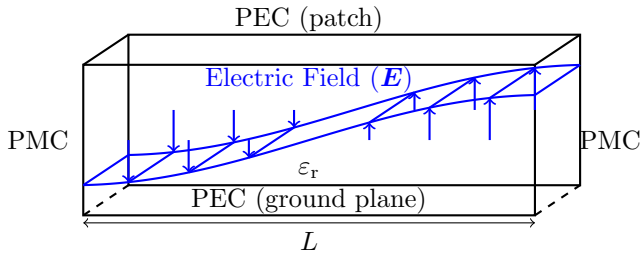


**Figure 3:** The cavity model with PEC at the top and bottom and PMC on the other four walls. The cavity is filled with material that has a relative permittivity  $\epsilon_r$ , and the electric field varies sinusoidally along the length ( $L$ ) of the cavity.

The choice of cavity boundary conditions can be understood by the typically highly conductive (especially at microwave frequencies) behavior of the ground plane and patch region being modeled as PECs. As the field typically attenuates rather rapidly outward from the other four boundaries it is reasonable to approximate these boundaries as PMCs, corresponding to open-circuit boundaries for the magnetic field. Together, these approximations allow the patch region to be

treated as a resonant cavity with well-defined modes, facilitating the derivation of closed-form approximations for the patch antenna's resonant frequencies, field distributions, and input impedance [48].

The electric and magnetic fields in the cavity are described by their resonant modes, with the half-wavelength resonance being the fundamental cavity mode if the cavity length is greater than the width. For the half-wavelength resonance along the length, the electric field varies sinusoidally along the length of the patch while remaining uniform across its width, supported by a corresponding magnetic field distribution. The resonant dielectric wavelength  $\lambda_\epsilon$  and resonant frequency  $f$  for the half-wavelength resonance along the length are

$$\lambda_\epsilon = \frac{\lambda}{\sqrt{\epsilon_r}} = 2L = \frac{c_0}{f\sqrt{\epsilon_r}} \quad \text{and} \quad f = \frac{c_0}{2L\sqrt{\epsilon_r}}, \quad (3.1)$$

respectively. The free space wavelength is given by  $\lambda$ . The resonant length is, as the resonance name suggests, half a wavelength in the dielectric cavity [48], and the speed of light in free space is given by  $c_0$ . It should be noted that here, as is generally a good approximation, the substrate is assumed to be nonmagnetic.

The input impedance of the antenna varies with the feed point's position. At the center of a half-wavelength patch, the input impedance would be observed as a short circuit. At the edge of the patch along the dimension of charge separation, the input impedance is an open circuit. From the cavity model, a formula can be used to adjust the probe feed location to achieve matching [47].

The cavity model, along with the transmission line model [77], is an excellent intuitive guide but not a tool for accurate numerical analysis due to assumptions such as ideal boundaries that lead to inaccuracies, particularly for thicker substrates or high-frequency applications. The model also neglects the surface wave. In Chapter 4, a versatile numerical method for evaluating the performance of microstrip patch antennas is presented.

## Method of Moments

**T**HIS chapter presents the MoM formulation that is used to determine bounds on microstrip patch antennas performance in this thesis. The free-space MoM can be used to discretize the current density on the conducting structure using basis function  $\psi_m$  [19, 37, 51, 107]. The divergence-conforming basis functions used in this thesis are rooftop basis functions [12, 87, 106], the rectangular cells are shown in Figure 4 for basis functions in the  $x$ -direction shown in red, and basis functions in the  $y$ -direction shown in green. It should be noted that while rectangular cells were chosen in this thesis, triangular cells could also be used [87].

The basis functions can be used to represent the current density as

$$\mathbf{J}(\mathbf{r}) = \sum_{m=1}^M I_m \psi_m(\mathbf{r}), \quad (4.1)$$

where the expansion coefficients  $I_m$  for the  $M$  mesh elements are collected in the mesh currents  $\mathbf{I} \in \mathbb{C}^{M \times 1}$ . Further, the dyadic free space Green's function is used and given by [56]

$$\mathbf{G}(\mathbf{r}', \mathbf{r}) = \left( \mathbf{1} + \frac{1}{\omega^2 \varepsilon_0 \mu_0} \nabla \nabla \right) \frac{e^{-j\omega \sqrt{\varepsilon_0 \mu_0} |\mathbf{r}' - \mathbf{r}|}}{4\pi |\mathbf{r}' - \mathbf{r}|}, \quad (4.2)$$

where  $\mathbf{1}$  is the identity tensor. The source and observer points are given by  $\mathbf{r}'$  and  $\mathbf{r}$ , respectively. The angular frequency is given by  $\omega = 2\pi f$ . The free-space permittivity and permeability are given by  $\varepsilon_0$  and  $\mu_0$ , respectively. Using the dyadic Green's function (4.2), the free space part of the impedance matrix used at the conductor interface is given by integrating over the testing and source basis functions ( $\psi_m$  and  $\psi_n$ ) using the Galerkin method (same source and testing basis functions) as

$$Z_{0,mn} = j\omega\mu_0 \int_{\Omega} \int_{\Omega} \psi_m(\mathbf{r}') \cdot \mathbf{G}(\mathbf{r}', \mathbf{r}) \cdot \psi_n(\mathbf{r}) dS' dS. \quad (4.3)$$

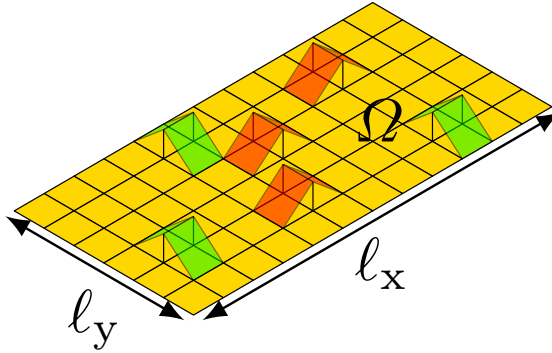


**Figure 4:** Example rectangular region with dimensions  $\ell_x \times \ell_y$  with currents discretized using rooftop basis functions in the  $x$ -direction shown in red and in  $y$ -direction shown in green.

The part of the impedance matrix due to Ohmic losses is given by

$$R_{\Omega, mn} = R_s \int_{\Omega} \psi_m(\mathbf{r}) \cdot \psi_n(\mathbf{r}) dS, \quad (4.4)$$

where  $R_s$  is the surface resistivity. These integrals can be performed numerically by using a Gaussian quadrature integration scheme on the non-singular part, and an analytic approach can be used to integrate over the singular part. The MoM matrix is then given by the sum of Ohmic (4.3) and free space impedance matrices (4.4) as [30]

$$Z_{mn} = Z_{0, mn} + R_{\Omega, mn}. \quad (4.5)$$

Further, as the same source and testing basis functions are used [37], the MoM impedance matrix (4.5) is symmetric.

The MoM is often applied with a known input voltage and geometry. The impedance matrix of the given geometry relates the currents to voltages as

$$\mathbf{V} = \mathbf{Z}\mathbf{I}, \quad (4.6)$$

where the voltage vector is given by  $\mathbf{V} \in \mathbb{C}^{M \times 1}$ . The impedance matrix is given by  $\mathbf{Z} \in \mathbb{C}^{M \times M}$ . Then, (4.6) can be rewritten to solve for the currents by inverting the impedance matrix as

$$\mathbf{I} = \mathbf{Z}^{-1}\mathbf{V}. \quad (4.7)$$

Much of computational electromagnetics is concerned with the performance of a given design and excitation (input voltage) [37, 52, 79], this can be done using (4.7). However, this thesis focuses on determining the optimal currents for an arbitrary geometry within a conducting region using in-house code and commercial solvers to compare to the performance of a known design that is obtained in part solving (4.7).

## 4.1 LAYERED GREEN'S FUNCTIONS AND SOMMERFELD INTEGRALS

To model microstrip patch antennas using the MoM, the free space Green's function (4.2) needs to be modified. This is because the infinite ground plane and dielectric substrate require layered Green's functions. The integrals suited to obtaining the layered Green's functions used to determine MoM matrices for microstrip patch antennas are Sommerfeld integrals, they are mathematically equivalent to inverse Hankel transforms [76]. They were originally proposed for long-distance wireless radio and telegraphy. However, today, they have found many applications in electromagnetic modeling [76]. In the case of microstrip patch antennas, these integrals can be used in such a way that only the currents on the patch design region are the unknowns. It should, however, be noted that other approaches could also be used to determine similar matrices, such as discrete complex images method [1, 15] and rational function fitting method [55, 84]. These Green's functions can be used in a Mixed-Potential Integral Equation (MPIE) formulation [74, 75] that is employed in this thesis.

Using the Sommerfeld integrals,  $(S_0)$ , Green's functions can be written for a single layer microstrip patch antenna as [75]

$$G_A(\rho_{12}) = \frac{1}{4\pi} S_0 \left( \frac{1}{D_{TE}} \right) \quad \text{and} \quad G_V(\rho_{12}) = \frac{1}{4\pi} S_0 \left( \frac{N}{D_{TE} D_{TM}} \right), \quad (4.8)$$

where  $G_A$  is the dyadic Green's function for the vector potential,  $G_V$  is the scalar Green's function for the scalar potential, and the radial distance is given by  $\rho_{12} = |\mathbf{r}' - \mathbf{r}|$ . Further,  $D_{TE}$ ,  $D_{TM}$ , and  $N$  in (4.8) are defined as [75]

$$\begin{aligned} D_{TE} &= u_1 + u_2 \coth(u_2 h), \\ D_{TM} &= \varepsilon_r u_1 + u_2 \tanh(u_2 h), \\ N &= u_1 + u_2 \tanh(u_2 h), \end{aligned} \quad (4.9)$$

with

$$u_1 = \sqrt{k_\rho^2 - \omega^2 c_0^{-2}} \quad \text{and} \quad u_2 = \sqrt{k_\rho^2 - \omega^2 \varepsilon_r c_0^{-2}}, \quad (4.10)$$

where  $k_\rho$  is the radial spectral coordinate. The Sommerfeld integral is an infinite integral defined in the spectral domain and given by [75]

$$S_0(g) = 2 \int_0^\infty J_0(k_\rho \rho_{12}) k_\rho g(k_\rho, \omega) dk_\rho, \quad (4.11)$$

where  $g$  is the function the Sommerfeld integral is applied to and  $J_0$  is the Bessel function of order 0. There are many challenges when computing Sommerfeld integrals [70]. One of these challenges comes from the poles in the spectral domain when  $D_{TM} = 0$  or  $D_{TE} = 0$ . Special care must be taken to correctly navigate the presence of the poles and to ensure the integral is performed on the correct Riemann-sheet [71]. Further, the convergence of the Sommerfeld integrand may be very slow and, in some cases, even divergent [70]. To handle

this, the generalized weighted averages procedure, also referred to as the Mosig-Michalski algorithm, is used as presented in [68, 70].

Even when the Sommerfeld integral is computed efficiently, it still takes considerable time to compute each spatial distance between source and observer points, and since each basis function has a few sample points, this time can become intractable. To avoid this challenge, an interpolation scheme is used [75]. In this scheme, a set of radial distances is determined ( $\rho_{12}$ ), and the required integrals are interpolated based on this. This is done as shown in [75] in a quadratic manner where the sample points are chosen by

$$\rho_l = \frac{\rho_{\max} - \rho_{\min}}{n^2 - 1}(l^2 - 1) + \rho_{\min}, \quad (4.12)$$

where the minimum and the maximum radial distance between source and observer points are given by  $\rho_{\min}$  and  $\rho_{\max}$ , respectively. The number of sample points is given by  $n$  and  $l \in \{1, \dots, n\}$ . In this thesis, generally, between  $n = 300$  and  $n = 500$  sample points are taken to ensure convergence and spline interpolation [66] was used to approximate the scalar and dyadic Green's functions between sample points. It should be noted that the minimum radial distance used is where the Green's function is not considered spatially singular, this singularity is discussed in more detail in Section 4.2.

## 4.2 SINGULARITY WHEN DETERMINING THE SELF INTEGRAL

Similar to the singularity in the spectral domain described in Section 4.1 that is due to the surface wave, a spatial singularity is also encountered when determining the MoM impedance matrix. This is due to the denominator going to zero as  $\rho_{12} \rightarrow 0$ . It is important to note here already that even though the integrand tends to infinity as  $\rho_{12} \rightarrow 0$ , the integral is still finite. To separate the scalar Green's function and dyadic Green's function into a singular and non-singular part, the asymptotic expressions from [75] are used. For the dyadic Green's function, this expression is

$$G_A \approx \frac{\mu_0}{4\pi} \sum_{i=0,1} \frac{e^{-jk\rho_i}}{\rho_i}, \quad (4.13)$$

where  $k = \omega\sqrt{\varepsilon_0\mu_0}$  is the free space wavenumber and

$$\rho_i = \sqrt{\rho_{12}^2 + 4i^2h^2}. \quad (4.14)$$

Therefore, the dyadic Green's function has a part containing a singularity ( $i = 0$ ) when  $\rho_{12} \rightarrow 0$  and one non-singular part. The dyadic Green's function (4.13) asymptotic expression is independent of the real part of relative permittivity. It is easy to determine the non-singular part ( $i = 1$ ).

The scalar Green's function singularity is significantly impacted by the dielectric substrate's relative permittivity. The non-singular part is an infinite sum

that, when the relative permittivity is one, is the same as the dyadic Green's function (4.13). This is given by

$$\mathbf{G}_V \approx \frac{1 - \zeta}{4\pi j\omega\epsilon_0} \left[ \frac{e^{-jk\rho_{12}}}{\rho_{12}} - (1 + \zeta) \sum_{i=1}^{\infty} (-\zeta)^{i-1} \frac{e^{-jk\rho_i}}{\rho_i} \right], \quad (4.15)$$

where  $\zeta = (\epsilon_r - 1)/(\epsilon_r + 1)$  and  $\rho_i$  is given in (4.14). The infinite sum converges [75] well for reasonable  $i$ .

The singular part of both the scalar and dyadic Green's function can have the exponent written in terms of sine and cosine terms. Once this is done, the sine term that is associated with losses is non-singular as  $\lim_{\rho_{12} \rightarrow 0} \sin(\rho_{12})/\rho_{12} = 1$  and therefore can easily be determined. However, taking the Taylor series expansion of the cosine term results in one singular term and infinite non-singular terms that rapidly converge.

Using the above-mentioned approach of separating the singular and non-singular special parts of the scalar and dyadic Green's functions, the non-singular part is simply integrated with the rest of the non-singular interpolated (4.12) Sommerfeld integrals to determine the impedance matrix that is linked to the dyadic and scalar Green's functions. With this, the dyadic Green's function is known or can be determined from the interpolation scheme. Spatial integration can be performed to determine matrix entries between source and testing basis functions

$$L_{mn} = \int_{\Omega} \int_{\Omega} \boldsymbol{\psi}_m(\mathbf{r}') \cdot \mathbf{G}_A(\rho_{12}) \cdot \boldsymbol{\psi}_n(\mathbf{r}) dS' dS, \quad (4.16)$$

and similarly for the scalar Green's function, spatial integration can be performed

$$C_{imn} = \int_{\Omega} \int_{\Omega} \nabla_1 \cdot \boldsymbol{\psi}_m(\mathbf{r}') \nabla_2 \cdot \boldsymbol{\psi}_n(\mathbf{r}) G_V(\rho_{12}) dS' dS, \quad (4.17)$$

where entries of  $L_{mn}$  can be written in matrix form as  $\mathbf{L}$  and entries of  $C_{imn}$  written in matrix form as  $\mathbf{C}_i$ . These matrices are broadly linked to the inductance and inverse of the capacitance, respectively.

The contribution of the spatially singular part not considered in the interpolation (4.12), needs to be included [33] in the MoM matrix (4.5), setting a threshold where the integrand is considered singular, and where not, the  $1/\rho_{12}$  part is integrated spatially analytically and added back to (4.16) and (4.17). It should be noted that when dielectric losses were added, the asymptotic expressions for the dyadic (4.13) and scalar (4.15) Green's functions were numerically adjusted as the non-singular part associated with dissipated power has changed in a way not captured by using complex permittivity values in the asymptotic expressions.

The computed matrices can be used to calculate the MoM impedance matrix (4.5) as [99]

$$\mathbf{Z} = j\omega\mu_0\mathbf{L} + \frac{\mathbf{C}_i}{j\omega\epsilon_0} + \mathbf{R}_{\Omega}, \quad (4.18)$$

where  $\mathbf{R}_\Omega$  (4.4) is due to Ohmic losses on the patch design region ( $\Omega$ ).

The MoM matrix along with the patch currents, can be used to analyze the performance of the microstrip patch antenna. In this thesis, the MoM matrix must be broken into separate components associated with a particular physical phenomenon. This is done in Sections 4.3.

### 4.3 INTERPRETING THE IMPEDANCE MATRIX OF MICROSTRIP PATCH ANTENNAS

It is possible to split the MoM impedance matrix (4.18) into a resistive ( $\mathbf{R}$ ) and a reactive ( $\mathbf{X}$ ) part as

$$\mathbf{Z} = \mathbf{R} + j\mathbf{X}. \quad (4.19)$$

These parts of the impedance matrix can be expressed in terms of the impedance matrix as

$$\mathbf{R} = \frac{\mathbf{Z} + \mathbf{Z}^H}{2} \quad \text{and} \quad \mathbf{X} = \frac{\mathbf{Z} - \mathbf{Z}^H}{2j}, \quad (4.20)$$

where the Hermitian transpose is denoted by superscript  $^H$ .

The real part of the impedance matrix  $\mathbf{R}$  is related to the dissipated power ( $P_d$ ) for a known current vector as

$$P_d = \frac{1}{2} \mathbf{I}^H \mathbf{R} \mathbf{I}. \quad (4.21)$$

When considering the resistance matrix (4.20) for microstrip patch antennas, it can be separated into three separate parts as [82]

$$\mathbf{R} = \mathbf{R}_r + \mathbf{R}_\Omega + \mathbf{R}_\epsilon, \quad (4.22)$$

where  $\mathbf{R}_r$  is the radiation resistance matrix that relates currents to radiated power. The derivation of this matrix is presented in Section 4.5. Further, currents on the patch design region can lead to Ohmic losses, the matrix used to determine this is  $\mathbf{R}_\Omega$ . This matrix can be determined from the Gram matrix [23,42] as shown in (4.4), it is a sparse matrix as Ohmic losses are only affected by overlapping basis functions. The dielectric resistance is given by  $\mathbf{R}_\epsilon$ . This matrix can be influenced by both the patch currents' relationship to dielectric losses and surface wave losses. While strictly speaking, the surface wave is only defined for a lossless dielectric substrate. However, in this thesis, it is still found that in some cases, it may be necessary to separate the dielectric losses coming from a propagating wave and those from the electric near field.

The different components of the resistance matrix (4.22) can be used to break up the dissipated power as

$$P_d = P_r + P_\Omega + P_\epsilon = \frac{1}{2} \mathbf{I}^H \mathbf{R} \mathbf{I}, \quad (4.23)$$

where the radiated power is given by  $P_r$  and power dissipated due to Ohmic losses given by  $P_\Omega$ . The power lost in the dielectric is given by  $P_\epsilon$  and is due to the surface wave and dielectric losses.

The imaginary part of the impedance matrix (4.20) for a known current is related to the difference between total stored magnetic and total stored electric energies as

$$W_m - W_e = \frac{1}{4\omega} \mathbf{I}^H \mathbf{X} \mathbf{I}, \quad (4.24)$$

where the stored magnetic and stored electric energies are given by  $W_m$  and  $W_e$ , respectively. The imaginary part of the impedance matrix can be split into two parts as [37, 105]

$$\mathbf{X} = \mathbf{X}_m - \mathbf{X}_e, \quad (4.25)$$

where  $\mathbf{X}_m$  relates the currents to the stored magnetic energy and  $\mathbf{X}_e$  relates the currents to stored electric energy. The stored electric and magnetic energies are non-trivial to separate from the reactance matrix, and in Chapter 5, how to compute them in alternative ways is discussed. They are required, as the Q-factor used to optimize bandwidth requires that stored electric and stored magnetic energies are known. When the stored electric and magnetic energies related to (4.25) are equal, then the antenna is resonant ( $\mathbf{I}^H \mathbf{X} \mathbf{I} = 0$ ).

## 4.4 RADIATION EFFICIENCY AND GAIN

Radiation efficiency and gain are key performance metrics for antennas, similar to Q-factor. Radiation efficiency is a measure of how much power an antenna radiates compared to dissipated power (4.21). Therefore, a higher radiation efficiency means the antenna is better at converting input power into radiated power.

Radiation efficiency is given by [30]

$$\eta = \frac{P_r}{P_d} = \frac{\mathbf{I}^H \mathbf{R}_r \mathbf{I}}{\mathbf{I}^H \mathbf{R} \mathbf{I}}. \quad (4.26)$$

How to determine this radiation resistance matrix is discussed in Section 4.5.

Even with a high radiation efficiency, this does not mean that the power of the antenna is transmitted in the desired direction, this is quantified by the gain that is given by [23]

$$G = 4\pi \frac{U}{P_d}, \quad (4.27)$$

where the radiation intensity is given by  $U$ . The gain is a combination of radiation efficiency and directivity given by the relationship

$$G = \eta D, \quad (4.28)$$

where directivity ( $D$ ) is the ratio of the maximum power density radiated in a specific direction to the average power density radiated by an isotropic antenna under the same radiated power [3, 35].

## 4.5 RADIATED POWER FOR MICROSTRIP PATCH ANTENNAS

The radiation resistance matrix can be used when computing radiation efficiency, as it is required to separate the radiated power from the dissipated power. Further, since one of the central topics of the thesis is current optimization to compute bounds on radiation efficiency, determining this matrix is of paramount importance as this allows for a direct way of relating patch currents to radiation efficiency.

To determine the radiation resistance matrix, the asymptotic expressions of the electric field from [71] are used. These expressions are in spherical coordinates (see the coordinate system in Figure 1). For this thesis, the electric far-field expressions that are derived for an  $\hat{\mathbf{x}}$ -directed horizontal electric (Hertzian) dipole (HED) with dipole moment  $J_h$  having units of Am, are converted to the far-field [75] components as

$$\begin{aligned} F_\theta &= \frac{Z_0}{2\pi} \frac{-J_h j k n_\theta \cos \phi \cos \theta}{n_\theta - j \varepsilon_r \cos \theta \cot(k h n_\theta)} \\ F_\phi &= \frac{Z_0}{2\pi} \frac{J_h j k \sin \phi \cos \theta}{\cos \theta - j n_\theta \cot(k h n_\theta)}, \end{aligned} \quad (4.29)$$

where  $n_\theta = \sqrt{\varepsilon_r - \sin^2 \theta}$  and the free-space impedance is given by  $Z_0$ . By performing a simple coordinate rotation, the far field from a  $\hat{\mathbf{y}}$ -directed HED can be determined. It should be noted that (4.29) was derived for a lossless dielectric substrate [75] and is here extended to the case of lossy dielectric substrates. These expressions can be shown to also be valid for lossy dielectric substrates and can alternatively be derived using reciprocity [51].

Through the integration of the far field (4.29), the radiation can be determined in any direction above the substrate given by [27, 56]

$$\mathbf{F}(\theta, \phi) \approx \mathbf{F}\mathbf{I}, \quad (4.30)$$

where the far-field matrix is given by  $\mathbf{F} \in \mathbb{C}^{2 \times M}$ . It relates currents to the far field in a spherical direction given by spherical coordinates, see Figure 1. The far-field can be used to determine the radiation intensity in a specific direction, required to compute gain (4.27). This is given by [23]

$$U(\theta, \phi) = \frac{|\mathbf{F}(\theta, \phi)|^2}{2Z_0}. \quad (4.31)$$

The radiated power is calculated by integrating over a hemispherical surface on the free-space side of the design region while neglecting surface wave effects near the grazing angle ( $\theta = \pi/2$ ). This calculation uses a set of quadrature points  $(\theta_n, \phi_n)$  and their corresponding quadrature weights. A matrix  $\mathbf{F}_s$  is constructed by evaluating the far-field matrices  $\mathbf{F}$  in (4.30) at the quadrature points, with each evaluation forming a row of  $\mathbf{F}_s$ . For simplicity, the square roots of the quadrature weights are incorporated into  $\mathbf{F}_s$ , enabling the radiated power  $P_r$  from the patch

currents  $\mathbf{I}$  to be determined using the radiation resistance matrix  $\mathbf{R}_r = \mathbf{F}_s^H \mathbf{F}_s$ , leading to

$$P_r = \frac{1}{2} \mathbf{I}^H \mathbf{F}_s^H \mathbf{F}_s \mathbf{I} = \frac{1}{2} \mathbf{I}^H \mathbf{R}_r \mathbf{I}. \quad (4.32)$$

In this thesis, a simple trapezoidal method [90] was used for integration of the far field and found to be sufficient.

## 4.6 RATIO OF SURFACE WAVE POWER TO RADIATED POWER

Surface waves are propagating waves in the dielectric substrate that can be launched by the patch [75]. For an infinite and lossless dielectric substrate, these waves propagate in the dielectric substrate. Should it be a finite substrate, the surface wave is radiated from the edge of the dielectric substrate, leading to radiation. However, this form of radiation is generally undesired [75] and, therefore, is not considered as such. It is required to separate the radiation resistance matrix (4.32) from the surface wave part to be able to determine the surface wave from the patch currents.

The surface wave power can be determined in two ways. One is from the Green's function by separating the radiated power and surface wave power. This can be done by noting that the pole in the spectral domain is connected to the surface wave. Then determining the contribution of the pole provides the surface wave. This was done in Paper I [80] by splitting the Sommerfeld integral into three parts as described in [75].

In this thesis, it is assumed that only the first transverse magnetic surface wave mode is propagating [71]. The thickness required for the first transverse electric surface wave mode to start propagating is  $h > \lambda / (4\sqrt{\epsilon_r} - 1)$  where a transverse electric pole is present.

In Paper II, the surface wave power was separated from the radiated power using the radiation resistance matrix, which can be determined as discussed in Section 4.4. Then, if there are no dielectric losses, the surface wave can be determined by subtracting the radiation resistance matrix and Ohmic loss matrix from the resistance matrix as (4.22)

$$\mathbf{R}_\epsilon = \mathbf{R} - \mathbf{R}_\Omega - \mathbf{R}_r. \quad (4.33)$$

This makes it possible to determine the surface wave-to-radiated power ratio for any current. However, as stated in [47], the surface wave-to-radiated power generally maintains that of an HED for small structures. Therefore, it is worth investigating whether this is also the case for some optimization problems. It is shown in Chapter 7 that in some optimization problems, this ratio can be approximated by [73]

$$\frac{P_{sw}}{P_r} \approx \Delta_{sw} = \frac{3\pi}{4} \frac{(\text{Re}\{\epsilon_r\} - 1)^3 kh}{\text{Re}\{\epsilon_r\}^2 (\text{Re}\{\epsilon_r\} - 1) + \frac{2}{5} \text{Re}\{\epsilon_r\}}. \quad (4.34)$$

This expression has been shown to generally be accurate for dielectric thicknesses  $h < 0.05\lambda$  [73]. By taking the real part of the relative permittivity in (4.34), the surface wave-to-radiated power ratio is assumed to remain constant with added dielectric losses.

## 4.7 Q-FACTOR

The Q-factor [9, 10, 24, 26, 44, 67, 105, 114] of antennas can be determined in several different ways [105, 114]. It is defined by the quotient of the maximum of stored electric or stored magnetic energies (4.24) and dissipated power as [9, 114]

$$Q = \frac{2\omega \max \{W_e, W_m\}}{P_d}. \quad (4.35)$$

The Q-factor of a microstrip patch antenna can be related to the patch currents. This is done by relating currents to dissipated power (4.21) and relating currents to stored electric and stored magnetic energies as is shown in Section 4.8.

The practical interest in Q-factor largely stems from the inverse relationship between Q-factor and fractional bandwidth given by [114]

$$Q_{\Gamma_0} = \frac{2}{B_{\Gamma_0}} \frac{\Gamma_0}{\sqrt{1 - \Gamma_0^2}}, \quad (4.36)$$

where  $B_{\Gamma_0}$  is the fractional bandwidth and  $\Gamma_0$  the reflection coefficient threshold. Therefore, by minimizing the Q-factor, the fractional bandwidth is maximized. However, since Q-factor can be determined at a single frequency, it is better suited for current optimization.

The relationship between Q-factor and fractional bandwidth (4.36) is shown in Figure 5 for an RLC circuit. Q-factors of 6 and 30 are chosen, and their reflection coefficients ( $\Gamma$ ) are shown for a range of normalized frequencies  $f/f_0$ , where  $f_0$  is the center frequency. For the Q-factor 6 curve, a reflection coefficient threshold of  $1/\sqrt{2}$  and  $1/3$  are shown to correspond to a fractional bandwidth of approximately 0.33 and 0.12, respectively.

Another method to compute Q-factor for a given design is from the angular frequency derivative of the input impedance as [92, 114]

$$Q_{Z'_{in}} \approx \frac{\sqrt{(\omega R'_{in})^2 + (\omega X'_{in} + |X_{in}|)^2}}{2R_{in}}, \quad (4.37)$$

where ' denotes angular frequency derivative and  $R_{in}$  and  $X_{in}$  are the real and imaginary parts of the input impedance, respectively.

At low frequencies, all three of these definitions of Q-factor produce approximately the same value for self-resonant antennas [95]. However, this is not always the case [95] as at higher frequencies, the stored energies are less clearly defined [31] as stored electric and stored magnetic energies become more correlated, making separation more difficult.

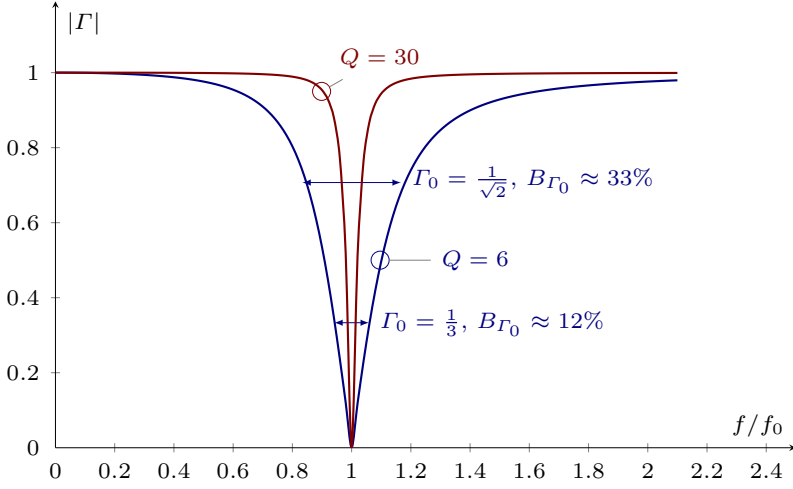


**Figure 5:** The resonance frequency magnitude for an RLC circuit with Q-factors 6 and 30 for center frequency  $f_0$ . The Q-factor 6 curve has a fractional bandwidth of approximately 0.33 and 0.12 for reflection coefficient threshold  $1/\sqrt{2}$  and  $1/3$ , respectively.

## 4.8 STORED ENERGIES

This thesis extends the understanding of stored energies [25,39,95,105] of radiating systems to microstrip patch antennas and introduces the relationship between these stored energies and material perturbations in the surrounding media. One way stored energies can be determined is from the electromagnetic field surrounding a radiating structure. This is done by approximately subtracting the radiated energy determined from the far field as was done by [16,25,114] and given by

$$W_F = \frac{1}{4} \int_{\mathbb{R}^3} \varepsilon_0 |\mathbf{E}(\mathbf{r})|^2 + \mu_0 |\mathbf{H}(\mathbf{r})|^2 - 2\varepsilon_0 \frac{|\mathbf{F}|^2}{|\mathbf{r}|^2} dV, \quad (4.38)$$

where the electric field and magnetic field are given by  $\mathbf{E}$  and  $\mathbf{H}$ , respectively. The terms containing the electric and magnetic fields account for the total stored energy. The propagating energy is approximately subtracted from the total energy using the far-field ( $\mathbf{F}$ ). However, this expression is coordinate dependent and therefore not a universal definition of stored energies [114].

Since current optimization is used in this thesis, it is required to relate antenna currents to stored energies to determine the Q-factor. It has been proposed in [105] and [37] to use angular frequency derivatives of the reactance matrix (4.25) to compute the stored electric and stored magnetic energies from

the currents as

$$\begin{aligned} W_e &= \frac{1}{4\omega} \mathbf{I}^H \mathbf{X}_e \mathbf{I} = \frac{1}{8} \mathbf{I}^H \left( \frac{\partial \mathbf{X}}{\partial \omega} - \frac{\mathbf{X}}{\omega} \right) \mathbf{I}, \\ W_m &= \frac{1}{4\omega} \mathbf{I}^H \mathbf{X}_m \mathbf{I} = \frac{1}{8} \mathbf{I}^H \left( \frac{\partial \mathbf{X}}{\partial \omega} + \frac{\mathbf{X}}{\omega} \right) \mathbf{I}. \end{aligned} \quad (4.39)$$

It has been shown that these expressions can be equivalently expressed using derivatives with respect to the material surrounding the antenna [81]. More details on this are provided in Chapter 5.

## 4.9 STORED ENERGIES OF MICROSTRIP PATCH ANTENNAS

To determine the stored electric and stored magnetic energies from the currents for microstrip patch antennas, the angular frequency derivative of the dyadic and scalar Green's functions are required. For this, the angular frequency derivative is moved inside the integral under conditions given by Lebesgue's dominated convergence theorem [103]. For the dyadic Green's function (4.8) as [82]

$$\frac{\partial}{\partial \omega} G_A(\rho_{12}) = \frac{1}{4\pi} S_0 \left( \frac{\partial}{\partial \omega} \frac{1}{D_{TE}} \right), \quad (4.40)$$

and for the scalar Green's function (4.8) as

$$\frac{\partial}{\partial \omega} G_V(\rho_{12}) = \frac{1}{4\pi} S_0 \left( \frac{\partial}{\partial \omega} \frac{N}{D_{TE} D_{TM}} \right). \quad (4.41)$$

Once the microstrip patch antenna frequency derivatives of the dyadic and scalar Green's function terms in the Sommerfeld integral have been formulated, the Sommerfeld integral still needs to be applied to them. While the angular frequency derivative removes the spatial singularity, the spectral domain pole still remains. These Sommerfeld integrals present their own challenges. However, their tails can also be handled using the Mosig–Michalski algorithm [70]. These integrals are also specially interpolated using between  $n = 300$  and  $n = 500$  interpolation points (4.12), where  $\rho_{\min} = 0$ . More details on these computations are provided in Paper I.

The expressions to determine the Q-factor for microstrip patch antennas using (4.40) and (4.41) were validated in Paper I. This was done by comparing the Q-factor calculated from the fractional bandwidth (4.36) and frequency derivative of the input impedance (4.37) both from the in-house code as well as a commercial solver, as shown in Figure 6. This was done for both a delta gap fed H-shaped patch antenna (see Figure 2) as well as a microstrip-fed patch antenna [48], as shown in the Figure 6. This indicated that for geometries of interest in this thesis, the derived stored energy results are reliable. The small deviation observed comparing results to the commercial solver for the H-shaped patch is attributed to the difference in feed used.

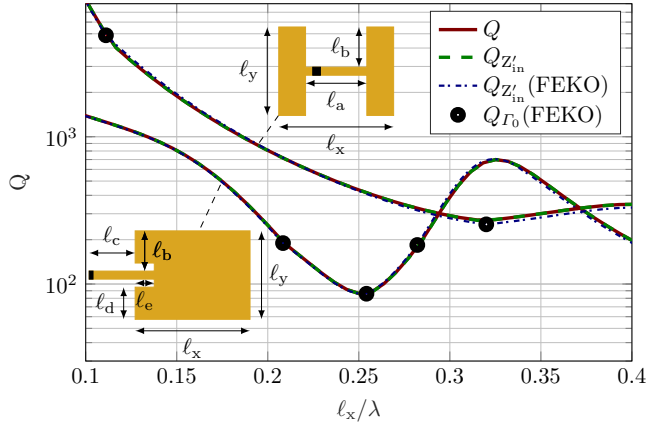


**Figure 6:** Validation of Q-factors computed using the stored energy in (4.39) ( $Q$ ), differentiation of the input impedance (4.37) ( $Q_{Z'_{in}}$ ) and fractional bandwidth (4.36) ( $Q_{R_0}$ ) for H-shaped and rectangular microstrip patch antennas on a dielectric slab with relative permittivity,  $\varepsilon_r = 4$ , dimensions  $h = 0.05\ell_x$ ,  $\ell_y = 0.77\ell_x$ ,  $\ell_a = 7\ell_x/15$ ,  $\ell_b = 5\ell_y/11$ ,  $\ell_c = 2\ell_x/7$ ,  $\ell_d = 7\ell_y/22$ , and  $\ell_e = 5\ell_x/42$ . The Q-factors at self resonances are indicated with markers and are computed from the bandwidth ( $Q_{R_0}$ ). Used from Paper I [80].



# 5

## Material Parameters and Stored Energies



IN this chapter, the links between material parameters and stored energies are described [81, 101]. This is broken into two parts, firstly, how this relationship can be used in the analysis of microstrip patch antennas, is shown in Section 5.1, and, then how this can be used to better understand stored energies in a more general context, is shown in Section 5.2.

### 5.1 RELATING Q-FACTOR TO RADIATION EFFICIENCY

The relationship between stored electric energy and dielectric losses is well established [101]. However, in radiating systems, this link is less straightforward. For microstrip patch antennas (as discussed in Chapter 4), one of the primary loss mechanisms arises from the electric field within the dielectric substrate. This electric field may contribute to losses either through propagating waves or through reactive near fields that lead to losses when interacting with the dielectric loss properties of the substrate.

For the reactive near-field component, the stored electric energy within the dielectric is directly associated with dielectric losses through the loss tangent [48]

$$\tan \delta = \left| \frac{\text{Im } \epsilon_r}{\text{Re } \epsilon_r} \right|. \quad (5.1)$$

Determining the exact proportion of stored electric energy within the substrate is challenging. In the cavity model described in Chapter 3, all stored energy is assumed to be confined within the dielectric substrate. With this assumption, the stored electric energy can be directly related to dielectric losses as  $P \approx 2\omega W_e \tan \delta$ . This approach, however, does not account for propagating waves within the dielectric substrate. This needs to be added, as even when the loss tangent (5.1) is zero, the dissipated power in the dielectric substrate can be

nonzero. Therefore, this leads to

$$P_\epsilon \approx 2\omega W_e \tan \delta + P_{\text{sw}}, \quad (5.2)$$

where  $P_{\text{sw}}$  is in the case of no dielectric losses, the classical surface wave power, and otherwise the propagating power in the dielectric substrate. The result of (5.2) can be added to the dissipated power equation (4.21), resulting in an expression that includes both dissipated and radiated power

$$P_d \approx P_r + P_{\text{sw}} + 2\omega W_e \tan \delta. \quad (5.3)$$

For a self-resonant antenna, where stored electric and magnetic energies are equal, the Q-factor can be expressed as

$$Q = \frac{2\omega W_e}{P_d}. \quad (5.4)$$

Dividing both sides of (5.3) by the dissipated power gives

$$1 \approx \eta + \frac{P_{\text{sw}}}{P_d} + Q \tan \delta, \quad (5.5)$$

that can be rewritten in terms of Q-factor as

$$Q \approx \frac{1}{\tan \delta} - \frac{P_r + P_{\text{sw}}}{P_d \tan \delta}. \quad (5.6)$$

It can be shown that the propagated power to radiated power ratio resembles that of the lossless dielectric, even once losses are added. This is suggested by the results presented in paper II. Therefore, the surface wave-to-radiated power ratio ( $\Delta_{\text{sw}}$ ) can be used to approximate the propagated power from (4.34). This can be used to rewrite (5.6) in terms of radiation efficiency as

$$\eta \approx \frac{1 - Q \tan \delta}{1 + \Delta_{\text{sw}}}. \quad (5.7)$$

This relationship can be used to approximate radiation efficiency from a Q-factor measurement. Furthermore, should a bound be determined on either Q-factor or radiation efficiency, an approximation of a bound on the other is easily determined. This relationship assumes that the Ohmic losses are negligible. However, this is also related to stored energy, as shown in Paper II.

## 5.2 MATERIAL DERIVATIVES AND STORED ENERGIES

As discussed in Section 5.1, there is a direct relationship between stored energies and the corresponding material properties. For example, stored electric energy is associated with permittivity, while stored magnetic energy is associated with permeability. This section explores how perturbations in these material properties influence the stored energies of radiating systems.

In electrostatics and magnetostatics, the relationship between total stored electric and total stored magnetic energies and derivatives with respect to material properties was described by Stratton in the 1940s [101], with similar approaches adopted by others [58,86]. They demonstrated that electrostatic energy is related to the permittivity of the infinite surrounding medium, while magnetostatic energy is similarly connected to permeability. Stratton showed that, under a constant potential, the electric energy increases linearly with a perturbation in permittivity, whereas with a constant charge, electric energy decreases linearly as permittivity increases. In magnetostatics, the magnetic energy exhibits the opposite proportional relationship with changes in permeability.

In electrostatics and magnetostatics, where no radiating field is present, the energy expressions are simplified, being directly linked to the integrals of the fields [101]. This straightforward relationship, however, does not hold for radiating systems, where total electric and total magnetic energies are infinite under far-field assumptions. This raises the question of whether it is possible to define stored electric and magnetic energies in the non-radiating (reactive) field as the part of the electromagnetic field not radiated. Stratton notes that his derivation is not simply applicable to a radiating system as the analogy of force on a body is no longer applicable [101].

Early attempts to quantify stored energy in the reactive field involved subtracting the radiated field component from the total energy [16,61,92], as in expression (4.38). However, as shown in [114], this approach is coordinate-dependent. Another method involves subtracting the Poynting vector [10], but this expression is computationally challenging to evaluate.

In Chapter 4, stored electric and magnetic energies are linked to current distributions [37,105]. There, and in Paper I, this approach is successfully applied to predict the fractional bandwidth of microstrip patch antennas as shown in Figure 6. However, this method sometimes yields indefinite matrices, as shown in [31], which is problematic since energy should be strictly positive, indicating that this approach does not universally define stored energy.

A research question addressed in this thesis is how the stored electric and magnetic energies of a radiating system are related to material properties. Addressing this could provide deeper physical insights into stored energies and clarify the link between stored energies and derivatives with respect to material losses for radiating systems.

To investigate this, one can analyze the dependence of the reactance and resistance matrices on material perturbations by applying material derivatives to the dyadic Green's function (4.2)

$$\mathbf{G} = \left( \mathbf{1} + \frac{1}{\omega^2 \varepsilon_b \mu_b} \nabla \nabla \right) \frac{e^{-j\omega \sqrt{\varepsilon_b \mu_b} R}}{4\pi R}. \quad (5.8)$$

Here, the background permittivity  $\varepsilon_b$  and background permeability  $\mu_b$  represents the infinite space around the radiating structure, allowing all material parameters to be expressed in terms of the background medium, as shown in Figure 7.

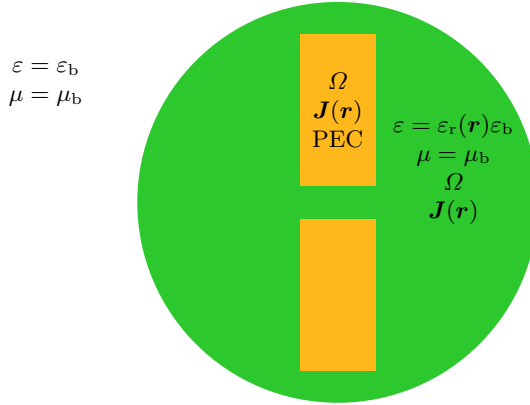


**Figure 7:** The background material, with permittivity  $\varepsilon_b$  and permeability  $\mu_b$ , encloses an antenna region  $\Omega$ , with a PEC conducting region and a dielectric region with permittivity  $\varepsilon_r(\mathbf{r})\varepsilon_b$ . In this chapter, to conserve initially the relative permittivity to wavelength relationship ( $\lambda_\varepsilon = \lambda/\sqrt{\varepsilon_r}$ ), the background permittivity is assumed to have an initial value equal to the free space permittivity. PEC regions have surface current densities, and dielectric regions contrast currents densities, both denoted  $\mathbf{J}(\mathbf{r})$ .

It should be noted that besides this chapter and paper III, the background material is assumed to have the constant permittivity and permeability of free space, therefore conserving the relation between dielectric wavelength and relative permittivity (3.1).

Taking derivatives of the dyadic Green's function (5.8) with respect to the background permittivity  $\varepsilon_b$  and background permeability  $\mu_b$ , yields the following identity as derived in Paper III [81] and given by

$$\varepsilon_b \frac{\partial \mathbf{G}}{\partial \varepsilon_b} = \mu_b \frac{\partial \mathbf{G}}{\partial \mu_b} = \frac{\omega}{2} \frac{\partial \mathbf{G}}{\partial \omega}, \quad (5.9)$$

indicating that the material derivatives of the dyadic Green's function are equivalent to frequency derivatives with a scaling factor. While (5.9) clearly shows the links between frequency derivatives and derivatives with respect to material parameters, the links between these parameters and their stored energies require additional steps. For this, the MoM impedance matrix linked to the Green's dyadic is used.

The MoM impedance matrix (4.3) is proportional to the product of the dyadic Green's function and the background permeability. Taking the material derivatives of this matrix with respect to the background permittivity and background permeability leads to

$$\varepsilon_b \frac{\partial \mathbf{Z}}{\partial \varepsilon_b} = \frac{\omega}{2} \frac{\partial \mathbf{Z}}{\partial \omega} - \frac{\mathbf{Z}}{2} \quad \text{and} \quad \mu_b \frac{\partial \mathbf{Z}}{\partial \mu_b} = \frac{\omega}{2} \frac{\partial \mathbf{Z}}{\partial \omega} + \frac{\mathbf{Z}}{2}. \quad (5.10)$$

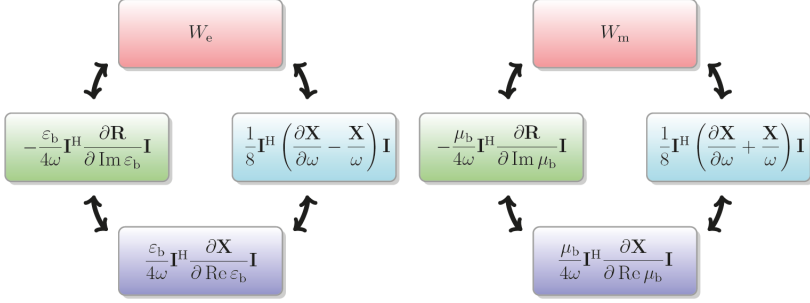


**Figure 8:** Stored electric energy (left) and stored magnetic energy (right) in the limit of no background material losses expressed in terms of derivatives, with respect to frequency, permittivity/permeability, and dielectric/magnetic losses.

Taking the imaginary part of these expressions can be expressed equivalently to the expressions relating currents to stored electric and stored magnetic energies using frequency derivatives (4.39), as

$$W_e = \text{Im} \left( \frac{\varepsilon_b}{4\omega} \mathbf{I}^H \frac{\partial \mathbf{Z}}{\partial \varepsilon_b} \mathbf{I} \right) \quad \text{and} \quad W_m = \text{Im} \left( \frac{\mu_b}{4\omega} \mathbf{I}^H \frac{\partial \mathbf{Z}}{\partial \mu_b} \mathbf{I} \right). \quad (5.11)$$

These expressions can be shown to be equivalent to those of Stratton [101] in the static limit and are equivalent to the stored energy expressions by Vandembosch [105]. Further, while they do not provide a different numerical value for stored energies, they do provide a physical interpretation in terms of the response of the reactive and dissipated power of a radiated system to a perturbation of permittivity or permeability for a fixed current.

Using holomorphic properties of the MoM impedance matrix expressions, Cauchy-Riemann equations [18, 21, 93] and complex derivatives [110] show that in the case of the background material being vacuum, the stored energies can be thought of as the derivative with respect to material losses of the resistance matrix or the real-valued material derivative of the reactance matrix. These expressions are shown in Figure 8 for both stored electric and stored magnetic energies.

The stored energy expressions can be shown to be equivalent to the electrostatic and magnetostatic energies in the static limit as  $\omega \rightarrow 0$ . To better understand how this relates to the statement by Stratton [101], the reactance matrix can be expressed in terms of the material derivatives (5.10) as

$$\mathbf{Z} = \mu_b \frac{\partial \mathbf{Z}}{\partial \mu_b} - \varepsilon_b \frac{\partial \mathbf{Z}}{\partial \varepsilon_b}. \quad (5.12)$$

Taking the derivative of this expression with respect to background permeability leads to

$$\mu_b \frac{\partial \mathbf{Z}}{\partial \mu_b} = \mu_b \frac{\partial \mathbf{Z}}{\partial \mu_b} + \mu_b^2 \frac{\partial^2 \mathbf{Z}}{\partial \mu_b^2} - \mu_b \varepsilon_b \frac{\partial^2 \mathbf{Z}}{\partial \mu_b \partial \varepsilon_b}. \quad (5.13)$$

In the case of magnetostatics, the two terms on the right-hand side can be shown to be equal to zero. This supports the statement that for a constant current, the magnetostatic energy increases linearly with an increase in permeability, meaning the magnetic field remains constant as expected. Taking the derivative with respect to permittivity leads to the expression

$$\varepsilon_b \frac{\partial \mathbf{Z}}{\partial \varepsilon_b} = \varepsilon_b \mu_b \frac{\partial^2 \mathbf{Z}}{\partial \varepsilon_b \partial \mu_b} - \varepsilon_b \frac{\partial \mathbf{Z}}{\partial \varepsilon_b} - \varepsilon_b^2 \frac{\partial^2 \mathbf{Z}}{\partial \varepsilon_b^2}, \quad (5.14)$$

where again the mixed derivative is zero for the case of electrostatics, as the magnetic and electric fields are independent. The second last term in this expression is in the case of electrostatics less than zero or equal to zero when there is no charge. The final term is positive and is linked to the change in the electric field. This confirms the statement that in a constant charge, the electric energy decreases with an increase in permittivity.

From (5.13) it can be shown that

$$\mu_b^2 \frac{\partial^2 \mathbf{Z}}{\partial \mu_b^2} = \mu_b \varepsilon_b \frac{\partial^2 \mathbf{Z}}{\partial \mu_b \partial \varepsilon_b}. \quad (5.15)$$

This can be interpreted that for a steady state current, the change in stored electric energy from a perturbation in permeability is with a scaling factor equal to the change in stored magnetic energy coming from the same perturbation. These terms are zero in the case of electrostatics and magnetostatics, but for a radiating system, they are nonzero.

If one were to hypothetically measure the change in stored electric energy coming from a perturbation of the background permittivity, one would want the measurement to be invariant with respect to any change in stored magnetic energy. This would suggest subtracting the term (5.15) from the permittivity derivative of the impedance matrix (5.14). This would lead to the expression of stored electric energy as [82]

$$\widetilde{W}_e = \text{Im} \left( \frac{\varepsilon_b}{4\omega} \mathbf{I}^H \left( \frac{\partial \mathbf{Z}}{\partial \varepsilon_b} - \mu_b \frac{\partial^2 \mathbf{Z}}{\partial \varepsilon_b \partial \mu_b} \right) \mathbf{I} \right). \quad (5.16)$$

Similarly, one would want the measurement of stored magnetic energy to be invariant with respect to a change in stored electric energy coming from a perturbation of permeability. This would lead to an expression for stored magnetic energy as [82]

$$\widetilde{W}_m = \text{Im} \left( \frac{\mu_b}{4\omega} \mathbf{I}^H \left( \frac{\partial \mathbf{Z}}{\partial \mu_b} - \varepsilon_b \frac{\partial^2 \mathbf{Z}}{\partial \mu_b \partial \varepsilon_b} \right) \mathbf{I} \right). \quad (5.17)$$

Since the subtracted term is zero for the static case, the expressions are still correct for this case. Further, since the same value is subtracted from both the expression for stored electric and stored magnetic energy, the difference remains the reactive energy.

The expressions (5.16) and (5.17) can be rewritten as

$$\widetilde{W}_e = \text{Im} \left( \frac{\varepsilon_b}{4\omega} \mathbf{I}^H \left( -\frac{\partial \mathbf{Z}}{\partial \varepsilon_b} - \varepsilon_b \frac{\partial^2 \mathbf{Z}}{\partial \varepsilon_b^2} \right) \mathbf{I} \right), \quad (5.18)$$

and

$$\widetilde{W}_m = \text{Im} \left( \frac{\mu_b}{4\omega} \mathbf{I}^H \left( \frac{\partial \mathbf{Z}}{\partial \mu_b} - \mu_b \frac{\partial^2 \mathbf{Z}}{\partial \mu_b^2} \right) \mathbf{I} \right), \quad (5.19)$$

respectively. Where the subtracted term can be interpreted as the change in the electric and magnetic field with their associated material derivatives. While the expressions (5.18) and (5.19) may not be an improvement of expressions (5.11), they do nevertheless provide a new interpretation and highlight the complications in validating whether an approach is indeed better. This emphasizes the requirement for an approach of validating new expressions to determine stored energies of radiating systems beyond checking whether they are negative, are correct in the static limit, and recover the reactance. One option would be to ensure that the expressions have a unified interpretation, not only in terms of current but in terms of voltage, that currently does not exist using (5.11).



## Physical Limits on Antennas

**I**T is well known that miniaturizing an antenna generally comes at the cost of many performance metrics [98]. Common performance metrics, as previously mentioned, are radiation efficiency, gain, and bandwidth (determined through the inverse relationship with Q-factor). Determining physical limits on antennas can be traced back to the pioneering work done by Wheeler [109] and Chu [9]. Chu derived an expression for the minimum Q-factor (4.35) of an antenna designed in a circumscribing spherical region, as shown in Figure 9. This simple expression is derived for electrically small antennas from an equivalent lumped-circuit element approach and is valid for linearly polarized single-mode antennas. It is given by

$$Q_{\text{Chu}} = \frac{1}{(ka)^3} + \frac{1}{ka}, \quad (6.1)$$

for a sphere of radius  $a$ . In Chapter 7, it is shown how this bound is not tight for microstrip patch antennas. One reason for the lack of tightness of the bounds on the performance of microstrip patch antennas is that these antennas are planar (nonspherical).

Following the Chu limit, an upper limit on directivity (4.27) was proposed by Harrington [36]. It assumes an acceptable bandwidth, and it is given by

$$D_{\text{Harrington}} = (ka)^2 + 2ka. \quad (6.2)$$

It should be noted that Harrington originally referred to this bound as a bound on gain, however, since it assumes no losses, it is compared to directivity values (4.27) in this thesis. This bound is also for a spherical design region (see Figure 9).

The current optimization formulation used to determine bounds on maximum radiation efficiency, minimum Q-factor, and maximum gain is presented in the following sections of this chapter, with the accompanying results presented in Chapter 7 as well as Paper I and Paper II.

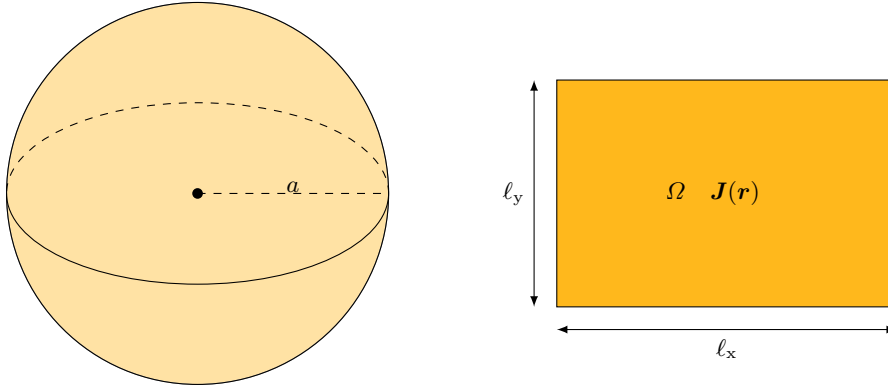


**Figure 9:** The spherical design region with radius  $a$  used to determine the Chu limit ( $Q_{\text{Chu}}$ ) and Harrington directivity bound ( $D_{\text{Harrington}}$ ) on the left. On the right, the planar rectangular design region ( $\Omega$ ) with current density  $\mathbf{J}(\mathbf{r})$  and dimensions  $\ell_x \times \ell_y$ .

## 6.1 QUADRATICALLY CONSTRAINED QUADRATIC PROGRAM

In this thesis, the current optimization problems considered can be written in the form of QCQPs [6]. These optimization problems, as considered in this thesis, take the form

$$\begin{aligned} & \text{maximize} && \mathbf{I}^H \mathbf{A} \mathbf{I} \\ & \text{subject to} && \mathbf{I}^H \mathbf{B} \mathbf{I} \leq 1 \\ & && \mathbf{I}^H \mathbf{C} \mathbf{I} = 0, \end{aligned} \tag{6.3}$$

where the solution is the optimal currents ( $\mathbf{I}$ ).

The optimization problem (6.3) is the primal problem. This problem can be rewritten as a dual problem by first taking the Lagrangian given by

$$L(\mathbf{I}, \nu_1, \nu_2) = -\mathbf{I}^H \mathbf{A} \mathbf{I} + \nu_1 \mathbf{I}^H \mathbf{B} \mathbf{I} - \nu_1 + \nu_2 \mathbf{I}^H \mathbf{C} \mathbf{I}, \tag{6.4}$$

Where  $\nu_1$  and  $\nu_2$  are Lagrange multipliers for the inequality constraint and equality constraint, respectively. By maximizing the Lagrangian with respect to the primal variables, the dual function is obtained. Minimizing this dual function over the multipliers  $\nu_1, \nu_2$  then yields a bound. If the solution of the primal problem and dual problem are equal, then either can be solved. This is referred to as strong duality [6]. For QCQPs having two or fewer quadratic constraints such as (6.3), there is generally strong duality [4]. However, the bounds do not have to be equal, which means there can be a dual gap. Nevertheless, for all results presented in this thesis, there is no dual gap and, therefore, strong duality holds [50].

## 6.2 MAXIMUM RADIATION EFFICIENCY

To maximize radiation efficiency (4.26), both the radiated power (4.32) and dissipated power (4.21) can be expressed in terms of the design region ( $\Omega$ ) currents, see Figure 9. Multiplying the current vector by a non-zero scalar has no impact on the radiation efficiency but scales the radiated and dissipated power by the same amount. Therefore the optimization problem can be expressed as determining the maximum radiated power for dissipated power below a certain threshold as

$$\begin{aligned} & \text{maximize} && \mathbf{I}^H \mathbf{R}_r \mathbf{I} \\ & \text{subject to} && \mathbf{I}^H \mathbf{R} \mathbf{I} \leq 2P_{\text{in}}, \end{aligned} \quad (6.5)$$

where the input power threshold is given by  $P_{\text{in}}$ . Here the equality in (6.3) is not required. As stated before, the dissipated power can be chosen as any arbitrary positive value, however, for simplicity, it is convenient to choose  $2P_{\text{in}} = 1$ . The radiation efficiency can be written in the form of a generalized Rayleigh quotient as

$$\eta = \frac{\mathbf{I}^H \mathbf{R}_r \mathbf{I}}{\mathbf{I}^H \mathbf{R} \mathbf{I}}. \quad (6.6)$$

This problem can further be simplified using a Cholesky decomposition [20] of the resistance matrix as

$$\mathbf{R} = \mathbf{O} \mathbf{O}^H. \quad (6.7)$$

This can then be used to rewrite the generalized Rayleigh quotient as a Rayleigh quotient using the transformation  $\mathbf{K} = \mathbf{O}^{-1} \mathbf{R}_r (\mathbf{O}^H)^{-1}$  as

$$\frac{\tilde{\mathbf{I}}^H \mathbf{K} \tilde{\mathbf{I}}}{\tilde{\mathbf{I}}^H \tilde{\mathbf{I}}}, \quad (6.8)$$

where  $\tilde{\mathbf{I}} = \mathbf{O}^H \mathbf{I}$ . Once in the form of a Rayleigh quotient, since  $\mathbf{K}$  is a Hermitian matrix and can be diagonalized, the expression (6.8) can be expressed as the weighted average of eigenvalues ( $\lambda_m$ ) as

$$\frac{\tilde{\mathbf{I}}^H \mathbf{K} \tilde{\mathbf{I}}}{\tilde{\mathbf{I}}^H \tilde{\mathbf{I}}} = \frac{\sum_{m=1}^M \lambda_m |x_m|^2}{\sum_{m=1}^M |x_m|^2}. \quad (6.9)$$

The maximum eigenvalue of  $\mathbf{K}$  is then the maximum radiation efficiency. This can be written as  $\eta_{\text{up}} = \max \text{eig}(\mathbf{K}) = \max \text{eig}(\mathbf{R}_r, \mathbf{R})$ .

An alternative approach to solving this optimization problem is using the Lagrangian. The Lagrangian [6] of this problem (6.6) is given by

$$L(\mathbf{I}, \nu_1) = -\mathbf{I}^H \mathbf{R}_r \mathbf{I} + \nu_1 \mathbf{I}^H \mathbf{R} \mathbf{I} - \nu_1. \quad (6.10)$$

The Lagrangian dual function can be determined as the minimum value of the Lagrangian. Even when the primal problem is nonconvex the Lagrangian dual is concave. This optimization problem can then be written as

$$\begin{aligned} & \text{minimize} && \nu_1 \\ & \text{subject to} && -\mathbf{R}_r + \nu_1 \mathbf{R} \succeq \mathbf{0}, \end{aligned} \quad (6.11)$$

where  $\nu_1 \geq 0$  as this conserves the positive semidefiniteness of the product of the scalar variable and resistance matrix ( $\nu_1 \mathbf{R}$ ). The problem of finding the minimum of the Lagrangian ( $\nu_1$ ) can then be expressed as the point where the gradients with respect to the Hermitian transpose of the currents equals zero (stationary point) as

$$\frac{\partial L(\mathbf{I}, \nu_1)}{\partial \mathbf{I}^H} = 0 = -\mathbf{R}_r \mathbf{I} + \nu_1 \mathbf{R} \mathbf{I}. \quad (6.12)$$

This is identified as a generalized eigenvalue problem where the current that maximizes the radiated power to dissipated radiated power produces the  $\nu_1$  equal to the maximum radiation efficiency. This is equal to the eigenvalue problem  $\eta_{\text{up}} = \max \text{eig}(\mathbf{R}_r, \mathbf{R})$ .

This problem can further be simplified using Cholesky decomposition (6.7). By using this decomposition, the eigenvalue problem can be written as

$$\eta_{\text{up}} = \max \text{eig}(\mathbf{O}^{-1} \mathbf{R}_r (\mathbf{O}^H)^{-1}) = \max \text{eig}(\mathbf{K}), \quad (6.13)$$

and therefore it is clear that the two approaches produce the same maximum radiation efficiency.

### 6.3 MAXIMUM SELF-RESONANT RADIATION EFFICIENCY

It is often desired to have an antenna be self-resonant to minimize reflected power. This is done by having the reactive power be zero ( $\mathbf{I}^H \mathbf{X} \mathbf{I} = 0$ ). This means that no external tuning through an added capacitance or inductance is required for matching. By adding this constraint, the input reactance would be zero, should this optimal current be excitable with a single feed. This leads to the following optimization problem

$$\begin{aligned} & \text{maximize} && \mathbf{I}^H \mathbf{R}_r \mathbf{I} \\ & \text{subject to} && \mathbf{I}^H \mathbf{R} \mathbf{I} \leq 1 \\ & && \mathbf{I}^H \mathbf{X} \mathbf{I} = 0, \end{aligned} \quad (6.14)$$

where, here, it should be noted that the self-resonant constraint means the search space for the maximum radiation efficiency is reduced. Then (6.14) can be expressed by taking the Lagrangian given by

$$L(\mathbf{I}, \nu_1, \nu_2) = -\mathbf{I}^H \mathbf{R}_r \mathbf{I} + \nu_1 \mathbf{I}^H \mathbf{R} \mathbf{I} - \nu_1 + \nu_2 \mathbf{I}^H \mathbf{X} \mathbf{I}. \quad (6.15)$$

The Lagrangian dual can then be written as

$$\begin{aligned} & \text{minimize} && \nu_1 \\ & \text{subject to} && -\mathbf{R}_r + \nu_1 \mathbf{R} + \nu_2 \mathbf{X} \succeq \mathbf{0}, \\ & && \nu_1 \geq 0, \quad \nu_2 \in \mathbb{R} \end{aligned} \quad (6.16)$$

where the constraint  $\nu_1 \geq 0$  is to ensure the positive semidefiniteness of the product of the scalar variable and the resistance matrix ( $\nu_1 \mathbf{R}$ ). The variable

$\nu_2 \in \mathbb{R}$  can take any real value since it acts on the indefinite reactance matrix. This semidefinite constraint can be written as [23]

$$\mathbf{I}^H(\nu_1 \mathbf{R} + \nu_2 \mathbf{X})\mathbf{I} = \nu_1 \mathbf{I}^H(\nu \mathbf{X} + \mathbf{R})\mathbf{I} \succeq \mathbf{I}^H \mathbf{R}_r \mathbf{I}, \quad (6.17)$$

where  $\nu = \nu_2/\nu_1$ . To have the sum of matrices in (6.15) be positive semidefinite means that  $\nu \mathbf{X} + \mathbf{R} \succeq \mathbf{0}$  [23] as  $\mathbf{0} \succeq -\mathbf{R}_r$ . This leads to the following inequality

$$\nu_1 \geq \frac{\mathbf{I}^H \mathbf{R}_r \mathbf{I}}{\mathbf{I}^H(\nu \mathbf{X} + \mathbf{R})\mathbf{I}} \geq \min_{\nu} \max \text{eig}(\mathbf{R}_r, \nu \mathbf{X} + \mathbf{R}). \quad (6.18)$$

As the reactance matrix is indefinite, the task then becomes to determine over what range of  $\nu$  the sum  $\nu \mathbf{X} + \mathbf{R} \succeq \mathbf{0}$  remains positive semidefinite. For this to be the case, the following condition needs to hold

$$\nu \frac{\mathbf{I}^H \mathbf{X} \mathbf{I}}{\mathbf{I}^H \mathbf{R} \mathbf{I}} \leq -1. \quad (6.19)$$

Since this is in the form of a Raleigh quotient similar to (6.6), the range of  $\nu$  can be calculated as

$$\frac{-1}{\min \text{eig}(\mathbf{X}, \mathbf{R})} \leq \nu \leq \frac{-1}{\max \text{eig}(\mathbf{X}, \mathbf{R})}. \quad (6.20)$$

This range resembles the characteristic modes [38]. After this constraint has been applied, the maximum radiation efficiency with the self-resonant constraint can be expressed as

$$\eta_{\text{ub}} = \min_{\nu} \max \text{eig}(\mathbf{R}_r, \nu \mathbf{X} + \mathbf{R}). \quad (6.21)$$

Writing the radiation resistance matrix in terms of the far field integration matrix (4.32)  $\mathbf{R}_r = \mathbf{F}_s^H \mathbf{F}_s$  means that the eigenvalue problem can be rewritten as

$$\eta_{\text{ub}} = \min_{\nu} \max \text{eig}(\mathbf{F}_s(\mathbf{R} + \nu \mathbf{X})^{-1} \mathbf{F}_s^H). \quad (6.22)$$

It should be noted that this maximum radiation efficiency will be less than or equal to the one determined without the self-resonant constraint (6.13) due to the reduced search space of optimal currents. Further, a simultaneous diagonalization of  $\mathbf{R}$  and  $\mathbf{X}$  can reduce the computational complexity in (6.22) by inverting a diagonal matrix [23].

## 6.4 LOWER BOUNDS ON Q-FACTOR

The lower bounds on Q-factor can be written as a QCQP as

$$\begin{aligned} & \text{maximize} && 2\mathbf{I}^H \mathbf{R} \mathbf{I} \\ & \text{subject to} && \mathbf{I}^H \mathbf{X}_e \mathbf{I} \leq 1 \\ & && \mathbf{I}^H \mathbf{X} \mathbf{I} = 0. \end{aligned} \quad (6.23)$$

This optimization problem formulation maximizes the denominator (disputed power) of the Q-factor expression (4.35) for a constant numerator (stored energy) with self-resonance enforced, and therefore stored electric and stored magnetic energies are equal. Since this optimization problem is in the same form as the maximum radiation efficiency with the self-resonant constraint, it can be handled in the same way leading to

$$1/Q_{\text{lb}} = \min_{\mu} \max \text{eig}(2\mathbf{R}, \mu\mathbf{X} + \mathbf{X}_e). \quad (6.24)$$

It should be noted that for  $0 \leq \mu \leq 1$ , the condition  $\mu\mathbf{I}^H\mathbf{X}\mathbf{I} + \mathbf{I}^H\mathbf{X}_e\mathbf{I} \succeq 0$  ensures that the constraint is positive semidefinite. Since  $\mathbf{I}^H\mathbf{X}\mathbf{I} = \mathbf{I}^H\mathbf{X}_m\mathbf{I} - \mathbf{I}^H\mathbf{X}_e\mathbf{I}$ , performing this substitution of the reactance matrix leads to

$$1/Q_{\text{lb}} = \min_{\mu} \max \text{eig}(2\mathbf{R}, (1 - \mu)\mathbf{I}^H\mathbf{X}_e\mathbf{I} + \mu\mathbf{I}^H\mathbf{X}_m\mathbf{I}). \quad (6.25)$$

It should further be noted that rank-deficient properties of  $\mathbf{R}$  can be used to reduce the computational cost of (6.25).

## 6.5 MAXIMUM GAIN

The optimization problem for maximum gain in a specific direction is chosen in this thesis as the normal direction from the patch on the free space side. This leads to the optimization problem given by

$$\begin{aligned} & \text{maximize} && \mathbf{I}^H\mathbf{F}^H\mathbf{F}\mathbf{I} \\ & \text{subject to} && \mathbf{I}^H\mathbf{R}\mathbf{I} \leq 1 \\ & && \mathbf{I}^H\mathbf{X}\mathbf{I} = 0, \end{aligned} \quad (6.26)$$

and written as an eigenvalue problem similar to (6.22) as

$$G_{\text{ub},r} \approx 4\pi \min_{\nu} \max \text{eig}(\mathbf{F}(\mathbf{R} + \nu\mathbf{X})^{-1}\mathbf{F}^H), \quad (6.27)$$

and the same range for  $\nu$  determined in (6.20) can be used.

# Microstrip Patch Antenna Bounds Results

**T**HIS chapter presents and discusses the results of the bounds formulation presented in Chapter 6. These bounds are also discussed in Paper I and Paper II. The presented bounds are on maximum radiation efficiency, minimum Q-factor, and maximum gain. The bounds are determined for a rectangular design region, as shown in Figure 10, assumed to have dimensions  $\ell_y = 0.77\ell_x$  and substrate thickness  $h = 0.05\ell_x$ , unless otherwise stated.

## 7.1 LOWER Q-FACTOR BOUNDS

The optimization problem used to determine lower Q-factor bounds in Section 6.4, obtained by solving the eigenvalue problem (6.25) is here applied to a patch design region (see Figure 10). The resulting bounds are shown for three substrate permittivities,  $\varepsilon_r \in \{1, 2, 4\}$  across a range of design region electrical sizes ( $\ell_x/\lambda$ ), in Figure 11. No Ohmic or dielectric losses are assumed. Three classical patch antenna geometries are compared to the lower Q-factor bounds as shown in Figure 11, where the black dot is an indication of the probe feed location. The results show that all three classical patch antennas considered, rectangular patches (resonating along either the shorter or longer dimension), slot-loaded patches, and H-shaped patches, are near the limits, determined using the current optimization. As it is shown that some designs perform near the bounds, this emphasizes the bounds as a realistic benchmarking tool.

The Chu limit (6.1) can be determined for the patch design region by taking a design region radius that encloses the patch and its image. For all three relative permittivities, it is evident from the results presented in Figure 10 that the Chu limit differs significantly from the computed bounds across the entire range of electrical sizes ( $\ell_x/\lambda$ ). This is primarily because the design region is nonspherical. Further, it should be noted that the relative permittivity of the substrate is not

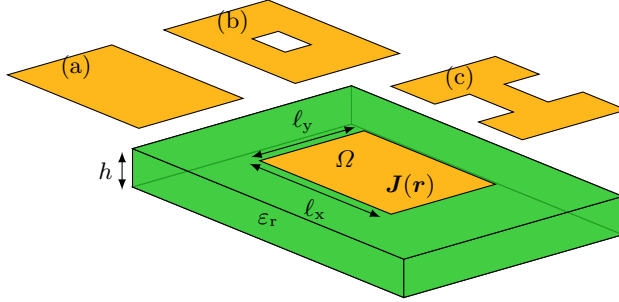


**Figure 10:** Microstrip patch antennas confined to a design region,  $\Omega$ , with side lengths  $\ell_x$  and  $\ell_y$  on top of an infinite dielectric substrate having relative permittivity  $\varepsilon_r$  and thickness  $h$ . The dielectric substrate is on top of an infinite PEC ground plane. Some possible patch geometries fitting within the design region are rectangular patch (a), slot-loaded patch (b), and H-shaped patch (c).

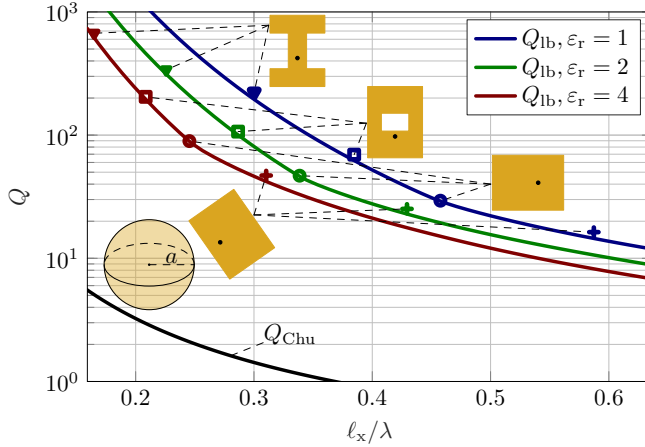


**Figure 11:** Demonstration of the tightness of lower  $Q$ -factor bounds for a rectangular design region  $\Omega$  with aspect ratio  $\ell_y = 0.77\ell_x$ , substrate thickness  $h = 0.05\ell_x$  and relative permittivity  $\varepsilon_r \in \{1, 2, 4\}$  computed using (6.25). FEKO simulation results for self-resonant antenna types (a-c in Figure 10) with  $Q$ -factors from (4.37) are indicated with markers. The H-shaped patch (c) has additional dimensions,  $\ell_a = 0.5\ell_x$  and  $\ell_b = \ell_y/3$ , see Figure 6. To place the new bounds into perspective, the Chu limit ( $Q_{\text{Chu}}$ ) (6.1) is included.

included in the Chu limit. Therefore, the most fair comparison is between the Chu limit and the  $\varepsilon_r = 1$  substrate.

The bounds for the three dielectric substrates shown in Figure 11 indicate that, for a fixed size of the design region, increasing the relative permittivity results in a lower Q-factor. The intuitive explanation is that the half-wavelength resonance, which effectively utilizes the available design region, occurs at a lower frequency for the same physical size patch when the relative permittivity is higher. Another perspective comes from examining the relationship between an increase in permittivity of the surrounding material (as discussed in Section 5.2), which can be interpreted under a constant-current scenario. In alignment with Stratton's electrostatic analysis, increasing the medium's permittivity, while maintaining a constant charge, reduces the stored electric energy. Consequently, near the static limit, this reduction can promote a lower Q-factor in the current optimization formulation. However, the change to other components of the Q-factor should also be considered since increasing the relative permittivity also influences the stored magnetic energy (away from the static limit) and the radiated power, complicating the overall relationship.

When the bounds are instead expressed in terms of the dielectric wavelength  $\ell_x/\lambda_\varepsilon$ , where  $\lambda_\varepsilon = \lambda/\sqrt{\varepsilon_r}$  (3.1), as shown in Figure 12, the bounds obtained for lower relative permittivity exhibit lower Q-factors. However, if the physical size of the design region remains fixed, this corresponds to operating at a higher frequency. Examining the bounds on a log-log scale reveals that the scaling is very similar across all four relative permittivity values ( $\varepsilon_r \in \{1, 2, 4, 10\}$ ). Notably, the scaling changes at around half a wavelength in the dielectric. As shown in Figure 11, the half-wavelength patch Q-factor aligns closely with the bounds. This is used as a starting point when applying the scaling rule presented in Paper I. This approximation of the bounds is shown by the dashed lines, which clearly serve as a good approximation of the bounds, especially for substrates with higher relative permittivity. The scaling rule applied is proportional to  $1/(ka)^5$ , which is in contrast to the scaling of the Chu limit of  $1/(ka)^3$  [9, 80].

An investigation of how surface waves influence the lower Q-factor bounds is shown in Figure 13, which compares the bounds determined both with and without the surface wave contribution ( $Q_{\text{rad}} = Q/\eta$ ). These results indicate that including or excluding the surface waves leads to nearly identical Q-factor bounds showing similar optimal current performance. Furthermore, it is observed that the approximate ratio of surface wave power to radiated power can predict the radiation efficiency using the expression (4.34) as  $\eta_{\text{HED}} = 1/(1 + \Delta_{\text{sw}})$ . However, this approximation becomes less accurate as the electrical size increases. These results indicate that in some cases, the lower Q-factor bounds computed with the surface wave power included can have its radiation efficiency approximated using the approximate ratio between surface wave and radiated power.

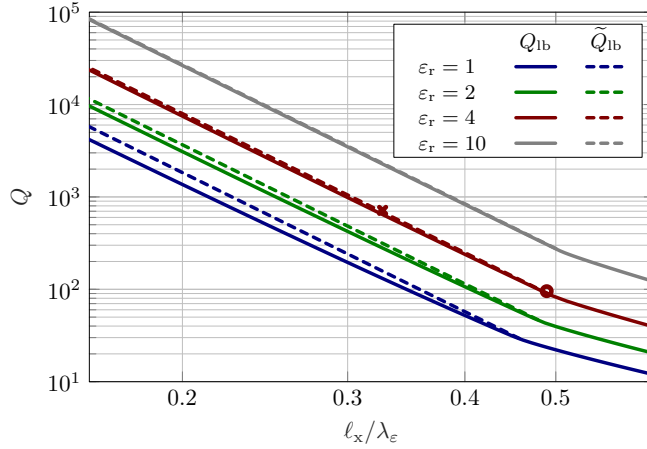


**Figure 12:** Lower Q-factor bounds for rectangular design regions  $\Omega$  with dimensions  $\ell_y = 0.77\ell_x$  and dielectric thickness  $h = 0.05\ell_x$  plotted versus  $\ell_x/\lambda_\epsilon$ . Dashed lines show how the scaling rule approximates the lower Q-factor bounds from simulations of half-wavelength resonant patches. The markers show the Q-factors obtained from simulating a half-wavelength resonant patch antenna as well as the predicted Q-factors from the scaling rule (see Paper I).

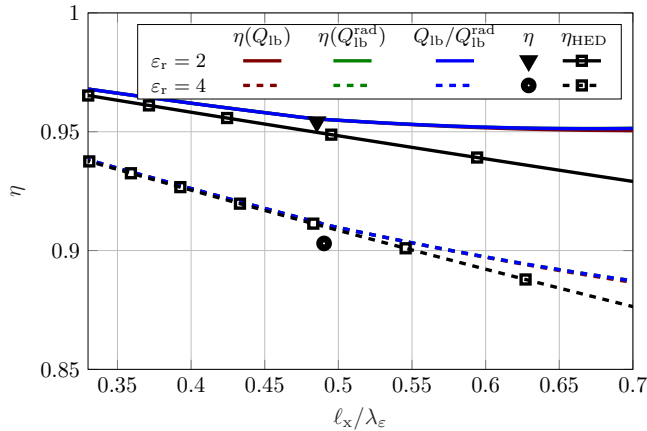


**Figure 13:** Radiation efficiency due to surface-wave losses of lower Q-factor bounds currents for the lossless case given a patch with dimensions  $\ell_y = 0.77\ell_x$  and dielectric thickness  $h = 0.05\ell_x$ . Two relative permittivities  $\epsilon_r \in \{2, 4\}$  are used. For half-wavelength resonant patches, radiation efficiencies calculated with FEKO are shown with markers. The approximate radiation efficiency for a HED (4.34) is also shown for both relative permittivities.

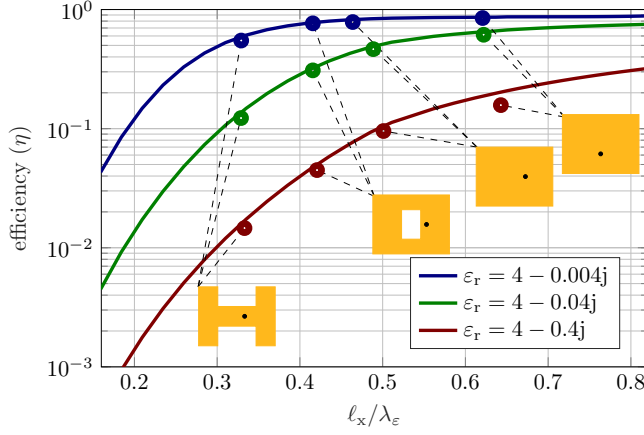


**Figure 14:** Upper bounds on radiation efficiency for all PEC microstrip patch antennas fitting within a rectangular design region  $\Omega$  with dimensions  $\ell_y = 0.77\ell_x$  having dielectric loss tangents  $\tan \delta \in \{0.001, 0.01, 0.1\}$  and substrate thickness  $h = 0.05\ell_x$  (see Figure 10). Radiation efficiencies computed using FEKO are shown by markers for the indicated patch antenna geometries (see insets a-c in Figure 10).

## 7.2 MAXIMUM RADIATION EFFICIENCY

The maximum radiation efficiency bounds presented in Chapter 6 can be applied to microstrip patch antennas, similarly to the lower Q-factor bounds. The first application is to investigate the maximum radiation efficiency when dielectric losses (4.23) are included in the substrate. These bounds are shown in Figure 14 for substrate relative permittivity  $\varepsilon_r = 4$ . The bounds are presented for three loss tangents (5.1),  $\tan \delta \in \{0.001, 0.01, 0.1\}$ . As expected, increasing the dielectric loss tangent reduces the maximum radiation efficiency. The simulated performances of the rectangular, slot-loaded, and H-shaped patches are tight to the computed bounds. However, for a loss tangent of  $\tan \delta = 0.1$ , there is a slight deviation from the bounds for the half-wavelength resonant patch along the  $\ell_y$  dimension. This deviation could potentially be avoided with another patch feed. Furthermore, as the loss tangent increases, the reduction in radiation efficiency for miniaturized designs becomes more pronounced. For instance, at  $\tan \delta = 0.1$ , the H-shaped patch exhibits an efficiency of about 1%, in contrast to approximately 10% for the half-wavelength patch at the same loss tangent.

It should be noted that the non-self-resonant bounds are not presented for the case of dielectric losses. This is because inductive loop currents, which do not radiate in the normal direction, would produce non-practical bounds. Even with low surface resistance on the patch, such loop currents would lead to high Ohmic losses, rendering these non-self-resonant bounds (formulated in Section 6.2) less meaningful. Also, the loop current is a relatively poor radiating mode, this,

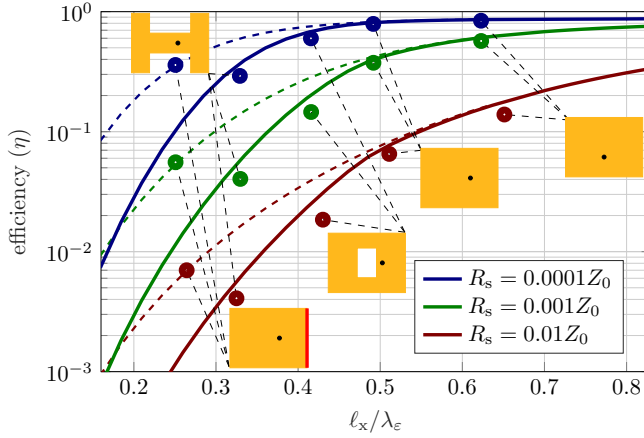


**Figure 15:** Upper bounds on radiation efficiency compared with (6.5) (solid) and without (6.13) (dashed) self-resonant constraint. The bounds are given for varying surface resistivities along with the performance of half-wavelength patch antennas. The design region dimensions are  $\ell_y = 0.77\ell_x$ , the substrate thickness is  $h = 0.05\ell_x$ , and the relative permittivity is  $\epsilon_r = 4$ . Radiation efficiencies for the classical patches shown in Figure 10 computed using FEKO are shown by markers. PIFAs' radiation efficiencies are also shown where the side shorted to the ground is indicated with a red line.

along with high current density on the edges of the patch, means the reduced dielectric losses are traded off against a large increase in Ohmic losses and a comparable decrease in radiated power. This means using loop current as a method to increase radiation efficiency may not have immediate practical value.

The impact of the patch surface resistivity (4.4) on the maximum radiation efficiency is investigated for three surface resistivities, as shown in Figure 15, assuming a dielectric substrate with relative permittivity  $\epsilon_r = 4$ . The bounds are determined both with and without the self-resonant constraint, as formulated in Chapter 6. As expected, a higher surface resistivity results in lower maximum radiation efficiency. It is observed that at and beyond the first half-wavelength resonance, the two bound formulations yield similar results. Furthermore, the performance of a simulated half-wavelength patch is tight to both bounds.

At electrical sizes  $\ell_x/\lambda_\epsilon$  less than  $1/2$ , the bounds computed with and without the self-resonant constraint show a significant difference in Figure 15. This can be attributed to the fact that achieving self-resonance requires modifying the patch geometry for example, by bending it (depicted in Figure 2) as in the slot-loaded or H-shaped patches (see Figure 10). However, a slight discrepancy is observed for the H-shaped patch, indicating that it does not excite the optimal currents. The reason the non-self-resonant bounds perform significantly better can be understood by noting that a planar inverted-F antenna (PIFA) design operates near these bounds. Since the PIFA effectively makes the currents running across the

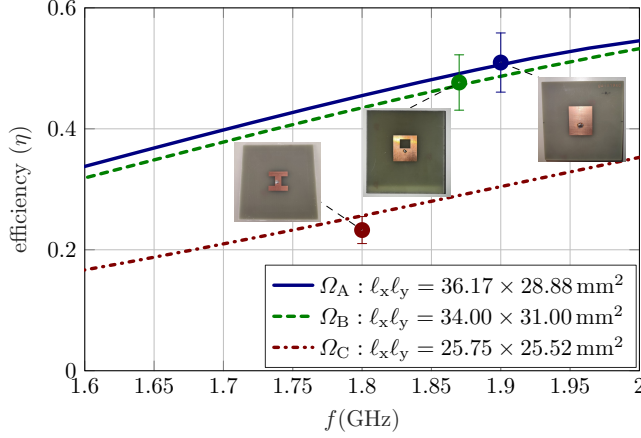


**Figure 16:** Upper bounds on radiation efficiency compared with measurements. The efficiency of three measured antennas is shown with markers. The design regions' dimensions are given in the legend. The relative permittivity of the  $h = 3.3$  mm thick substrate is  $\epsilon_r = 4.29(1 - j0.015)$  and the used surface resistivity of copper is  $R_s = 0.01 \Omega/\square$ . Error bars are based on the precision of the measurement. The ground plane has dimensions  $100 \text{ mm} \times 100 \text{ mm}$ .

patch self-resonant without requiring any material removal (spreading out the currents), it provides a direct path to realizing these improved bounds. It should be noted, however, that while the PIFA design may be considered preferable in this regard, it also requires the addition of vias, making it more challenging to implement. This is discussed in more detail in Paper II.

To emphasize the practical use of the maximum radiation efficiency bounds, they are compared to the performance of measured microstrip patch antennas, as shown in Figure 16. The substrate used for the patch measurements is  $100 \text{ mm} \times 100 \text{ mm}$  with a thickness of  $h = 3.3 \text{ mm}$ . The substrate is assumed to have a relative permittivity  $\epsilon_r = 4.29(1 - j0.015)$ , based on measurements of a similar FR4 substrate at 2 GHz [102]. The surface resistivity is assumed to be similar to copper at  $R_s = 0.01 \Omega/\square$ . The bounds are shown between 1.6 GHz – 2 GHz for three different design regions. They exhibit good agreement with the performance of the half-wavelength, slot-loaded, and H-shaped patches. This demonstrates that the bounds are practically relevant, as they provide a reasonable prediction of measured antenna performances. However, it should be noted that error bars have been added to the measurement results to approximate the effects of manufacturing variations in the design, among other variations. It should be noted that using the Q-factor bounds scaling as demonstrated in Figure 12 and the relationship between Q-factor and radiation efficiency, the measured Q-factor of the half-wavelength rectangular patch was shown to be able to accurately predict its radiation efficiency bounds at lower frequencies as shown in Paper II.

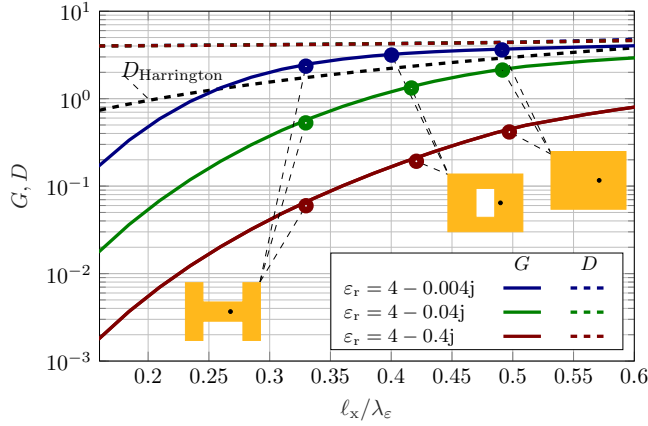


**Figure 17:** Upper bounds on the gain in the normal direction,  $\hat{z}$ , for microstrip patch antennas fitting within a rectangular design region with dimensions  $\ell_y = 0.77\ell_x$ , relative permittivity  $\text{Re}\{\varepsilon_r\} = 4$ , loss tangents  $\tan \delta \in \{0.001, 0.01, 0.1\}$ , and substrate thickness  $h = 0.05\ell_x$ . The corresponding realized directivities are shown by dashed lines.

### 7.3 MAXIMUM GAIN

To evaluate the maximum achievable gain of microstrip patch antennas for three different dielectric loss tangents ( $\tan \delta \in \{0.001, 0.01, 0.1\}$ ), the eigenvalue problem (6.27) is solved for relative permittivity  $\text{Re}\{\varepsilon_r\} = 4$ . As shown in Figure 17, the three classical microstrip patch antenna geometries are shown to be tight to the upper gain bounds for all three considered loss tangents.

The optimal currents derived from the maximum gain bounds can be used to determine the corresponding directivity (4.28), as shown in Figure 17. For all three loss tangents, approximately the same directivity is obtained. This indicates that, for these antennas, the maximum gain is primarily influenced by the radiation efficiency rather than the directivity.

The maximum directivity bounds by Harrington (6.2) is compared to the directivity results for the maximum gain bounds shown in Figure 17, though this comparison comes with certain pitfalls. Harrington's bounds are only meaningful for  $1 \leq ka$ , which approximately corresponds to  $0.5 \leq \ell_x / \lambda_\varepsilon$ . Even beyond this point, the directivity remains higher than Harrington's bound. This occurs because the patch antenna is not a single-mode radiator, thus increasing directivity and leading to the discrepancies. This observation highlights the versatility of the current optimization approach using layered Green's functions over some other techniques. Since a circumscribing sphere is not required and only the design region itself matters, the method is broadly applicable and does not rely on the restrictive assumptions used for Harrington's bound.

## Metasurface Element Designs for Infrared-Based Antenna Measurements



THE design and characterization of metasurfaces have emerged as a promising technique for imaging radiated electromagnetic RF fields. By converting the RF fields into heat and detecting the IR radiation using an IR camera, these metasurfaces can provide a practical and innovative approach to measuring radiating devices [22,78]. This chapter explores the impact of metasurface element designs on their ability to accurately measure RF field distributions and their associated challenges, such as polarization sensitivity, bandwidth performance, and mutual coupling. Three metasurface element designs, dipole, U-shape, and cross potent, are investigated, and their performance in terms of power absorption and field mapping are compared. These insights are important for optimizing IR-based measurement setups and ensuring an accurate representation of the electromagnetic fields from radiating sources.

IR cameras have been employed for RF field measurements for several decades [7, 14, 22, 57, 57, 78], initially using a homogeneous sheet. Recently, metasurfaces with sub-wavelength elements were designed to dissipate power from millimeter waves. This approach still relies on thermal imaging with an IR camera, but it observes the localized heating of metasurface elements rather than a uniform sheet, leading to an increase in emitted IR photons [64]. One key benefit of using metasurfaces over a homogeneous sheet is the former's ability to distinguish between orthogonal polarizations and, therefore, provide extra information. Additionally, this technique has been used to identify defects in the radiating structure under test [65].

The metasurface elements examined in this chapter are planar, similar to patch antennas. The design of these elements significantly influences the performance of the measurement setup. This is as the image captured by the IR camera is correlated with the power dissipated as heat in the metasurface el-

ements. Hence, it is necessary that the elements dissipate detectable amounts of power and effectively receive the component of the electromagnetic field of interest. Unlike antennas where maximum radiation efficiency is desired, the radiation from the metasurface elements is desired to be minimized and dissipated power on the elements maximized.

An example of the measurement setup is shown in Figure 18, where the metasurface is placed between the IR camera and the device under test (source) that produces the RF field. The source field induces a temperature increase in the metasurface, which is then observed by the IR camera as an increase in detected IR photons. Effectively, the metasurface converts the RF field from the source into IR radiation.

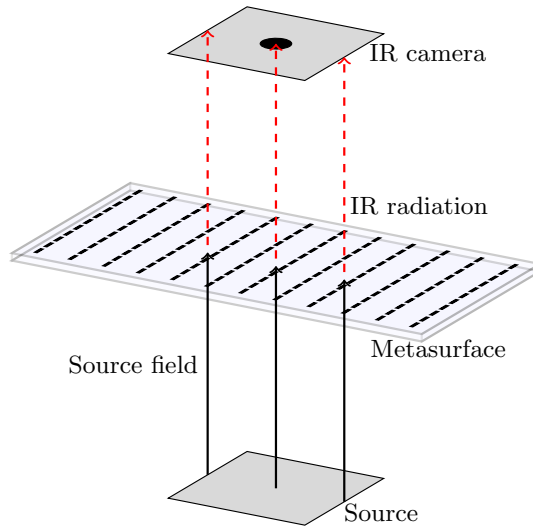


**Figure 18:** The measurement setup with the metasurface placed between the electromagnetic source and the IR camera.

The three metasurface elements considered in this thesis are shown in Figure 19. Each element is designed for operation at a center frequency of 28 GHz, a frequency relevant to 5G communication systems [5]. The elements are the dipole, U-shape, and cross potent. The dipole and U-shape elements are optimized for a  $y$ -polarized field, while the cross potent element is designed to receive both  $x$ - and  $y$ -polarized fields. Each element is situated within a  $5.35 \text{ mm} \times 5.35 \text{ mm}$  unit cell and repeats in an array, as, for example, shown by the dipole array in Figure 18. The surface resistivities of the metasurface elements are  $6.45 \text{ } \Omega/\square$  for the dipole,  $7.3 \text{ } \Omega/\square$  for the U-shape, and  $10.3 \text{ } \Omega/\square$  for the cross potent element.

The elements in Figure 19 are designed so that, at 28 GHz and under the same  $\hat{y}$ -polarized plane-wave illumination in an infinite array configuration, they reflect, transmit, and absorb approximately the same amount of power, as shown in Figure 20. Ideally, the absorbed power should be as large as possible to ensure

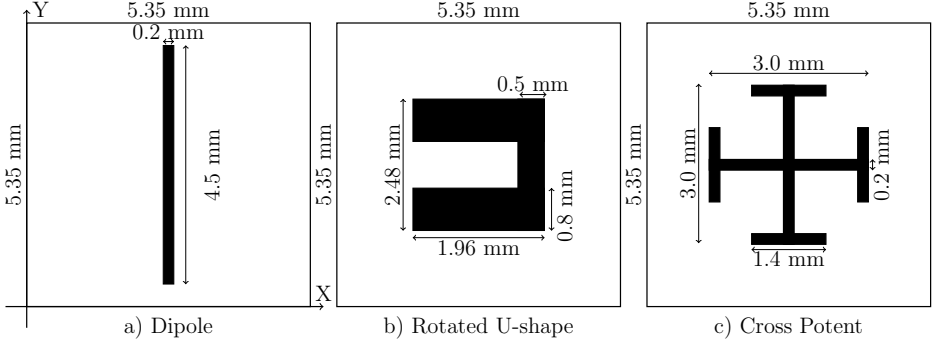


**Figure 19:** The three metasurface elements and their dimensions, each confined within a 5.35 mm  $\times$  5.35 mm unit cell. The surface resistivities are 6.45  $\Omega/\square$  for the dipole, 7.3  $\Omega/\square$  for the U-shape, and 10.3  $\Omega/\square$  for the cross potent element.

a strong IR response that can be imaged using the IR camera. However, this also leads to more reflected power that may interact with the source and other elements, potentially having a significant effect on the measurement results.

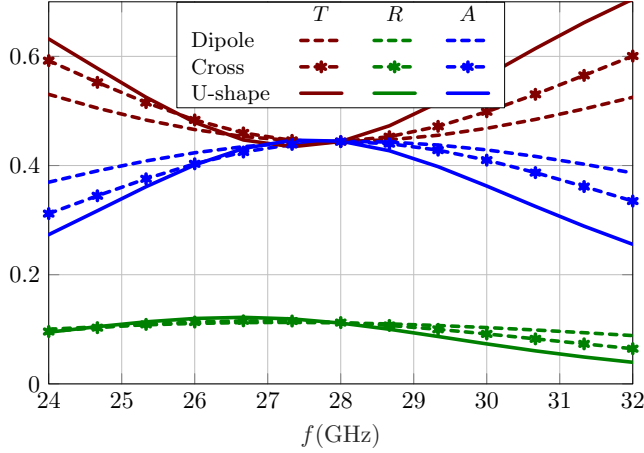


**Figure 20:** Transmittance, reflectance, and absorptance for  $y$ -polarized plane wave over a frequency range for the three elements in Figure 19.

The polarization sensitivity of the metasurface elements is another important factor. While the dipole exhibits strong sensitivity to  $y$ -polarized fields and minimal response to  $x$ -polarized ones, the U-shape element exhibits some undesired coupling to  $x$ -polarized fields. In contrast, the cross potent element's symmetrical design ensures polarization independence between  $x$ - and  $y$ -polarized fields, making it suitable for measurements of both polarizations. Additional polarization properties of the elements are discussed in Paper IV.

To assess the performance of the metasurface, an ideal  $y$ -polarized dipole

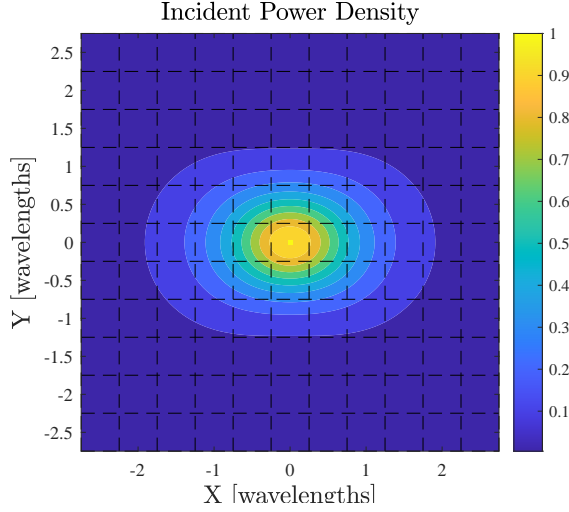


**Figure 21:** Incident power density in the normal direction from a  $\hat{\mathbf{y}}$ -directed ideal electric dipole placed one wavelength below the center.

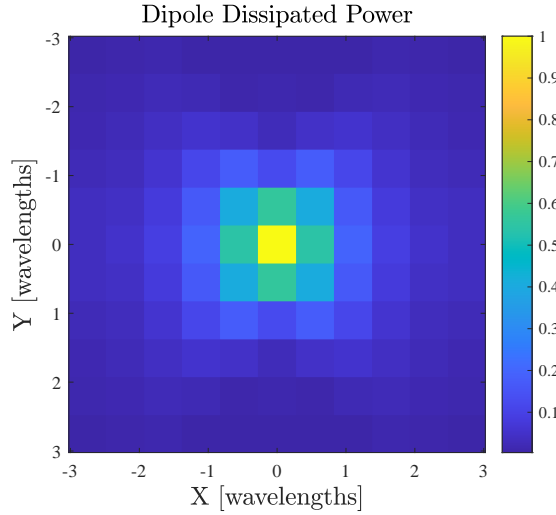


**Figure 22:** Dissipated power in each dipole element (see Figure 19 (a)) of an  $11 \times 11$  element metasurface. The surface is illuminated by an ideal  $\hat{\mathbf{y}}$ -directed electric dipole placed one wavelength below the surface.

source is placed one wavelength below the center element of the surface (see Figure 18). The metasurface is chosen to be  $11 \times 11$  unit cells in size. The incident power density for this dipole on a five-wavelength square region (equal to the  $11 \times 11$  unit cells) is shown in Figure 21. The incident power density in the

normal direction with respect to this region decays rather rapidly outward from the center element. This rapid decay compared to the electric energy density (see Paper IV) is partially due to the Poynting vector moving away from the normal direction as the distance from the center of the region is increased.

The incident power density without the metasurface, shown in Figure 22 (a), is compared to that of a dipole array with elements shown in Figure 19 at 28 GHz. The normalized dissipated power clearly resembles the incident power level from the ideal source. Further, it is shown in Paper IV that  $\hat{x}$ - and  $\hat{y}$ -directed electric energy density have less agreement with the dissipated power on the elements. This is attributed to the interaction between metasurface elements.

Further, in Paper IV, the other two metasurface elements are also shown to have a dissipated power distribution more closely resembling that of the incident power density rather than the electric energy density. Should only a single element be moved in the presence of the field, the dissipated power distribution would more closely resemble that of the electric energy density of the polarization the element is set up to detect. This suggests that reducing the interaction between metasurface elements can be used to better image the electric energy density. This can be achieved by mismatching the elements coming at the cost of less dissipated power. Other element designs or spacing can also be considered.



## Summary and Future Work

**T**HIS thesis establishes new performance limits for microstrip patch antennas by deriving tight bounds on Q-factor, radiation efficiency, and gain. These bounds, numerically compared to well-known antenna geometries and measured design performance, indicate practical benchmarks that guide trade-offs between miniaturization, bandwidth, and efficiency. One of the key contributions is demonstrating that the lower Q-factor bounds derived in this thesis are significantly tighter than the classical Chu limit for microstrip patch antennas. By showing that standard designs approach these tighter bounds, this work confirms their relevance to practical microstrip patch antennas. The derived bounds also scale differently from those of antennas in free space, revealing new scaling rules for microstrip patch antennas.

Beyond these new Q-factor bounds, the thesis introduces radiation efficiency and gain bounds, which provide realistic benchmarks for assessing antenna performance. These bounds highlight important performance trade-offs linked to miniaturization, such as the use of high-permittivity substrates over altering patch design geometry. A notable contribution is a new relationship derived between maximum bandwidth and maximum radiation efficiency, which shows that optimizing one of these parameters often enhances the other. These findings create a clear framework for balancing trade-offs in patch antenna design, emphasizing their practical relevance.

The derived bounds are made more accessible to antenna designers through approximations based on half-wavelength resonant patch antenna simulations or measurements. This allows for practical use even in commercial solvers, enabling the benchmarking of designs against theoretical limits. Several practical scenarios are explored, including how the design frequency, region shape, and dielectric substrate permittivity influence these bounds.

In addition to performance limits, this thesis contributes a deeper material-based understanding of stored energies in radiating systems. An interpretation of stored energies through material derivatives is introduced, showing how electric stored energy relates to a perturbation of permittivity and how stored magnetic

energy relates to a perturbation of permeability. The equivalence of material and frequency derivatives for evaluating Q-factor is demonstrated, offering a broader perspective on stored energy. Further, this relation also links stored energies and material losses to one another in radiating systems.

Finally, the thesis explores a preliminary step toward improving field imaging techniques using metasurfaces combined with IR cameras. This investigation demonstrates how metasurfaces with tailored absorptance, transmittance, and reflectance can offer high-resolution, polarization-sensitive RF field measurements. It is shown that the dissipated power in metasurface elements correlates closely with the incident power density rather than the electric energy density. This work provides more insight into the importance of the choice of metasurface elements for RF field measurements and suggests some application specific choices.

## Future Work

Building on the contribution of this thesis, a number of directions for future research can be pursued, as detailed below.

First, more complex geometries and materials could be considered by extending the current optimization methods to include stacked patches, antennas with shorting pins (PIFA), and alternative design regions such as circular shapes. Investigating the influence of finite ground planes and vertical currents on the derived bounds is an essential next step to refine the models further and extend their applicability. Additionally, incorporating advanced materials with engineered permittivity and permeability could enable further performance enhancements and novel design strategies for miniaturization.

Second, the accessibility of bounds in commercial solvers can be improved. While this thesis provides approximation methods to make performance bounds more accessible, future work could focus on integrating these methods directly into commercial simulation tools. This will enhance the antenna design community's ability to apply these benchmarks to complex scenarios and optimize trade-offs between efficiency, bandwidth, and form factor.

Third, the material-derivative perspective of stored energies offers new opportunities to explore. By adopting more generalized approaches that incorporate realistic material losses and a broader range of antenna configurations, deeper insights into energy storage and loss mechanisms can be gained. These studies could help link stored energy properties to specific design objectives, such as achieving a lower Q-factor or improving efficiency in complex radiating systems.

Lastly, enhanced field-imaging techniques could be explored further. The metasurface-based IR measurement setup offers a promising approach for field imaging, but future efforts could focus on improving resolution and sensitivity. Modifications in metasurface design can further align dissipated power distributions with the underlying field properties in the absence of the metasurface. Along with additional simulations, experimental validation using IR cameras is required to solidify this approach as a viable technique for detailed, polarization-sensitive field measurements. Arbitrary sources and improved calibration techniques could

also be explored to broaden the applicability of this method.

This thesis provides a robust theoretical foundation for understanding and optimizing microstrip patch antennas. By deriving new performance bounds, introducing material-based perspectives on stored energy, and exploring novel field-measurement techniques, it lays the groundwork for advancing the state of the art in antenna design. Future work can build on these contributions to explore more intricate geometries, leverage engineered materials, refine theoretical methods, and improve imaging techniques for electromagnetic fields.



# Bibliography

- [1] M. Aksun and G. Dural. Clarification of issues on the closed-form Green's functions in stratified media. *IEEE Trans. Antennas Propag.*, **53**(11), pp. 3644–3653, 2005.
- [2] Altair. *FEKO*, 2022. [Online] Available: <https://altairhyperworks.com/product/Feko>.
- [3] Antenna Standards Committee of the IEEE Antenna and Propagation Society, The Institute of Electrical and Electronics Engineers Inc., USA. *IEEE Standard Definition of Terms for Antennas*, March 1993. IEEE Std 145-1993.
- [4] A. Beck and Y. C. Eldar. Strong duality in nonconvex quadratic optimization with two quadratic constraints. *SIAM Journal on Optimization*, **17**(3), pp. 844–860, 2006.
- [5] F. Boccardi, R. W. Heath, A. Lozano, T. L. Marzetta, and P. Popovski. Five disruptive technology directions for 5G. *IEEE Communications Magazine*, **52**(2), pp. 74–80, 2014.
- [6] S. P. Boyd and L. Vandenberghe. *Convex Optimization*. Cambridge University Press, 2004.
- [7] K. W. Brown. Far-field antenna pattern measurement using near-field thermal imaging. *IEEE Trans. Antennas Propag.*, **66**(3), pp. 1488–1496, 2018.
- [8] M. Capek, L. Jelinek, and M. Gustafsson. Shape synthesis based on topology sensitivity. *IEEE Trans. Antennas Propag.*, **67**(6), pp. 3889–3901, 2019.
- [9] L. J. Chu. Physical limitations of omni-directional antennas. *Journal of Applied Physics*, **19**, pp. 1163–1175, 1948.

- [10] R. E. Collin and S. Rothschild. Evaluation of antenna Q. *IEEE Trans. Antennas Propag.*, **12**, pp. 23–27, January 1964.
- [11] CST. *Studio Suite 3D EM simulation and analysis software*, 2022. [Online] Available: <https://www.cst.com/>.
- [12] D. B. Davidson. *Computational Electromagnetics for RF and Microwave Engineering*. Cambridge University Press, 2005.
- [13] A. G. Derneryd. Analysis of the microstrip disk antenna element. *IEEE Trans. Antennas Propag.*, **27**(5), pp. 660–664, 1979.
- [14] K. Fan, J. Y. Suen, X. Liu, and W. J. Padilla. All-dielectric metasurface absorbers for uncooled terahertz imaging. *Optica*, **4**(6), pp. 601–604, 2017.
- [15] D. Fang, J. Yang, and G. Delisle. Discrete image theory for horizontal electric dipoles in a multilayered medium. *IEE Proceedings H (Microwaves, Antennas and Propagation)*, **135**, pp. 297–303, 1988.
- [16] R. L. Fante. Quality factor of general ideal antennas. *IEEE Trans. Antennas Propag.*, **17**(2), pp. 151–155, March 1969.
- [17] R. Garg. *Microstrip Antenna Design Handbook*. Antennas and Propagation Library. Artech House, 2001.
- [18] W. Geyi. Stored energies and radiation Q. *IEEE Trans. Antennas Propag.*, **63**(2), pp. 636–645, 2015.
- [19] W. C. Gibson. *The Method of Moments in Electromagnetics*, volume 1. Chapman & Hall/CRC London, UK, 2008.
- [20] G. Golub and C. Van Loan. *Matrix computations (4th Edition)*. the Johns Hopkins University Press, Baltimore, MD, 2013.
- [21] R. E. Greene and S. G. Krantz. *Function Theory of One Complex Variable, (3rd Edition)*. American Mathematical Society, Providence, RI, 2006.
- [22] L. G. Gregoris and K. Iizuka. Thermography in microwave holography. *Applied Optics*, **14**(7), pp. 1487–1489, 1975.
- [23] M. Gustafsson and M. Capek. Maximum gain, effective area, and directivity. *IEEE Trans. Antennas Propag.*, **67**(8), pp. 5282–5293, 2019.
- [24] M. Gustafsson and B. L. G. Jonsson. Antenna Q and stored energy expressed in the fields, currents, and input impedance. *IEEE Trans. Antennas Propag.*, **63**(1), pp. 240–249, 2015.
- [25] M. Gustafsson and B. L. G. Jonsson. Stored electromagnetic energy and antenna Q. *Progress In Electromagnetics Research (PIER)*, **150**, pp. 13–27, 2015.

- 
- [26] M. Gustafsson, A. Karlsson, A. P. Rebelo, and B. Widenberg. Design of frequency selective windows for improved indoor outdoor communication. *IEEE Trans. Antennas Propag.*, **54**, pp. 1897–1900, 2006.
- [27] M. Gustafsson and S. Nordebo. Optimal antenna currents for Q, superdirectivity, and radiation patterns using convex optimization. *IEEE Trans. Antennas Propag.*, **61**(3), pp. 1109–1118, 2013.
- [28] M. Gustafsson, C. Sohl, and G. Kristensson. Physical limitations on antennas of arbitrary shape. *Proc. R. Soc. A*, **463**, pp. 2589–2607, 2007.
- [29] M. Gustafsson. RCS reduction of integrated antenna arrays with resistive sheets. *J. Electromagnet. Waves Appl.*, **20**(1), pp. 27–40, 2006.
- [30] M. Gustafsson, M. Capek, and K. Schab. Tradeoff between antenna efficiency and Q-factor. *IEEE Trans. Antennas Propag.*, **67**(4), pp. 2482–2493, April 2019.
- [31] M. Gustafsson, M. Cismasu, and B. L. G. Jonsson. Physical bounds and optimal currents on antennas. *IEEE Trans. Antennas Propag.*, **60**(6), pp. 2672–2681, 2012.
- [32] E. Hammerstad and O. Jensen. Accurate models for microstrip computer-aided design. In *1980 IEEE MTT-S International Microwave symposium Digest*, pp. 407–409, 1980.
- [33] I. Hanninen, M. Taskinen, and J. Sarvas. Singularity subtraction integral formulae for surface integral equations with RWG, rooftop, and hybrid basis functions. *Progress In Electromagnetics Research*, **63**, pp. 243–278, 2006.
- [34] R. C. Hansen. Fundamental limitations in antennas. *Proc. IEEE*, **69**(2), pp. 170–182, 1981.
- [35] R. F. Harrington. Antenna excitation for maximum gain. *IEEE Trans. Antennas Propag.*, **13**(6), pp. 896–903, Nov. 1965.
- [36] R. F. Harrington. Effect of antenna size on gain, bandwidth, and efficiency. *Journal of Research of the National Bureau of Standards — D. Radio Propagation*, **64**(1), pp. 1–12, 1960.
- [37] R. F. Harrington. *Field Computation by Moment Methods*. Macmillan, New York, NY, 1968.
- [38] R. F. Harrington and J. R. Mautz. Theory of characteristic modes for conducting bodies. *IEEE Trans. Antennas Propag.*, **19**(5), pp. 622–628, 1971.
- [39] R. F. Harrington and J. R. Mautz. Control of radar scattering by reactive loading. *IEEE Trans. Antennas Propag.*, **20**(4), pp. 446–454, 1972.

- [40] M. N. Hasan, S. W. Shah, M. I. Babar, and Z. Sabir. Design and simulation based studies of a dual band u-slot patch antenna for WLAN application. In *2012 14th International Conference on Advanced Communication Technology (ICACT)*, pp. 997–1001, 2012.
- [41] R. L. Haupt and D. H. Werner. *Genetic Algorithms in Electromagnetics*. Wiley-IEEE Press, 2007.
- [42] R. A. Horn and C. R. Johnson. *Topics in Matrix Analysis*. Cambridge University Press, 1991.
- [43] Y. Huang. *Antennas: From Theory to Practice*. Wiley, 2021.
- [44] IEEE Standards Association. IEEE recommended practice for near-field antenna measurements. IEEE Std 1720-2012, 2012.
- [45] W. A. Imbriale, S. S. Gao, and L. Boccia, editors. *Space Antenna Handbook*. Wiley, 2012.
- [46] U. Jakobus and F. Landstorfer. Improved PO-MM hybrid formulation for scattering from three-dimensional perfectly conducting bodies of arbitrary shape. *IEEE Trans. Antennas Propag.*, **43**(2), pp. 162–169, 1995.
- [47] J. R. James and P. S. Hall. Handbook of microstrip antennas. *Peter Peregrinus Ltd*, 1989.
- [48] J. R. James, P. S. Hall, and C. Wood. *Microstrip antenna: theory and design*. IET, 1981.
- [49] L. Jelinek and M. Capek. Optimal currents on arbitrarily shaped surfaces. *IEEE Trans. Antennas Propag.*, **65**(1), pp. 329–341, 2017.
- [50] L. Jelinek, J. Liska, M. Capek, V. Losenicky, and M. Gustafsson. Maximum radiation efficiency of implanted antennas employing a novel hybrid method. In *2021 IEEE International Symposium on Antennas and Propagation and USNC-URSI Radio Science Meeting (APS/URSI)*, pp. 1339–1340, 2021.
- [51] J. M. Jin. *Theory and Computation of Electromagnetic Fields*. Wiley, 2011.
- [52] J. M. Jin. *The Finite Element Method in Electromagnetics*. IEEE Press. Wiley, 2015.
- [53] B. L. G. Jonsson, S. Shi, L. Wang, F. Ferrero, and L. Lizzi. On methods to determine bounds on the  $Q$ -factor for a given directivity. *IEEE Trans. Antennas Propag.*, **65**(11), pp. 5686–5696, 2017.
- [54] M. U. Khan, M. S. Sharawi, and R. Mittra. Microstrip patch antenna miniaturisation techniques: a review. *IET Microwaves, Antennas & Propagation*, **9**(9), pp. 913–922, 2015.

- 
- [55] V. Kourkoulos and A. Cangellaris. Accurate approximation of Green's functions in planar stratified media in terms of a finite sum of spherical and cylindrical waves. *IEEE Trans. Antennas Propag.*, **54**(5), pp. 1568–1576, 2006.
- [56] G. Kristensson. *Scattering of Electromagnetic Waves by Obstacles*. SciTech Publishing, an imprint of the IET, Edison, NJ, 2016.
- [57] S. A. Kuznetsov, A. G. Paulish, A. V. Gelfand, P. A. Lazorskiy, and V. N. Fedorinin. Bolometric THz-to-IR converter for terahertz imaging. *Applied Physics Letters*, **99**(2), 2011.
- [58] L. D. Landau and E. M. Lifshitz. *Electrodynamics of Continuous Media (1st Edition)*. Pergamon Press, Oxford, 1960.
- [59] K. F. Lee and K. M. Luk. *Microstrip patch antennas*. World Scientific, 2011.
- [60] K. F. Lee and K. F. Tong. Microstrip patch antennas — basic characteristics and some recent advances. *Proc. IEEE*, **100**(7), pp. 2169–2180, 2012.
- [61] C. Levis. A reactance theorem for antennas. *Proceedings of the IRE*, **45**(8), pp. 1128–1134, 1957.
- [62] J. Liu, Q. Xue, H. Wong, H. W. Lai, and Y. Long. Design and analysis of a low-profile and broadband microstrip monopolar patch antenna. *IEEE Trans. Antennas Propag.*, **61**(1), pp. 11–18, 2012.
- [63] R. Luebbers, D. Steich, and K. Kunz. FDTD calculation of scattering from frequency-dependent materials. *IEEE Trans. Antennas Propag.*, **41**(9), pp. 1249–1257, 1993.
- [64] J. Lundgren, M. Gustafsson, D. Sjöberg, and M. Nilsson. IR and metasurface based mm-wave camera. *Applied Physics Letters*, **118**(18), pp. 184104, 2021.
- [65] J. Lundgren, T. Martin, H. Khalid, M. Zabihipour, D. Tu, I. Engquist, D. Sjöberg, and M. Gustafsson. Real-time near-field mmWave measurements using screen-printed metasurfaces and IR camera. *TEAT Technical Report*, **7282**, pp. 1–26, 2024.
- [66] S. McKinley and M. Levine. Cubic spline interpolation. *College of the Redwoods*, **45**(1), pp. 1049–1060, 1998.
- [67] J. S. McLean. A re-examination of the fundamental limits on the radiation  $Q$  of electrically small antennas. *IEEE Trans. Antennas Propag.*, **44**(5), pp. 672–676, May 1996.

- [68] K. Michalski. Extrapolation methods for Sommerfeld integral tails. *IEEE Trans. Antennas Propag.*, **46**(10), pp. 1405–1418, 1998.
- [69] K. A. Michalski and J. R. Mosig. Discrete complex image mixed-potential integral equation analysis of microstrip patch antennas with vertical probe feeds. *Electromagnetics*, **15**(4), pp. 377–392, 1995.
- [70] K. A. Michalski and J. R. Mosig. Efficient computation of Sommerfeld integral tails — methods and algorithms. *Journal of Electromagnetic Waves and Applications*, **30**(3), pp. 281–317, 2016.
- [71] J. R. Mosig. Closed formula for the static three-dimensional Green function in microstrip structures. *Electronics Letters*, **14**, pp. 544–546, 1978.
- [72] J. R. Mosig. Integral equation techniques for 3D microstrip structures. *Review of Radio Science*, pp. 127–153, 1993.
- [73] J. R. Mosig, R. C. Hall, and F. E. Gardiol. Numerical analysis of microstrip patch antennas. In *Handbook of Microstrip Antennas*, J. R. James and P. S. Hall, Editors, pp. 391–453. London: Peregrinus, 1989.
- [74] J. Mosig. Arbitrarily shaped microstrip structures and their analysis with a mixed potential integral equation. *IEEE Transactions on Microwave Theory and Techniques*, **36**(2), pp. 314–323, 1988.
- [75] J. R. Mosig and F. E. Gardiol. A dynamical radiation model for microstrip structures. In *Advances in Electronics and Electron Physics*, P. W. Hawkes, Editor, volume 59, pp. 139 – 237. Academic Press, 1982.
- [76] J. R. Mosig and K. A. Michalski. Sommerfeld integrals and their relation to the development of planar microwave devices. *IEEE Journal of Microwaves*, **1**(1), pp. 470–480, 2021.
- [77] R. Munson. Conformal microstrip antennas and microstrip phased arrays. *IEEE Trans. Antennas Propag.*, **22**(1), pp. 74–78, 1974.
- [78] K. Muzaffar, L. I. Giri, K. Chatterjee, S. Tuli, and S. Koul. Fault detection of antenna arrays using infrared thermography. *Infrared Physics & Technology*, **71**, pp. 464–468, 2015.
- [79] B. A. P. Nel and M. M. Botha. An efficient MLACA-SVD solver for superconducting integrated circuit analysis. *IEEE Transactions on Applied Superconductivity*, **29**(7), pp. 1–10, 2019.
- [80] B. A. P. Nel, A. K. Skrivervik, and M. Gustafsson. Q-factor bounds for microstrip patch antennas. *IEEE Trans. Antennas Propag.*, **71**(4), pp. 3430–3440, 2023.

- 
- [81] B. A. P. Nel, A. K. Skrivervik, and M. Gustafsson. Stored energies and Q-factor expressed in material derivatives. *IEEE Antennas and Wireless Propagation Letters*, **23**(1), pp. 19–23, 2024.
  - [82] B. A. P. Nel, A. K. Skrivervik, and M. Gustafsson. Radiation efficiency and gain bounds for microstrip patch antennas. *IEEE Trans. Antennas Propag.* (Early Access), 2024.
  - [83] B. A. P. Nel, A. K. Skrivervik, J. Lundgren, and M. Gustafsson. Impact of meta-surface element designs on infrared-based antenna near-field measurements. In *Proceedings of the 19th European Conference on Antennas and Propagation (EuCAP)*, 2025. Accepted.
  - [84] V. I. Okhmatovski and A. C. Cangellaris. A new technique for the derivation of closed-form electromagnetic Green’s functions for unbounded planar layered media. *IEEE Trans. Antennas Propag.*, **50**(7), pp. 1005–1016, 2002.
  - [85] V. Palanisamy and R. Garg. Analysis of arbitrarily shaped microstrip patch antennas using segmentation technique and cavity model. *IEEE Trans. Antennas Propag.*, **34**(10), pp. 1208–1213, 1986.
  - [86] W. K. Panofsky and M. Phillips. *Classical Electricity and Magnetism (2nd Edition)*. Addison-Wesley, Reading, MA, 1962.
  - [87] A. Peterson. *Mapped Vector Basis Functions for Electromagnetic Integral Equations*. Synthesis Lectures on Computational Electromagnetics. Springer International Publishing, 2022.
  - [88] D. M. Pozar. Microstrip antenna. *Proceedings of the IEEE*, **80**(1), pp. 79–91, 1992.
  - [89] D. M. Pozar. New results for minimum Q, maximum gain, and polarization properties of electrically small arbitrary antennas. In *Proceedings of the 3rd European Conference on Antennas and Propagation (EuCAP)*, pp. 1993–1996, March 2009.
  - [90] Q. I. Rahman and G. Schmeisser. Characterization of the speed of convergence of the trapezoidal rule. *Numerische Mathematik*, **57**, pp. 123–138, 1990.
  - [91] Y. Rahmat-Samii and E. Michielssen. *Electromagnetic Optimization by Genetic Algorithms*. Wiley Series in Microwave and Optical Engineering. John Wiley & Sons, 1999.
  - [92] D. R. Rhodes. Observable stored energies of electromagnetic systems. *Journal of the Franklin Institute*, **302**(3), pp. 225–237, 1976.
  - [93] D. Rhodes. A reactance theorem. *Proceedings of the Royal Society of London. A. Mathematical and Physical Sciences*, **353**(1672), pp. 1–10, 1977.

- [94] W. Richards, Y. Lo, and D. Harrison. An improved theory for microstrip antennas and applications. *IEEE Trans. Antennas Propag.*, **29**(1), pp. 38–46, 1981.
- [95] K. Schab, L. Jelinek, M. Capek, C. Ehrenborg, D. Tayli, G. A. Vandenbosch, and M. Gustafsson. Energy stored by radiating systems. *IEEE Access*, **6**, pp. 10553 – 10568, 2018.
- [96] M. Shafi, A. F. Molisch, P. J. Smith, T. Haustein, P. Zhu, P. De Silva, F. Tufvesson, A. Benjebbour, and G. Wunder. 5G: A tutorial overview of standards, trials, challenges, deployment, and practice. *IEEE Journal on Selected Areas in Communications*, **35**(6), pp. 1201–1221, 2017.
- [97] I. Singh and V. S. Tripathi. Micro strip patch antenna and its applications: a survey. *Int. J. Comp. Tech. Appl*, **2**(5), pp. 1595–1599, 2011.
- [98] A. K. Skrivervik, J.-F. Zürcher, O. Staub, and J. R. Mosig. PCS antenna design: The challenge of miniaturization. *IEEE Antennas Propag. Mag.*, **43**(4), pp. 12–27, August 2001.
- [99] W. E. Smith. The energy storage of a prescribed impedance. *Proceedings of the Royal Society of New South Wales*, **102**, pp. 203–218, 1969.
- [100] A. Sommerfeld. Über die Ausbreitung der Wellen in der drahtlosen Telegraphie. *Annalen der Physik*, **333**, pp. 665–736, 1909.
- [101] J. A. Stratton. *Electromagnetic Theory*. McGraw-Hill, New York, NY, 1941.
- [102] Y. Su, M. Pellaton, C. Affolderbach, G. Miletì, and A. K. Skrivervik. Mode suppression and homogeneous field bandwidth enhancement of a tuning-free micro-loop-gap resonator using FR4 for chip-scale rubidium clock. *IEEE Trans. Microwave Theory Tech.*, pp. 1–11, 2024.
- [103] E. Talvila. Necessary and sufficient conditions for differentiating under the integral sign. *The American Mathematical Monthly*, **108**(6), pp. 544–548, 2001.
- [104] D. Tayli and M. Gustafsson. Physical bounds for antennas above a ground plane. *IEEE Antennas Wireless Propag. Lett.*, **15**, pp. 1281–1284, 2016.
- [105] G. A. E. Vandenbosch. Reactive energies, impedance, and Q factor of radiating structures. *IEEE Trans. Antennas Propag.*, **58**(4), pp. 1112–1127, 2010.
- [106] G. Vecchi. Loop-star decomposition of basis functions in the discretization of the EFIE. *IEEE Trans. Antennas Propag.*, **47**(2), pp. 339–346, February 1999.

- 
- [107] J. J. H. Wang. *Generalized Moment Methods in Electromagnetics: Formulation and Computer Solution of Integral Equations*. John Wiley & Sons, New York, NY, 1991.
  - [108] R. Waterhouse. Microstrip patch antennas. In *Handbook of Antennas in Wireless Communications*, pp. 6–1. CRC Press, 2018.
  - [109] H. A. Wheeler. Fundamental limitations of small antennas. *Proc. IRE*, **35**(12), pp. 1479–1484, 1947.
  - [110] W. Wirtinger. Zur formalen Theorie der Funktionen von mehr komplexen Veränderlichen. *Mathematische Annalen*, **97**, pp. 357–376, 1927.
  - [111] A. D. Yaghjian, M. Gustafsson, and B. L. G. Jonsson. Minimum  $Q$  for lossy and lossless electrically small dipole antennas. *Progress In Electromagnetics Research*, **143**, pp. 641–673, 2013.
  - [112] A. D. Yaghjian, T. H. O'Donnell, E. E. Altshuler, and S. R. Best. Electrically small supergain end-fire arrays. *Radio Science*, **43**(3), pp. 1–13, May 2008.
  - [113] A. D. Yaghjian and H. R. Stuart. Lower bounds on the  $Q$  of electrically small dipole antennas. *IEEE Trans. Antennas Propag.*, **58**(10), pp. 3114–3121, 2010.
  - [114] A. D. Yaghjian and S. R. Best. Impedance, bandwidth, and  $Q$  of antennas. *IEEE Trans. Antennas Propag.*, **53**(4), pp. 1298–1324, 2005.
  - [115] J.-F. Zürcher and F. E. Gardiol. *Broadband Patch Antennas*. Artech House, Boston, MA, 1995. ISBN 0-89006-777-5.



**PAPERS**



# Paper I

# Paper I

*Reproduced, with permission, from: IEEE*

B. A. P. Nel, A. K. Skrivervik, and M. Gustafsson. Q-factor Bounds for Microstrip Patch Antennas. Transactions on Antennas and Propagation, 71(4), pp. 3430– 3440, 2023. doi: 10.1109/TAP.2023.3243726.

# Q-factor Bounds for Microstrip Patch Antennas

Ben A.P. Nel, Anja K. Skrivervik, and Mats Gustafsson, *Senior Member, IEEE*

## Abstract

Antenna bounds are a useful tool in assessing feasibility or performance of an antenna design. Microstrip patch antennas are often limited by their relatively narrow bandwidth, and therefore Q-factor is an important design parameter, as it is related to the inverse of the fractional bandwidth. This paper presents the first tight lower Q-factor bounds on microstrip patch antennas supported by an infinite dielectric substrate. The derived lower Q-factor bounds are orders of magnitude tighter than the Chu limit and introduce a new scaling rule. These bounds consider all possible geometries on the predefined design region. Moreover, it is shown that well known patch antennas have Q-factors near the bounds and have thus a near optimal bandwidth. The computation of the bounds is done using a method of moments formulation. However, an approximation to these bounds using commonly available simulation tools is provided.

## Index Terms

Optimization, microstrip patch antennas, Q-factor, method of moments, Sommerfeld integrals, physical bounds.

## I. INTRODUCTION

Microstrip patch antenna technology saw a rapid development in the late 1970s [1], [2] partially driven by their low-cost and ease of fabrication. Modeling of these antennas soon followed, and reliable models showing good agreement with measurements became available by the early 1980s [3]. These models allowed antenna designers to improve performance parameters, such as bandwidth.

Corresponding author: Ben A.P. Nel.

This work was supported by the Swedish Research Council (2017-04656) and the Hedda Andersson guest professor program at Lund University.

Ben A.P. Nel and Mats Gustafsson are with the Department of Electrical and Information Technology, Lund University, SE-221 00 Lund, Sweden (e-mail: {ben.nel,mats.gustafsson}@eit.lth.se).

Anja K. Skrivervik is with the Microwave Antenna Group, École Polytechnique Fédérale de Lausanne (EPFL), 1015 Lausanne, Switzerland and the Department of Electrical and Information Technology, Lund University, SE-221 00 Lund, Sweden (e-mail: anja.skrivervik@epfl.ch).

Microstrip patch antennas are still in wide use today and can be modeled using commercial software *e.g.*, FEKO or CST [4], [5].

Due to the narrowband nature of microstrip antennas, the Q-factor, that is inversely proportional to the fractional bandwidth, is an important design parameter [6]. Bandwidth and Q-factor can be computed for a given design [7] and are then generally optimized by varying parameters using, *e.g.*, heuristic methods [8], [9]. While this is a reliable design approach, it is time-consuming and often obtains local optima rather than a desired global optimum.

Since lower Q-factor bounds of microstrip patch antenna designs are of particular interest, an approach to compute these bounds (also referred to as limit) is presented here. This allows designers to assess the feasibility of reaching a required bandwidth within a specified design region. These bounds also provide benchmarks, in the design process, and when evaluating designs from literature.

A physical bound on Q-factor was derived by Chu [10] in the late 1940s. This bound, applicable to small antennas enclosed by a sphere, radiating into free space, is generally known to be unobtainable for microstrip patch antenna designs due to the latter's form factor. Obtaining tight bounds on several parameters for arbitrarily shaped antennas has successfully been done, using current optimization on antennas made of conductors having no dielectric substrate [11], [12], [13], [14], [15]. Amongst all possible currents, the optimal one produces the lowest possible Q-factor.

In order to determine lower Q-factor bounds, all possible design geometries need to be considered. The performance of these design geometries can be computed from their underlying current distribution. To compute Q-factor, this current distribution is linked to stored energy and radiated power. Thus, a natural method to compute lower Q-factor bounds is to optimize over all possible current distributions on the antenna design region. Conveniently, these currents are the unknowns in the method of moments (MoM) formulation. A similar formulation would be very difficult in a semi-analytic method *e.g.*, cavity model or numerical methods such as finite element method (FEM) or finite-difference time-domain (FDTD), where the natural unknowns are the fields. Using current optimization with MoM, lower Q-factor bounds are computed by eigenvalue problems.

Microstrip patch antennas can be analyzed numerically, for instance with an integral equation formulation using MoM [3]. If the ground plane and dielectric slab are assumed to be infinite, their effect can be accounted for implicitly in the Green's function, given by Sommerfeld integrals [16]. In this case, the unknowns of the problem are only the currents on the patch, providing a computational advantage over methods, where also the ground plane and dielectric regions need to be discretized [17]. It should be noted that while in reality the ground plane is always finite, comparative studies [18] have found the assumption of an infinite ground plane to be a fair approximation of reasonably large ground planes.

Here, the original definition of a microstrip patch antenna is used, in that a single dielectric layer having all currents horizontally on the patch is assumed. These antennas are typically fed with a vertical feeding pin. While shorting pins, stacked patches or miniaturized ground planes [19], [20], [21] can be used to enhance the bandwidth, they are not considered here. Further, it is also assumed that there is only one dominant resonance over the bandwidth. Patches similar to the ones presented here are in wide use due to their simplicity and low cost.

This paper presents a method to determine an upper limit on achievable bandwidth for microstrip patch antennas. These bounds account for all possible geometries within a predefined design region, thereby obtaining a performance limit to compare miniaturized patch designs with. Obtained bounds are shown to be tight (near) to the performance of some practical antenna designs. As the computation of the bounds requires a MoM formulation, it is also shown that an approximation of the bounds can be obtained requiring only the simulation of a half-wavelength patch antenna. The bounds are formulated in Q-factor which is an accurate estimate of achievable bandwidth given a single dominant resonance over the bandwidth [7]. These bounds build on [22] by allowing for the addition of a dielectric substrate. This non-trivial addition makes the bounds more relevant for microstrip antenna designers, where a dielectric is usually required.

Section II presents the microstrip patch antenna formulation that is used to compute bounds. Section III validates expressions derived to compute Q-factor. Section IV shows how to compute lower Q-factor bounds and Section V provides a method to predict bounds based on simulating half-wavelength resonant patch antennas. Then, in Section VI, practical examples of the proposed bounds and comparisons with patch antennas are shown. Section VII concludes the paper. Finally, the Appendices provide additional information on Sommerfeld integrals and low-frequency Q-factor scaling.

## II. MICROSTRIP PATCH ANTENNA MODEL

In this paper, microstrip patch antennas are modeled by assuming an infinite PEC ground plane and an infinite lossless dielectric substrate. On top of the substrate is a PEC patch confined to a design region  $\Omega$ , *e.g.*, a rectangle with side lengths  $\ell_x$  and  $\ell_y$ , see Figure 1. The presence of the dielectric layer affects the microstrip patch antenna performance in several ways leading to a non-trivial relationship between dielectric permittivity and Q-factor. The combination of these effects with the widespread applications emphasizes the importance of adding a dielectric to the Q-factor formulations developed in the past [22], [23] that use image theory to account for an infinite ground plane but do not consider the dielectric substrate.

Some classical patch antenna geometries constructed within a rectangular design region  $\Omega$  are shown in Figure 1. The rectangular patch (a) is resonant

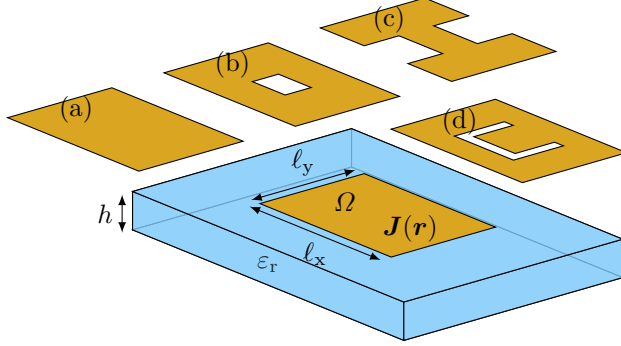


Figure 1: Microstrip patch antennas confined to a design region,  $\Omega$ , with side lengths  $\ell_x$  and  $\ell_y$  on top of an infinite dielectric substrate having relative permittivity  $\varepsilon_r$  and thickness  $h$ . The dielectric substrate is on top of an infinite PEC ground plane. Some possible patch geometries fitting within the design region are rectangular patch (a), slot loaded patch (b), H-shaped patch (c), and U-slot patch (d).

around half-a-wavelength [1] in the dielectric. A lower resonance frequency is obtained by slot loading (b) effectively lengthening the current path and miniaturizing the patch [24]. For further miniaturization the H-shaped patch (c) can be used [24]. Dual resonances can be obtained with the U-slot patch (d) [25]. These patches can be constructed by removing metal from the rectangular design region and then the radiated field is determined by the current density  $\mathbf{J}(\mathbf{r})$  on the remaining metal part. This enables modeling of antenna parameters such as Q-factor and gain from all patch geometries within the design region  $\Omega$  by identifying non-metal regions with current density  $\mathbf{J}(\mathbf{r}) = \mathbf{0}$ .

In this paper, lower bounds on the Q-factor for microstrip patch antennas are determined by optimizing over current densities  $\mathbf{J}(\mathbf{r})$  in  $\Omega$  for given height ( $h$ ), relative permittivity ( $\varepsilon_r$ ), and frequency ( $f$ ), see Figure 1. These bounds implicitly account for all possible patch geometries within the design region ( $\Omega$ ), such as (a)-(d) in Figure 1. Since the bounds are tailored to microstrip patch antennas, they can be tight to designs.

Here, it is important to emphasize the key difference between a method to compute the performance of a given structure, as opposed to the bounds for a given design region. For a given structure and excitation, analyzing microstrip patch antennas is well understood [3]. For instance using a commercial solver. In contrast, bounds for a given design region rather computes a performance limit for all antennas fitting within the design region using *e.g.*, MoM as a tool in current optimization. The latter is not understood as well, but may provide simple, yet valuable, results to antenna designers.

MoM [3], [26] is used to compute microstrip patch antenna bounds, where the surface current density on the design region  $\Omega$  is expanded in a set of basis functions  $\psi_m(\mathbf{r})$  as

$$\mathbf{J}(\mathbf{r}) = \sum_{m=1}^M I_m \psi_m(\mathbf{r}). \quad (1)$$

The expansion coefficients  $I_m$  are collected in  $\mathbf{I} \in \mathbb{C}^{M \times 1}$  and related to the excitation voltages  $\mathbf{V} \in \mathbb{C}^{M \times 1}$  as

$$\mathbf{Z}\mathbf{I} = \mathbf{V}. \quad (2)$$

The MoM impedance matrix,  $\mathbf{Z} \in \mathbb{C}^{M \times M}$ , is decomposed in its real and imaginary parts

$$\mathbf{Z} = \mathbf{R} + j\mathbf{X}, \quad (3)$$

defining the resistance  $\mathbf{R} \in \mathbb{R}^{M \times M}$  and reactance  $\mathbf{X} \in \mathbb{R}^{M \times M}$  matrices. This MoM impedance matrix describes the interaction between all basis functions on the patch. The interaction between the patch basis functions and the external environment (*e.g.*, dielectric and ground plane) is implicitly accounted for through the Green's functions derived using *e.g.*, Sommerfeld integrals [3].

### III. CALCULATING AND VALIDATING Q-FACTOR

The Q-factor of a single resonant antenna is inversely proportional to its fractional bandwidth [7]. However, unlike bandwidth, Q-factor can be computed at a single frequency. This is exploited here to approximate bandwidth, which is an important microstrip patch antenna design parameter. It should be noted that this formulation can be extended to multiband antennas, as long as there is one dominant resonance within each band.

The Q-factor of an antenna is related to its fractional bandwidth by [7]

$$B_{\Gamma_0} \approx \frac{2}{Q} \frac{\Gamma_0}{\sqrt{1 - \Gamma_0^2}}, \quad (4)$$

where  $\Gamma_0$  is the threshold for the reflection coefficient. An approximate Q-factor can be determined from inverting (4) as

$$Q_{\Gamma_0} = \frac{2}{B_{\Gamma_0}} \frac{\Gamma_0}{\sqrt{1 - \Gamma_0^2}}. \quad (5)$$

In this paper, the threshold is set to  $\Gamma_0 = -10$  dB to calculate approximate Q-factor values from simulated bandwidths.

The Q-factor (4) is linked to the quotient of stored energy and dissipated power ( $P_d$ ) as

$$Q = \frac{2\omega \max\{W_e, W_m\}}{P_d}, \quad (6)$$

where angular frequency is denoted by  $\omega = 2\pi f$ , electric stored energy by  $W_e$ , and magnetic stored energy by  $W_m$ .

Surface waves [19] result in some dissipated power in (6) not being radiated into free space even for an infinite lossless dielectric, PEC patch, and infinite PEC ground plane. When the substrate is thin, the surface wave that propagates in the dielectric layer only contains the first transverse magnetic surface-wave mode. This mode has no cutoff frequency and the first transverse electric surface-wave mode is launched when the free-space wavelength is,  $\lambda < 4h\sqrt{\epsilon_r - 1}$ , [3].

The dissipated power can then be divided into power radiated into free space ( $P_r$ ) and power lost in the surface wave ( $P_{sw}$ ) as  $P_d = P_r + P_{sw}$ . Then radiation efficiency due to losses in the surface wave is expressed as

$$\eta = \frac{P_r}{P_r + P_{sw}}. \quad (7)$$

Power lost in surface waves is undesirable even for a finite ground plane where they lead to diffraction on the edges [3]. Therefore rather than using the Q-factor in (6), a radiated Q-factor is determined as

$$Q_{\text{rad}} = \frac{Q}{\eta} = \frac{2\omega \max\{W_e, W_m\}}{P_r}. \quad (8)$$

Before the Q-factors (6) and (8) can be computed, expressions for dissipated power and stored energy are required. These quantities are determined from the current density  $\mathbf{J}(\mathbf{r})$  in the design region  $\Omega$  contained in the column matrix  $\mathbf{I}$ , *e.g.*, computed for a given geometry and excitation using (1). The dissipated power in (6) is evaluated from the MoM resistance matrix  $\mathbf{R}$  in (3) as [26]

$$P_d = \frac{1}{2} \mathbf{I}^H \mathbf{R} \mathbf{I}, \quad (9)$$

where the Hermitian transpose is denoted by superscript  $^H$ . The radiated power (7) is similarly determined from the radiation resistance matrix  $\mathbf{R}_r \in \mathbb{R}^{M \times M}$  as

$$P_r = \frac{1}{2} \mathbf{I}^H \mathbf{R}_r \mathbf{I}. \quad (10)$$

For a lossless dielectric, the radiation resistance matrix can be computed from the far field (Appendix A) or by splitting up the Sommerfeld integral as shown in [3].

Stored electromagnetic energies of microstrip patch antennas are interpreted here as the energy that does not radiate away through the dielectric (surface wave) or into free space (space wave). These energies are stored around the patch, for instance in the dielectric region near the patch (standing wave).

Stored energy of small antennas in free space have been accurately modeled [27], [28] and been generalized to patch antennas above an infinite ground plane [22] and heterogeneous temporally dispersive media [29]. The total stored

energy can be computed by differentiation of the reactance MoM matrix  $\mathbf{X}$  in (3) as proposed in [30] which together with the reactance define stored electric and magnetic energies [26], [28]

$$\begin{aligned} W_e &= \frac{1}{8} \mathbf{I}^H \left( \frac{\partial \mathbf{X}}{\partial \omega} - \frac{\mathbf{X}}{\omega} \right) \mathbf{I} \\ W_m &= \frac{1}{8} \mathbf{I}^H \left( \frac{\partial \mathbf{X}}{\partial \omega} + \frac{\mathbf{X}}{\omega} \right) \mathbf{I}. \end{aligned} \quad (11)$$

Here, stored energy expressions for small antennas in free space are extended to microstrip patch antennas, allowing for stored energy to be localized in the dielectric substrate near the patch design region  $\Omega$ . This procedure is based on (11) where closed form expressions for the angular frequency derivative,  $\frac{\partial \mathbf{X}}{\partial \omega}$ , are presented in Appendix A based on Sommerfeld integrals. From (11) it can be shown that both the electric and magnetic stored energy have a term associated with the vector and scalar potential Green's functions [3] and the angular frequency derivative thereof.

To validate the expressions for stored energies (11) for microstrip patch antennas, the Q-factor (6) is compared with Q-factors based on fractional bandwidth (5) and differentiation of the input impedance [28]. In this latter method the Q-factor for a single resonant antenna tuned with a series capacitor or inductor is given by [7]

$$Q_{Z'_{in}} = \frac{\sqrt{(\omega R'_{in})^2 + (\omega X'_{in} + |X_{in}|)^2}}{2R_{in}}, \quad (12)$$

where ' denotes angular frequency derivative and  $R_{in}$  and  $X_{in}$  are the real and imaginary parts of the input impedance, respectively.

A comparison between Q-factors (6) based on stored energies (11) (solid red curve) and differentiation of the input impedance (12) (dashed green curve) for H-shaped and rectangular patches are shown in Figure 2. The H-shaped and rectangular patches are fed with a delta gap excitation and microstrip line, respectively, with position indicated by the black rectangle. For further validation with (12), commercial software (FEKO) was used with a thin-wire feed over a small cut in the H-shaped patch instead of a delta gap feed (blue curve). Similarly, to validate the results for the rectangular patch the microstrip port excitation model in FEKO was used. For both patches the self resonances ( $X_{in} = 0$ ) were matched to  $R_{in}$ , in order to compute the fractional bandwidth. Then the fractional bandwidth was used to calculate Q-factor ( $Q_{\Gamma_0}$ ) from (5). These Q-factors are shown by black markers in Figure 2 and confirm the calculated Q-factor. This example indicates that Q-factor determined from the quadratic forms (11) is an accurate indicator of Q-factor and fractional bandwidth for microstrip patch antennas. Finally, it should be noted that when interpreting

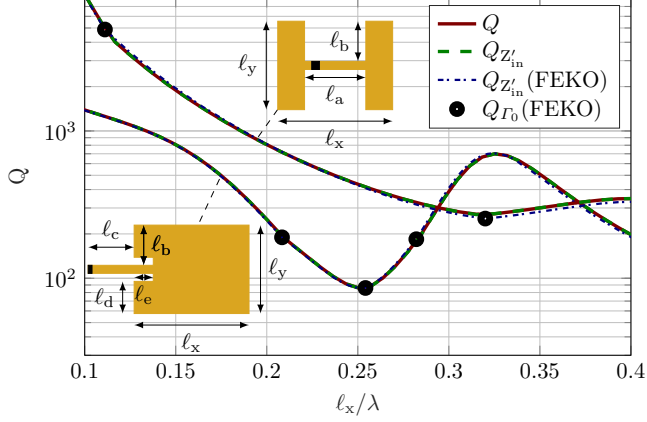


Figure 2: Validation of Q-factors computed using the stored energy in (11) ( $Q$ ), differentiation of the input impedance (12) ( $Q_{Z'_{in}}$ ) and fractional bandwidth (5) ( $Q_{\Gamma_0}$ ) for H-shaped and rectangular microstrip patch antennas on a dielectric slab with relative permittivity,  $\epsilon_r = 4$ , dimensions  $h = 0.05\ell_x$ ,  $\ell_y = 0.77\ell_x$ ,  $\ell_a = 7\ell_x/15$ ,  $\ell_b = 5\ell_y/11$ ,  $\ell_c = 2\ell_x/7$ ,  $\ell_d = 7\ell_y/22$ , and  $\ell_e = 5\ell_x/42$ . The Q-factors at self resonances are indicated with markers and are computed from the bandwidth ( $Q_{\Gamma_0}$ ).

computed Q-factor (6) and (12) in terms of bandwidth (5) for non-resonant structures ( $X_{in} \neq 0$ ) a series tuning capacitor or inductor is assumed.

#### IV. LOWER Q-FACTOR BOUNDS

From the expressions of Q-factor (6), dissipated power (9), and stored energy (11), an optimization problem to compute lower bounds on Q-factor can be written as

$$\begin{aligned} & \text{minimize} && \max \{W_e(\mathbf{I}), W_m(\mathbf{I})\} \\ & \text{subject to} && P_d(\mathbf{I}) = P_{in}. \end{aligned} \quad (13)$$

Both the objective (related to numerator of (6)) and the constraint are quadratic functions of the current ( $\mathbf{I}$ ), which is the optimization variable. Therefore, this is a quadratically constrained quadratic program (QCQP) which can be solved using its dual as a parametrized eigenvalue problem [31]. Note that the input power ( $P_{in}$ ) in (13) can be set to any arbitrary positive value. This does not change the bounds, but rather just scales the optimal currents. For the eigenvalue problem, a convex combination of  $W_e$  and  $W_m$  can be taken [15]. Then the eigenvalue problem to compute lower Q-factor bounds can be written as [13]

$$Q_{lb} = \frac{1}{2} \max_{\nu} \min \text{eig}(\nu \mathbf{X} + \mathbf{X}_{\omega}, \mathbf{R}), \quad (14)$$

with Lagrange parameter  $\nu \in [-1, 1]$  and  $\mathbf{X}_\omega = \omega \frac{\partial \mathbf{X}}{\partial \omega}$ . It should be noted that low-rank matrices  $\mathbf{R}$  can be exploited [32], [33] to reduce the computational cost of (14).

Once the optimization problem has been solved, it is possible to obtain currents that satisfy the bound from the eigenvectors. This implies equality in (14) and therefore no dual gap [34]. In some cases it may be necessary to test for degenerate eigenvalues to recover the currents as shown in [15]. This phenomenon is attributed to geometrical symmetries in the problem.

The Q-factor bounds from (14) can be determined once the MoM impedance matrix (3) and its angular frequency derivative in Appendix A have been computed. Q-factor bounds,

$$Q_{\text{lb}} = Q_{\text{lb}}(f, \Omega, h, \varepsilon_r), \quad (15)$$

obtained in this way are functions of several microstrip patch antenna parameters. Investigations of the bounds for any of these parameters can lead to useful antenna design insight. Illustrations in this paper focus on two cases; firstly how the bounds depend on the frequency  $f$  for a fixed design region and dielectric slab, and secondly how the bounds depend on the design region  $\Omega$  for a fixed dielectric slab and frequency.

To demonstrate the bounds for the case with a fixed geometry, a design region  $\Omega$  with  $\ell_y = 0.77\ell_x$  and dielectric thickness  $h = 0.05\ell_x$ , see Figure 1, is considered together with a sweep of frequency or equivalently free-space wavelength ( $\lambda$ ). For substrate relative permittivities  $\varepsilon_r \in \{1, 2, 4\}$ , lower Q-factor bound,  $Q_{\text{lb}}$ , are shown for electrical sizes  $\ell_x/\lambda$  by solid lines in Figure 3. It should be further emphasized that although the bounds are computed for a rectangular patch region, they imply that any patch geometry fitting within the design region,  $\Omega$  has Q-factor at or above the bound.

The Chu bound [10], [35],  $Q \geq Q_{\text{Chu}} = 1/(ka)^3 + 1/(ka)$ , for any antenna enclosed in a sphere of radius  $a$  circumscribing the patch and its mirror image, is also shown in Figure 3. The Chu limit is clearly not tight for microstrip patch antennas and orders of magnitude off the bounds presented here. This is due to the use of a circumscribing sphere, where the radius of the volumetric design region is  $a \approx 0.632\ell_x$  instead of the actual planar design region.

The bounds are compared with Q-factors from (12) of antenna designs (a-c) in Figure 1 with input impedance simulated in FEKO. These patches with probe feed, having placement indicated by markers on their geometry, are shown in Figure 3. The two half-wavelength resonant patches (a in Figure 1) are matched to  $50\Omega$ . The Q-factors calculated using (12) are shown to be approximately on the bounds for all three relative permittivities. Two other matched antenna designs (slot loaded (b) and H-shaped (c)) are shown to also be approximately on the bounds. These examples demonstrate that the computed bounds are tight, in the

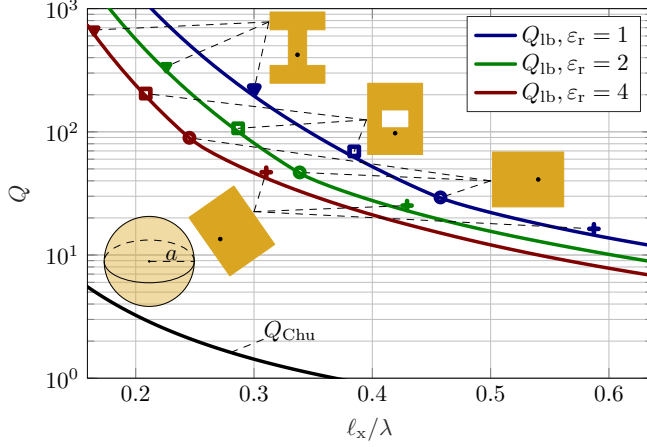


Figure 3: Demonstration of the tightness of lower Q-factor bounds for a rectangular design region  $\Omega$  with aspect ratio  $\ell_y = 0.77\ell_x$ , substrate thickness  $h = 0.05\ell_x$  and relative permittivity  $\varepsilon_r \in \{1, 2, 4\}$  computed using (14). FEKO simulation results for self-resonant antenna types (a-c in Figure 1) with Q-factors from (12) are indicated with markers. The H-shaped patch (c) has additional dimensions,  $\ell_a = 0.5\ell_x$  and  $\ell_b = \ell_y/3$ , see Figure 2. To place the new bounds into perspective, the Chu limit ( $Q_{\text{Chu}}$ ) [10] is included.

sense that it is possible to design antennas with Q-factors close to the bound. The examples also show that the resonance frequencies scale approximately with the wavelength in the dielectric  $\lambda_\varepsilon = \lambda/\sqrt{\varepsilon_r}$ , as expected.

The optimal currents obtained from (14) given a rectangular design region are generally associated with a polarization along the longer dimension of the patch for radiation in the normal direction, therefore in Figure 3,  $\hat{x}$ -polarized as  $\ell_x > \ell_y$ . To enforce polarization along the shorter dimension of the patch, the optimization problem (13) is reformulated by adding an affine constraint to ensure no undesired polarization as

$$\begin{aligned} & \text{minimize} && \max \{W_e(\mathbf{I}), W_m(\mathbf{I})\} \\ & \text{subject to} && P_d(\mathbf{I}) = P_{\text{in}} \\ & && \mathbf{F}_o \mathbf{I} = 0, \end{aligned} \quad (16)$$

where  $\mathbf{F}_o$  is the far-field vector (defined in Appendix A) for the undesired polarization. When an  $\hat{x}$ -polarization bound is desired but  $\ell_y > \ell_x$ , then  $\mathbf{F}_o$ , defined here for radiation normal to the patch into free space, should be for  $\hat{y}$ -polarization in (16). Optimization problem (16) can be reduced to the form (13) by eliminating the linear equality constraint [36], similar to (14), solved as an

eigenvalue problem. It should be noted that by maximizing partial gain over Q-factor, dependence on polarization can also be investigated [22].

The optimization problems in (13) and (16) can be reformulated to minimize the radiated Q-factor ( $Q_{\text{rad}}$ ) in (8) by replacing  $P_d$  with  $P_r$ . This can potentially yield different optimal currents.

## V. BOUNDS FROM SELF-RESONANT PATCHES

The formulation to obtain lower Q-factor bounds presented in Section IV requires a MoM implementation as *e.g.*, presented in Section II. However, a simpler approximate formulation to obtain lower Q-factor bounds may be desired. Therefore, this section introduces a simple approximate method for obtaining lower Q-factor bounds over a range of frequencies (15), requiring only simulations of half-wavelength resonant patch antennas.

Patch antenna resonances are associated with their dielectric wavelengths, as shown in Figure 3. Therefore, it is worth comparing bounds at the same dielectric wavelength  $\lambda_\epsilon$  as shown in Figure 4. When comparing Figure 3 and Figure 4, it is observed that the order of the curves are swapped. This is simply due to the bounds being represented with respect to dielectric wavelength in Figure 4 as opposed to the free-space wavelength in Figure 3. Other than the addition of the bounds with relative permittivity  $\epsilon_r = 10$  the data is the same. A reason for using the dielectric wavelength is that resonances of half-wavelength patches are approximately at  $\ell_x/\lambda_\epsilon \approx 0.5$ .

The log-log plot in Figure 4 has straight lines, and the bounds scaling can be read of as approximately  $(\lambda_\epsilon/\ell_x)^5$  (doubling size reduces  $Q$  bounds by a factor 32) up to the half-wavelength resonances. This scaling is also derived in Appendix B through a low-frequency expansion assuming no total charge on the patch, given  $\epsilon_r = 1$ , and can be partially attributed to the ground plane acting as a short for small  $h/\lambda$ . It should be noted that at low-frequencies given a total charge on the patch, radiation from the charge difference between patch and ground plane can result in  $(\lambda_\epsilon/\ell_x)^3$  Q-factor scaling, however this form of monopole radiation is not desired for patch antennas.

To use the  $(\lambda_\epsilon/\ell_x)^5$  scaling to approximate bounds, a valid reference Q-factor is required. For this, simulated half-wavelength resonant patch antennas' Q-factors,  $Q_{\text{hw}}$ , computed using (5) or (12), are chosen. These are reasonable reference Q-factors, as these antennas perform close to the bounds, as shown in Figure 3. The simple scaling rule that follows from these simulations of half-wavelength resonant patch antennas with frequency  $f_{\text{hw}}$  and dielectric wavelength  $\lambda_{\epsilon,\text{hw}}$ , is given by

$$\tilde{Q}_{\text{lb}}(f) = \frac{Q_{\text{hw}} f_{\text{hw}}^5}{f^5} = \frac{Q_{\text{hw}} \lambda_\epsilon^5}{\lambda_{\epsilon,\text{hw}}^5}. \quad (17)$$

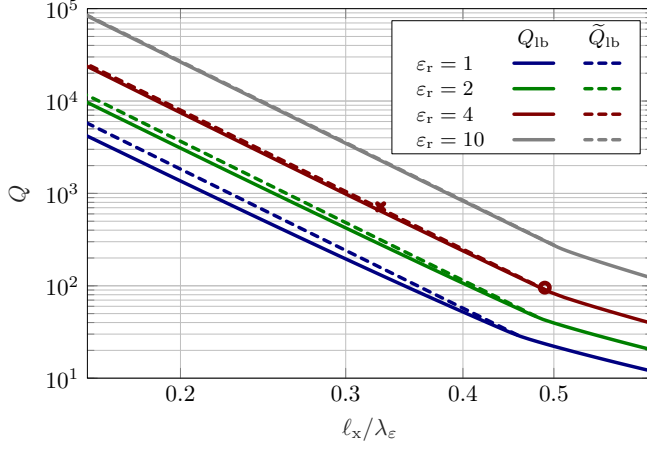


Figure 4: Lower Q-factor bounds for rectangular design regions  $\Omega$  with dimensions  $\ell_y = 0.77\ell_x$  and dielectric thickness  $h = 0.05\ell_x$  plotted versus  $\ell_x/\lambda_\epsilon$ . Dashed lines show how (17) approximates the lower Q-factor bounds from simulations of half-wavelength resonant patches. The markers show the Q-factor obtained from simulating a half-wavelength resonant patch antenna as well as the predicted Q-factor from (17) interpreted as for the same geometry at a desired design frequency.

This scaling rule is presented in Figure 4 (dashed lines) for bounds varying in frequency for a fixed design region and dielectric slab, *i.e.*, for a fixed  $\epsilon$ ,  $h$ ,  $\ell_x$  and  $\ell_y$ . The results show that by only simulating one half-wavelength patch, a good approximation of Q-factor bounds over a range of frequencies with chosen geometric constraints and permittivity are obtained. This scaling is observed to be more accurate for higher relative permittivity. It should be noted that this scaling can also be added as an extension of the cavity model predicted half-wavelength Q-factors [1], this does not require a full-wave solver but is less accurate.

For design purposes, it is convenient to know approximate bounds on Q-factor to obtain a benchmark before beginning the design process. To this aim, consider a design region  $\Omega$  with fixed dielectric slab and working frequency of the antenna  $f$ . For the design region the maximum length is  $\ell_x$  and the maximum width is  $\ell_y$ . The relative permittivity and height of the dielectric slab are  $\epsilon_r$  and  $h$ , respectively. An approximation of lower Q-factor bounds for the antenna under design consideration can be obtained using the scaling (17) through the following procedure:

- 1) Determine the half-wavelength resonance frequency,  $f_{\text{hw}}$ , for the considered

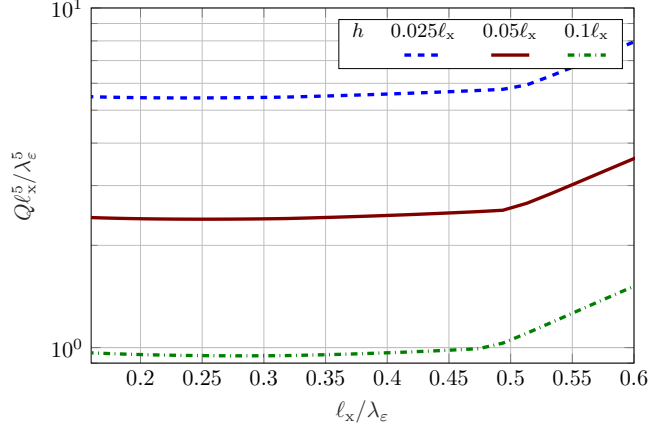


Figure 5: Lower Q-factor bounds for rectangular patch region with dimensions  $\ell_y = 0.77\ell_x$ , relative permittivity  $\varepsilon_r = 4$  and varying height. The axis is scaled to show the  $(\ell_x/\lambda_\varepsilon)^5$  scaling.

- dielectric slab and design region
- 2) Obtain the Q-factor  $Q_{\text{hw}}$  of the half-wavelength patch using either (5) or (12)
- 3) Obtain  $\tilde{Q}_{\text{lb}}(f)$  from  $Q_{\text{hw}}$  using (17)

An example of using the scaling rule (17) is to compute an approximation of lower Q-factor bounds at 2.45 GHz for relative permittivity  $\varepsilon_r = 4$ , dimensions  $\ell_x = 20$  mm,  $\ell_y = 15.4$  mm and  $h = 1$  mm. Then step 1) the half-wavelength resonance frequency is determined as approximately 3.665 GHz. For the second step 2) the Q-factor is computed as 95.5 at the half-wavelength resonance. Then finally 3) using the scaling  $\tilde{Q}_{\text{lb}}(f) \approx 95.5(3.665/2.45)^5 \approx 715$ . This corresponds to a  $-10$  dB bandwidth of approximately 2.3 MHz. The results from these steps are shown by markers in Figure 4.

The scaling of (17) is further demonstrated on results presented in Figure 4, by factoring out the  $\lambda_\varepsilon^5/\ell_x^5$  scaling, as shown in Figure 5. Additional dielectric thicknesses are also considered and shown to have similar scaling along with the expected result that increased dielectric thickness results in a lower Q-factor [1]. Lastly, it should be noted that the small difference between the predicted scaling and bounds in Figure 4 depends on  $h$  and  $\lambda$ . By reducing  $h$  or increasing  $\lambda$  the proposed scaling (17) becomes a more accurate approximation. This means that scaling comes closer to the low-frequency expansion of Appendix B, and also that the scaling contribution of the surface wave is reduced.

## VI. PRACTICAL EXAMPLES

In this section, practical applications of the lower Q-factor bounds compared with simulated antenna designs are presented. Subsection VI-A illustrates how the Q-factor depends on the patch width for antennas linearly polarized along their length. Subsection VI-B examines how the size of the design region impacts Q-factor bounds for a given frequency and substrate. Subsection VI-C shows how the bounds can be applied to dual resonant patch antennas. Finally, Subsection VI-D shows the effect when bounds are determined on radiated Q-factor (8) instead of on Q-factor (6).

### A. Design region width

Improvement in bandwidth can be achieved by altering the width of half-wavelength patch antennas [1]. This subsection investigates this improvement for arbitrary shaped antennas, designed within a rectangular design region  $\Omega$  (see Figure 1). In Figure 6, the patch width ( $\ell_y$ ) effect on the bounds ( $Q_{lb,x}$ ) for polarization along the length ( $\ell_x$ ) enforced by (16) is shown. However, the slopes of the bounds in Figure 6 are relatively unaffected by the change in width. This implies that the scaling rule of (17) can be generalized to other length-to-width ratios than shown in Figure 4. The bounds are observed to scale roughly as  $\ell_x/\ell_y$  (doubling  $\ell_y$  reduces  $Q$  bounds by a factor 2) as shown in Figure 7 at selected  $\ell_x/\lambda_\epsilon$ . Further, when the width is greater than the length, the lower Q-factor bounds can be significantly greater than when polarization is disregarded solving (13), especially at lower frequencies. This is due to the dielectric wavelength of the patch being linked to the polarization direction ( $\ell_x$ ) and therefore being the most significant patch dimension regarding Q-factor scaling, especially before the half-wavelength resonance (as shown in Subsection VI-C). Finally, the bounds of Figure 1 are shown to have both the H-shaped and half-wavelength patch antennas near the Q-factor bounds for all presented patch dimensions.

### B. Patch design for a given substrate and frequency

A classical problem is to design patch antennas for a given frequency and dielectric substrate. In this subsection, a design scenario is used to investigate how the design region ( $\Omega$ ) affects the Q-factor bounds for a given dielectric substrate and frequency. The chosen substrate has thickness,  $h = 1.57$  mm, and relative permittivity,  $\epsilon_r = 2.33$ , as for RTDuroid 5870 by Rogers Corporation, but it is considered lossless. Then, for a frequency of  $f = 2.45$  GHz, the length and width of the patch design region are varied. The lower Q-factor bounds, constrained to  $\hat{x}$ -polarization in the normal direction by solving optimization problem (16), are shown in Figure 8. This contour plot for a range of design

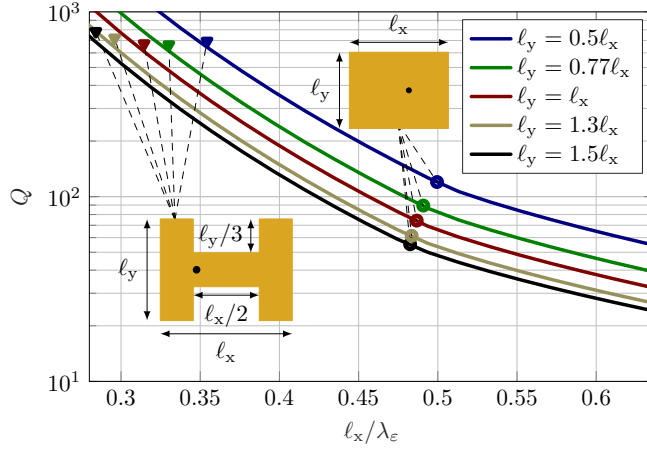


Figure 6: Effect of width  $\ell_y$  on the lower Q-factor bounds for polarization along  $\ell_x$  enforced through (16), relative permittivity  $\varepsilon_r = 4$  and thickness  $h = 0.05\ell_x$ . The bounds are compared to the performances of H-shaped and half-wavelength resonant patch antennas using (5).

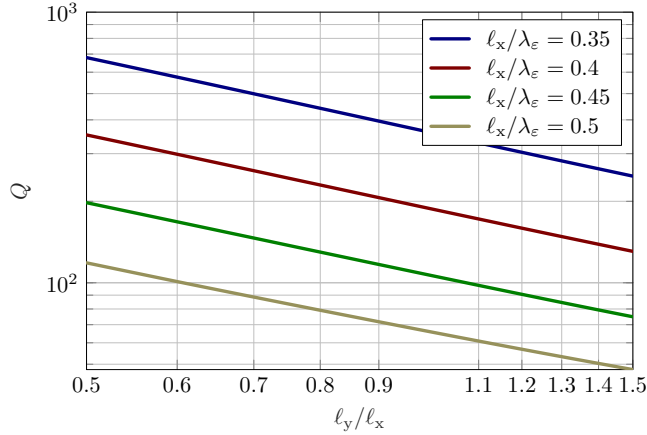


Figure 7: Effect of width ( $\ell_y$ ) on the lower Q-factor bounds,  $Q_{lb,x}$ , for different electrical lengths  $\ell_x/\lambda_\varepsilon$  with polarization along  $\ell_x$  enforced through (16), relative permittivity  $\varepsilon_r = 4$  and thickness  $h = 0.05\ell_x$ .

TABLE I: NUMERICAL Q-FACTORS OF PATCHES SHOWN IN FIGURE 8

Patch type	$\ell_x$ / mm	$\ell_y$ / mm	$Q_{lb,x}$	$Q_{Z'_{in}}$
Half-wavelength	38.5	50	45	45
Half-wavelength	38.9	30	66	67
Half-wavelength	39.4	20	90	91
Slot loaded	35.2	28	90	94
Slot loaded	36.7	18	118	121
H-shaped	25.9	20	274	297

region dimensions provides lower Q-factor bounds. Given a design region, the bounds indicate whether it is possible to obtain a required Q-factor. For a desired Q-factor, the bounds also provide a range of possible design regions that can aid patch miniaturization.

The regular spacing of the contours in log scale show that for this scenario a relatively simple bounds scaling can be derived. The contour lines are all spaced by  $10^{0.2}$ , therefore, the first line less than  $Q_{lb,x} = 1000$  is  $Q_{lb,x} \approx 631$ . Going between these two lines, it can clearly be read off that a change in  $\ell_x$  (polarization dimension) results in greater bounds scaling compared with an equal change in  $\ell_y$  (width dimension), as shown in Subsection VI-A. Thus, doubling  $\ell_x$  results in moving across 4 contour lines while doubling  $\ell_y$  results in only moving across 2 contour lines.

To further demonstrate the relevance of the bounds, FEKO is used to simulate patch antennas. This is first done for three half-wavelength patches by using a probe feed and then obtaining Q-factors from (12). These results are shown to be near the bounds and are indicated by their geometry in the contour plot. Further, slot loaded patches (b) and an H-shaped patch (c), are simulated. All patches shown in Figure 8 are within a margin of 10% from the lower Q-factor bounds, see Table I.

### C. Dual resonance

Some patch antennas are designed for dual resonance [19]. In the first example, Q-factors for dual resonant antennas are compared with the lower Q-factor bounds allowing for different polarization for the two resonances. In the second example, a design with the same polarization for both resonances is considered.

For the first example, Figure 9 shows a comparison between  $\hat{x}$  and  $\hat{y}$ -polarized lower Q-factor bounds (16) for a patch with dimensions  $\ell_y = 0.77\ell_x$ ,  $h = 0.05\ell_x$  and relative permittivity  $\varepsilon_r = 4$ . Firstly, it shows that at lower frequencies, a significant reduction in Q-factor can be achieved by having polarization along the longer dimension of the design region. Further, it indicates that at higher frequencies (around the half-wavelength resonance of the shorter ( $y$ ) dimension) there is little difference between the bounds. This result also shows that for

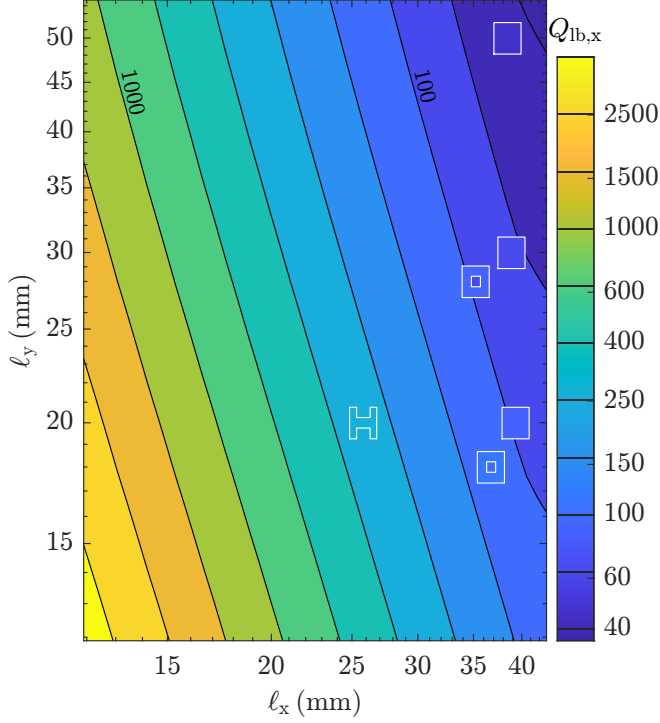


Figure 8: Lower Q-factor bounds,  $Q_{lb,x}$ , for relative permittivity  $\epsilon_r = 2.33$ , frequency  $f = 2.45$  GHz, dielectric thickness  $h = 1.57$  mm and a rectangular design region  $\Omega$  with side lengths  $\ell_x$  and  $\ell_y$  for  $\hat{x}$ -polarized antennas in the normal direction. The shown antenna geometries have interior colors corresponding to their Q-factors computed using (12), see Table I.

dual resonant patch antennas, two orthogonal modes tight to the bounds can be obtained. This patch is shown with feed placement indicated with a black dot. Further, a reduction in Q-factor is not possible by using circular polarization [37], [38] with these design parameters since  $\hat{x}$ -polarization is essentially on the bounds, calculated using (13), which allows for arbitrary polarization.

For the second example, a dual resonant antenna with the same polarization for both bands can be obtained from the U-slot patch (d) in Figure 1. In this case, efficiently utilizing the patch design region for both resonances is challenging. This is because a larger portion of the design region is effectively used for the first resonance than for the second resonance. The results in Figure 10 show this for a chosen U-slot patch (with dimensions  $h = 4.5$  mm,  $\ell_x = 21.5$  mm and  $\ell_y = 26.5$  mm). From simulations Q-factor is computed using (5), the resonances are located at approximately 3.64 GHz ( $\ell_x/\lambda_\epsilon \approx 0.39$ ) and 5.23 GHz ( $\ell_x/\lambda_\epsilon \approx 0.56$ ).

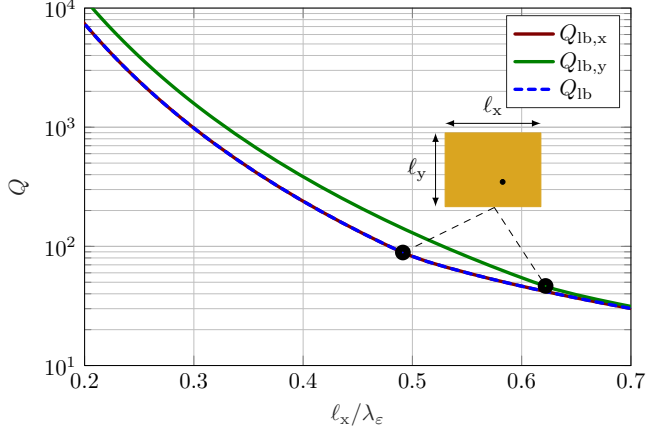


Figure 9: Dual polarized antenna design with  $\hat{x}$  and  $\hat{y}$ -polarization, compared with lower Q-factor bounds for a design region with dimensions  $\ell_y = 0.77\ell_x$ ,  $h = 0.05\ell_x$  and relative permittivity  $\varepsilon_r = 4$  obtained from (13) and (16). The dual resonant antenna geometry is shown with feed location and two simulated resonance Q-factors obtained using (12) are indicated by markers.

The first resonance is near the bounds, while the second is significantly off. This may be seen as a fair trade-off, as it results in a similar fractional bandwidth of approximately 0.05 for both resonances. This fractional bandwidth is similar to what is reported in [39] from CST simulations with a finite ground plane that is double the size of the design region.

#### D. Surface-wave losses

To investigate the contribution of surface-wave losses on Q-factor bounds (13), the latter are computed with ( $Q_{lb}$ ) and without surface-wave losses ( $Q_{lb}^{rad}$ ). For both  $Q_{lb}$  and  $Q_{lb}^{rad}$  the optimal currents are then used to compute the radiation efficiency for relative permittivities  $\varepsilon_r \in \{2, 4\}$  as shown in Figure 11. Observe that in the presented range of  $\ell_x/\lambda_\varepsilon$  for both relative permittivities there is no significant noticeable difference in radiation efficiency between  $Q_{lb}$  and  $Q_{rad}$ . Additionally, the quotient  $Q_{lb}/Q_{lb}^{rad}$  (see, (8)), indicating similar radiation efficiency, correctly suggests that the optimal currents effectively produce the same Q-factor. At the half-wavelength resonance FEKO simulations are used to compute the radiation efficiency as indicated with markers in Figure 11. The FEKO simulations' radiation efficiency was determined by integrating over the far-field above the patch (radiated power) and comparing this with the input power. The small difference between FEKO and the bounds come from a combination of factors *e.g.*, a different feed model. Furthermore, it can clearly

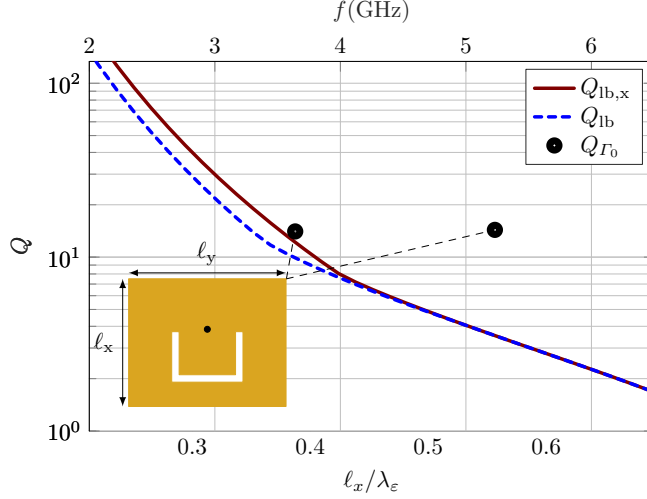


Figure 10: Lower Q-factor bounds for a design region with dimensions  $\ell_x = 21.5$  mm and  $\ell_y = 26.5$  mm compared with a dual resonant U-slot patch antenna design adapted from [39], where the relative permittivity is  $\epsilon_r = 2.2$  and substrate thickness is  $h = 4.5$  mm.

be seen that a greater relative permittivity and  $\ell_x/\lambda_\epsilon$  results in greater surface-wave losses when computing Q-factor bounds.

For a horizontal electric (Hertzian) dipole (HED) on the patch region, given a thin substrate, an approximate ratio between surface-wave power and radiated power is [40]

$$\frac{P_{\text{sw}}}{P_r} = \frac{3\pi^2}{2} \frac{(\epsilon_r - 1)^3 h/\lambda}{\epsilon_r^2 (\epsilon_r - 1) + \frac{2}{5}\epsilon_r}. \quad (18)$$

From this expression, radiation efficiency can, in a lossless case, be approximated as  $\eta_{\text{HED}} = 1/(1 + P_{\text{sw}}/P_r)$ . This has been shown to be accurate up to  $h \leq 0.05\lambda$  [40].

In Figure 11, the radiation efficiency obtained for an HED is shown with two black lines. These lines suggest that it can be sufficient to use (18) in determining radiation efficiency once bounds have been computed with (13).

## VII. CONCLUSION

In this paper, a formulation to compute lower Q-factor bounds for microstrip patch antennas is presented. The results are numerically validated against expressions available in literature for computing Q-factor from fractional bandwidth and input impedance. Current optimization is used to compute the lower Q-factor bounds. These bounds are shown to be tight for classic patch antenna designs.

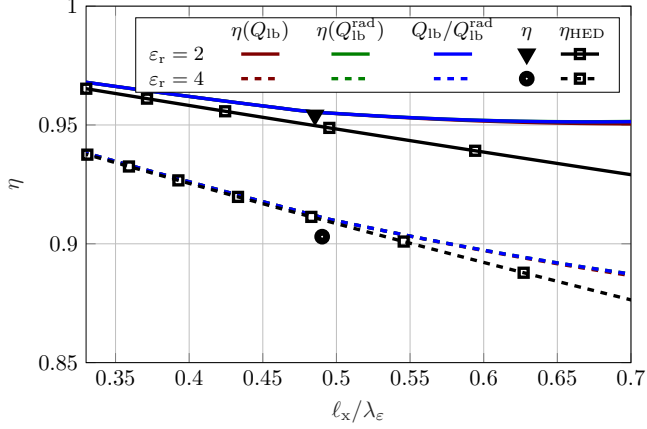


Figure 11: Radiation efficiency due to surface-wave losses of lower Q-factor bounds currents for the lossless case given a patch with dimensions  $\ell_y = 0.77\ell_x$  and dielectric thickness  $h = 0.05\ell_x$ . Two relative permittivities  $\varepsilon_r \in \{2, 4\}$  are used and for half-wavelength resonant patches radiation efficiency calculated with FEKO are shown with markers. The approximate radiation efficiency for a HED (18) is also shown for both relative permittivities.

This further emphasizes the versatility of current optimization as a method of determining lower Q-factor bounds, previously generally only applied to antennas in free space. Further, the microstrip patch antennas under investigation serve as a canonical case for introducing the method.

It is shown that lower Q-factor bounds can be approximated by a simple method that only requires the simulation of half-wavelength resonant patch antennas. The low-frequency lower Q-factor bounds scale differently from those of antennas in free space, due to the ground plane. Further, this bound is orders of magnitude tighter than the Chu bound. Moreover, it shows that circular polarization cannot enhance bandwidth for the patch antennas considered here.

Some practical applications of the bounds are also considered, such as how the design frequency and design region impact the bounds for a given dielectric substrate. Obtained Q-factor for dual resonant antennas are also compared to the bounds for both orthogonal, and parallel polarization, of the two resonances. The bounds are computed with and without surface-wave losses, showing that for electrically thin substrates, the surface-wave contribution to the bounds is relatively small and can be accurately approximated by a closed form expression.

Among potential extensions of the proposed method are the addition of shorting pins, stacked patches and considering other design region shapes *e.g.*, circular. A further extension is using two resonances to widen the bandwidth.

APPENDIX A  
MOM IMPEDANCE ANGULAR FREQUENCY DERIVATIVE

The MoM impedance matrix in (3), assuming no ohmic losses, can be expressed as

$$\mathbf{Z} = j\omega\mu_0\mathbf{L} + \frac{\mathbf{C}_i}{j\omega\varepsilon_0}, \quad (19)$$

where  $\mathbf{L}$  and  $\mathbf{C}_i$  are broadly linked to the inductance and inverse of the capacitance, respectively. The permeability of free space is denoted  $\mu_0$ , the permittivity of free space is denoted  $\varepsilon_0$ , and the speed of light in free space is given by  $c_0 = 1/\sqrt{\varepsilon_0\mu_0}$ . Matrix  $\mathbf{L}$  has elements

$$L_{mn} = \int_{\Omega} \int_{\Omega} \boldsymbol{\psi}_m(\mathbf{r}_1) \cdot \mathbf{G}_A \cdot \boldsymbol{\psi}_n(\mathbf{r}_2) dS_1 dS_2, \quad (20)$$

and matrix  $\mathbf{C}_i$  has elements

$$C_{imn} = \int_{\Omega} \int_{\Omega} \nabla_1 \cdot \boldsymbol{\psi}_m(\mathbf{r}_1) \nabla_2 \cdot \boldsymbol{\psi}_n(\mathbf{r}_2) G_V dS_1 dS_2, \quad (21)$$

where the basis functions are denoted  $\boldsymbol{\psi}_m$  and  $\boldsymbol{\psi}_n$ . Since all basis functions are assumed to be on the patch region, the distances between basis functions are equal to their radial distances, given by  $\rho_{12} = |\mathbf{r}_1 - \mathbf{r}_2|$ . The vector Green dyadic,  $\mathbf{G}_A = G_A(\hat{\mathbf{x}}\hat{\mathbf{x}} + \hat{\mathbf{y}}\hat{\mathbf{y}})$  can be calculated from the scalar,  $G_A$ , since no  $z$ -directed basis functions are assumed. Along with the scalar Green's function,  $G_V$ , are expressed in radial coordinates as

$$\begin{aligned} G_A(\rho_{12}) &= \frac{1}{4\pi} S_0 \left( \frac{1}{D_{TE}} \right) \\ G_V(\rho_{12}) &= \frac{1}{4\pi} S_0 \left( \frac{N}{D_{TE} D_{TM}} \right), \end{aligned} \quad (22)$$

where the Sommerfeld integral,  $S_0$  is [3]

$$S_0(g) = 2 \int_0^{\infty} J_0(k_{\rho}\rho_{12}) k_{\rho} g(k_{\rho}, \omega) dk_{\rho}, \quad (23)$$

where  $J_0$  is the Bessel function of order 0 and  $k_{\rho}$  is the radial spectral coordinate. Further,  $D_{TE}$ ,  $D_{TM}$ , and  $N$  are defined as [3]

$$\begin{aligned} D_{TE} &= u_1 + u_2 \coth u_2 h \\ D_{TM} &= \varepsilon_r u_1 + u_2 \tanh u_2 h \\ N &= u_1 + u_2 \tanh u_2 h, \end{aligned} \quad (24)$$

with

$$u_1 = \sqrt{k_{\rho}^2 - \omega^2 c_0^{-2}} \quad \text{and} \quad u_2 = \sqrt{k_{\rho}^2 - \omega^2 \varepsilon_r c_0^{-2}}. \quad (25)$$

The following derivation is used to compute stored energies (11). Firstly, the angular frequency derivative of the MoM impedance matrix is computed as

$$\frac{\partial \mathbf{Z}}{\partial \omega} = j\mu_0 \mathbf{L} + j\mathbf{C}_i \frac{1}{\omega^2 \varepsilon_0} + j\omega\mu_0 \frac{\partial \mathbf{L}}{\partial \omega} + \frac{1}{j\omega\varepsilon_0} \frac{\partial \mathbf{C}_i}{\partial \omega}, \quad (26)$$

and the imaginary part can easily be separated for computations of (11). The angular frequency derivative of  $\mathbf{L}$  is

$$\frac{\partial L_{mn}}{\partial \omega} = \int_{\Omega} \int_{\Omega} \psi_m(\mathbf{r}_1) \cdot \psi_n(\mathbf{r}_2) \frac{\partial G_A}{\partial \omega} dS_1 dS_2, \quad (27)$$

and the angular frequency derivative of  $\mathbf{C}_i$  is

$$\frac{\partial C_{imn}}{\partial \omega} = \int_{\Omega} \int_{\Omega} \nabla_1 \cdot \psi_m(\mathbf{r}_1) \nabla_2 \cdot \psi_n(\mathbf{r}_2) \frac{\partial G_V}{\partial \omega} dS_1 dS_2. \quad (28)$$

To calculate angular frequency derivatives of the vector and scalar Green's functions in (22), differentiation is moved inside the integral in the Sommerfeld integral under conditions given by Lebesgue's dominated convergence theorem [41]. The angular frequency derivative of the vector Green's function can then be written as

$$\frac{\partial}{\partial \omega} G_A(\rho_{12}) = \frac{1}{4\pi} S_0 \left( \frac{\partial}{\partial \omega} \frac{1}{D_{TE}} \right). \quad (29)$$

The final expressions follow from basic differentiation rules and explicit differentiation of terms in (22). The angular frequency derivative of  $D_{TE}^{-1}$  is given by

$$\frac{\partial}{\partial \omega} \frac{1}{D_{TE}} = -\frac{\frac{\partial}{\partial \omega} D_{TE}}{D_{TE}^2}, \quad (30)$$

where

$$\frac{\partial D_{TE}}{\partial \omega} = \frac{\omega}{c_0^2} \left( \varepsilon_r h \operatorname{csch}^2 hu_2 - \frac{1}{u_1} - \frac{\varepsilon_r \coth hu_2}{u_2} \right). \quad (31)$$

The angular frequency derivative of the scalar Green's function (22) is expressed as

$$\frac{\partial}{\partial \omega} G_V(\rho_{12}) = \frac{1}{4\pi} S_0 \left( \frac{\partial}{\partial \omega} \frac{N}{D_{TE} D_{TM}} \right), \quad (32)$$

which is further computed using

$$\frac{\partial}{\partial \omega} \frac{N}{D_{TE} D_{TM}} = \frac{D_{TE} D_{TM} \left( \frac{\partial N}{\partial \omega} \right) - N \left( \frac{\partial D_{TE} D_{TM}}{\partial \omega} \right)}{(D_{TE} D_{TM})^2}, \quad (33)$$

where

$$\frac{\partial}{\partial \omega} D_{TE} D_{TM} = D_{TM} \frac{\partial}{\partial \omega} D_{TE} + D_{TE} \frac{\partial}{\partial \omega} D_{TM}, \quad (34)$$

with

$$\frac{\partial D_{TM}}{\partial \omega} = \frac{\omega \varepsilon_r}{c_0^2} \left( -\frac{1}{u_1} - \frac{\tanh hu_2}{u_2} - h \operatorname{sech}^2 hu_2 \right), \quad (35)$$

and

$$\frac{\partial N}{\partial \omega} = \frac{\omega}{c_0^2} \left( -\frac{1}{u_1} - \frac{\varepsilon_r \tanh hu_2}{u_2} - \varepsilon_r h \operatorname{sech}^2 hu_2 \right). \quad (36)$$

The Sommerfeld integrals of (29) and (32) can be solved in the spectral-domain by going out into the complex plane to avoid the singularity and discontinuity at  $u_1 = 0$ . For (32) the singularity of the first transverse magnetic surface wave mode at  $D_{\text{TM}} = 0$  should also be avoided. It is assumed there is only one surface wave mode. Note, there is no singularity or discontinuity at  $u_2 = 0$  [3]. To integrate the tail, partition-extrapolation using the Mosig–Michalski algorithm [42] can be used, except when  $\rho_{12} = 0$ , where the integrals are non-oscillatory as a result of  $J_0(0) = 1$  in (24). These integrals are also finite and relatively easy to solve.

From Sommerfeld integrals an asymptotic expression for the radiated far field can be derived [3]. Given radiation in the  $z$ -direction from an HED at the origin, the far-field can be rewritten assuming for instance an  $x$ -directed current producing an  $\hat{x}$ -polarized far-field at  $x = 0$ ,  $y = 0$  and  $z \rightarrow \infty$ .

Using the far-field relation [11],  $\mathbf{E}_{\hat{e}}(\hat{\mathbf{r}}) = e^{-jk r} \mathbf{F}_{\hat{e}}(\hat{\mathbf{r}})/r$  as  $r \rightarrow \infty$ , and the current density expanded in local basis functions as (1), the far-field vector can then be expressed as

$$\mathbf{F}_{\hat{e}}(\hat{\mathbf{z}}) \approx \mathbf{F}\mathbf{I} = \sum_{m=1}^M \frac{-j\omega\mu_0 I_m}{2\pi(1 - j\sqrt{\varepsilon_r} \cot(kh\sqrt{\varepsilon_r}))} \int_{\Omega} \hat{\mathbf{e}}^* \cdot \boldsymbol{\psi}_m(\mathbf{r}) e^{jk\hat{\mathbf{z}} \cdot \mathbf{r}} d\mathbf{S}, \quad (37)$$

where  $\hat{\mathbf{e}}$  is the unit polarization vector and superscript  $*$  denotes the complex conjugate.

## APPENDIX B

### LOW-FREQUENCY EXPANSION

Mirror currents are used to determine the low-frequency expansion for horizontal current densities in a region  $\Omega$  at height  $h$  above an infinite PEC ground plane. The electric far-field  $\mathbf{F}$  in a direction  $\hat{\mathbf{r}}$  from a current density  $\mathbf{J}$  in free space can be expressed as

$$\mathbf{F}(\hat{\mathbf{r}}) = \frac{-jk\eta_0}{4\pi} \left( \hat{\mathbf{r}} \times \int_{\mathbb{R}^3} e^{jk\hat{\mathbf{r}} \cdot \mathbf{r}_1} \mathbf{J}(\mathbf{r}_1) dV_1 \right) \times \hat{\mathbf{r}}, \quad (38)$$

which for the patch geometry with surface currents and surface mirror currents reduces to

$$\begin{aligned} \int_{\mathbb{R}^3} e^{jk\hat{\mathbf{r}} \cdot \mathbf{r}_1} \mathbf{J}(\mathbf{r}_1) dV_1 &= \int_{\Omega} e^{jk\hat{\mathbf{r}} \cdot \mathbf{r}_1} \mathbf{J}_s(\mathbf{r}_1) - e^{jk\hat{\mathbf{r}} \cdot (\mathbf{r}_1 - 2\hat{\mathbf{z}}\mathbf{r}_1 \cdot \hat{\mathbf{z}})} \mathbf{J}_s(\mathbf{r}_1) dS_1 \\ &= \int_{\Omega} \left( e^{jk\hat{\mathbf{r}} \cdot \mathbf{r}_1} - e^{jk\hat{\mathbf{r}} \cdot (\mathbf{r}_1 - 2h\hat{\mathbf{z}})} \right) \mathbf{J}_s(\mathbf{r}_1) dS_1 \\ &= (1 - e^{-j2hk\hat{\mathbf{r}} \cdot \hat{\mathbf{z}}}) \int_{\Omega} e^{jk\hat{\mathbf{r}} \cdot \mathbf{r}_1} \mathbf{J}_s(\mathbf{r}_1) dS_1. \end{aligned} \quad (39)$$

The low-frequency expansion [43] is expressed in the electric  $\mathbf{p}$  and magnetic  $\mathbf{m}$  dipole moments determined from the surface charge  $\varrho_s$  and surface current  $\mathbf{J}_s$  densities in  $\Omega$ , i.e.

$$\mathbf{F}(\hat{\mathbf{r}}) \approx j2hk\hat{\mathbf{r}} \cdot \hat{\mathbf{z}} \frac{k^2}{4\pi\epsilon_0} (\hat{\mathbf{r}} \times (\mathbf{p} \times \hat{\mathbf{r}}) + c_0^{-1}\mathbf{m} \times \hat{\mathbf{r}}), \quad (40)$$

as  $k \rightarrow 0$ , where

$$\mathbf{p} = \int_{\Omega} \mathbf{r} \varrho_s(\mathbf{r}) dS \quad \text{and} \quad \mathbf{m} = \frac{1}{2} \int_{\Omega} \mathbf{r} \times \mathbf{J}_s(\mathbf{r}) dS, \quad (41)$$

and it is assumed that the total charge in region  $\Omega$  is zero. The radiated power for the patch geometry scales as  $k^6$  in the electrically small limit in contrast to  $k^4$  for an electrically small antenna in free space [10], [44]. The corresponding stored energy is independent of  $k$  in the limit  $k \rightarrow 0$  and approaches the static energy. This produces a Q-factor scaling from (6)

$$Q \sim k^{-5} \sim \lambda^5, \quad (42)$$

in contrast to  $Q \geq (ka)^{-3}$  for a spherical region with radius  $a$  in free space [10] and  $Q \geq 6\pi/(\gamma k^3)$  for electric dipole radiators in an arbitrary shaped region with high-contrast polarizability  $\gamma$  [44].

If the height ( $h$ ) is made proportional to the wavelength in free space  $h \sim \lambda$ , this from (40) produces radiated power scaling of  $k^4$ .

## REFERENCES

- [1] J. R. James, P. S. Hall, and C. Wood, *Microstrip antenna theory and design*. Peregrinus on behalf of the Institution of Electrical Engineers London ; New York, 1981.
- [2] D. M. Pozar, "Microstrip antenna," *Proc. IEEE*, vol. 80, no. 1, pp. 79–91, 1992.
- [3] J. R. Mosig and F. E. Gardiol, "A dynamical radiation model for microstrip structures," in *Advances in Electronics and Electron Physics*, P. W. Hawkes, Ed. Academic Press, 1982, vol. 59, pp. 139 – 237.
- [4] (2022) FEKO. Altair. [Online]. Available: <https://altairhyperworks.com/product/Feko>
- [5] (2022) CST Studio Suite 3D EM simulation and analysis software. [Online]. Available: <https://www.cst.com/>
- [6] A. G. Derneryd, "Analysis of the microstrip disk antenna element," *IEEE Trans. Antennas Propag.*, vol. 27, no. 5, pp. 660–664, 1979.
- [7] A. D. Yaghjian and S. R. Best, "Impedance, bandwidth, and Q of antennas," *IEEE Trans. Antennas Propag.*, vol. 53, no. 4, pp. 1298–1324, 2005.

- [8] Y. Rahmat-Samii and E. Michielssen, *Electromagnetic Optimization by Genetic Algorithms*, Wiley Series in Microwave and Optical Engineering. John Wiley & Sons, 1999.
- [9] R. L. Haupt and D. H. Werner, *Genetic Algorithms in Electromagnetics*. Wiley-IEEE Press, 2007.
- [10] L. J. Chu, "Physical limitations of omni-directional antennas," *J. Appl. Phys.*, vol. 19, pp. 1163–1175, 1948.
- [11] M. Gustafsson and S. Nordebo, "Optimal antenna currents for Q, superdirectivity, and radiation patterns using convex optimization," *IEEE Trans. Antennas Propag.*, vol. 61, no. 3, pp. 1109–1118, 2013.
- [12] L. Jelinek and M. Capek, "Optimal currents on arbitrarily shaped surfaces," *IEEE Trans. Antennas Propag.*, vol. 65, no. 1, pp. 329–341, 2017.
- [13] M. Gustafsson, M. Capek, and K. Schab, "Tradeoff between antenna efficiency and Q-factor," *IEEE Trans. Antennas Propag.*, vol. 67, no. 4, pp. 2482–2493, April 2019.
- [14] B. L. G. Jonsson, S. Shi, L. Wang, F. Ferrero, and L. Lizzi, "On methods to determine bounds on the Q-factor for a given directivity," *IEEE Trans. Antennas Propag.*, vol. 65, no. 11, pp. 5686–5696, 2017.
- [15] M. Capek, M. Gustafsson, and K. Schab, "Minimization of antenna quality factor," *IEEE Trans. Antennas Propag.*, vol. 65, no. 8, pp. 4115–4123, 2017.
- [16] A. Sommerfeld, "Über die Ausbreitung der Wellen in der drahtlosen Telegraphie," *Annalen der Physik*, vol. 333, pp. 665–736, 1909.
- [17] J. R. Mosig, "Integral equation techniques for 3D microstrip structures," *Review of Radio Science*, pp. 127–153, 1993.
- [18] R. Garg, P. Bhartia, I. Bahl, and A. Ittipiboon, *Microstrip Antenna Design Handbook*. Artech House, 2001.
- [19] J. R. James and P. S. Hall, *Handbook of microstrip antennas*. Peregrinus on behalf of the Institution of Electrical Engineers London, U.K, 1989.
- [20] J.-F. Zürcher and F. E. Gardiol, *Broadband Patch Antennas*. Boston, MA: Artech House, 1995, iSBN 0-89006-777-5.
- [21] A. Skrivervik, J.-F. Zurcher, O. Staub, and J. Mosig, "PCS antenna design: the challenge of miniaturization," *IEEE Antennas and Propagation Magazine*, vol. 43, no. 4, pp. 12–27, 2001.
- [22] D. Tayli and M. Gustafsson, "Physical bounds for antennas above a ground plane," *IEEE Antennas Wireless Propag. Lett.*, vol. 15, pp. 1281–1284, 2016.
- [23] D.-H. Kwon and D. M. Pozar, "Spectral-domain radiation Q analysis of a planar dipole over a conducting ground plane," in *2015 IEEE International Symposium on Antennas and Propagation USNC/URSI National Radio Science Meeting*, 2015, pp. 1404–1405.
- [24] V. Palanisamy and R. Garg, "Rectangular ring and H-shaped microstrip

- antennas Alternatives to rectangular patch antenna,” *Electronics Letters*, vol. 21, pp. 874–876, Sep. 1985.
- [25] T. Huynh and K.-F. Lee, “Single-layer single-patch wideband microstrip antenna,” *Electronics Letters*, vol. 31, pp. 1310–1312, 1995.
- [26] R. F. Harrington, *Field Computation by Moment Methods*. New York, NY: Macmillan, 1968.
- [27] G. A. E. Vandenbosch, “Reactive energies, impedance, and Q factor of radiating structures,” *IEEE Trans. Antennas Propag.*, vol. 58, no. 4, pp. 1112–1127, 2010.
- [28] K. Schab, L. Jelinek, M. Capek, C. Ehrenborg, D. Tayli, G. A. Vandenbosch, and M. Gustafsson, “Energy stored by radiating systems,” *IEEE Access*, vol. 6, pp. 10 553 – 10 568, 2018.
- [29] M. Gustafsson and C. Ehrenborg, “State-space models and stored electromagnetic energy for antennas in dispersive and heterogeneous media,” *Radio Sci.*, vol. 52, 2017.
- [30] R. F. Harrington and J. R. Mautz, “Control of radar scattering by reactive loading,” *IEEE Trans. Antennas Propag.*, vol. 20, no. 4, pp. 446–454, 1972.
- [31] M. Gustafsson, D. Tayli, C. Ehrenborg, M. Cismasu, and S. Nordebo, “Antenna current optimization using MATLAB and CVX,” *FERMAT*, vol. 15, no. 5, pp. 1–29, 2016. [Online]. Available: [https://efermat.github.io/articles/Gustafsson-ART-2016-Vol15-May\\_Jun-005/](https://efermat.github.io/articles/Gustafsson-ART-2016-Vol15-May_Jun-005/)
- [32] M. Gustafsson, K. Schab, L. Jelinek, and M. Capek, “Upper bounds on absorption and scattering,” *New Journal of Physics*, vol. 22, no. 073013, 2020.
- [33] M. Gustafsson and M. Capek, “Maximum gain, effective area, and directivity,” *IEEE Trans. Antennas Propag.*, vol. 67, no. 8, pp. 5282–5293, 2019.
- [34] A. Beck and Y. C. Eldar, “Strong duality in nonconvex quadratic optimization with two quadratic constraints,” *SIAM Journal on Optimization*, vol. 17, no. 3, pp. 844–860, 2006.
- [35] J.-E. Sten, A. Hujanen, and P. Koivisto, “Quality factor of an electrically small antenna radiating close to a conducting plane,” *IEEE Trans. Antennas Propag.*, vol. 49, no. 5, pp. 829–837, May 2001.
- [36] S. P. Boyd and L. Vandenberghe, *Convex Optimization*. Cambridge Univ. Pr., 2004.
- [37] R. F. Harrington, *Time Harmonic Electromagnetic Fields*. New York, NY: McGraw-Hill, 1961.
- [38] D. M. Pozar, “New results for minimum Q, maximum gain, and polarization properties of electrically small arbitrary antennas,” in *Antennas and Propagation, 2009. EuCAP 2009. 3rd European Conference on*, March 2009, pp. 1993–1996.

- [39] M. N. Hasan, S. W. Shah, M. I. Babar, and Z. Sabir, "Design and simulation based studies of a dual band u-slot patch antenna for wlan application," in *2012 14th International Conference on Advanced Communication Technology (ICACT)*, 2012, pp. 997–1001.
- [40] J. R. Mosig, R. C. Hall, and F. E. Gardiol, "Numerical analysis of microstrip patch antennas," in *Handbook of Microstrip Antennas*, J. R. James and P. S. Hall, Eds. London: Peregrinus, 1989, pp. 391–453.
- [41] E. Talvila, "Necessary and sufficient conditions for differentiating under the integral sign," *The American Mathematical Monthly*, vol. 108, no. 6, pp. 544–548, 2001.
- [42] K. A. Michalski and J. R. Mosig, "Efficient computation of Sommerfeld integral tails – methods and algorithms," *Journal of Electromagnetic Waves and Applications*, vol. 30, no. 3, pp. 281–317, 2016.
- [43] G. Kristensson, *Scattering of Electromagnetic Waves by Obstacles*. Edison, NJ: SciTech Publishing, an imprint of the IET, 2016.
- [44] M. Gustafsson, C. Sohl, and G. Kristensson, "Physical limitations on antennas of arbitrary shape," *Proc. R. Soc. A*, vol. 463, pp. 2589–2607, 2007.



## Paper II

## Paper II

*Reproduced, with permission, from: IEEE*

B. A. P. Nel, A. K. Skrivervik, and M. Gustafsson. Radiation Efficiency and Gain Bounds for Microstrip Patch Antennas. Transactions on Antennas and Propagation, (Early Access), 2024. doi: 10.1109/TAP.2024.3514318

# Radiation Efficiency and Gain Bounds for Microstrip Patch Antennas

Ben A.P. Nel, Anja K. Skrivervik, and Mats Gustafsson, *Senior Member, IEEE*

## Abstract

This paper presents bounds on radiation efficiency and gain for microstrip patch antennas, demonstrating close alignment with the performance of classic antenna designs. These bounds serve as effective benchmarks for assessing antenna performance and evaluating trade-offs and design feasibility. The study particularly addresses the trade-off between miniaturization and performance by comparing bounds for antennas of similar size and frequency, achieved either by using high-permittivity substrates or by optimizing the metallic patch design area. To enhance usability, scaling laws are applied, enabling these bounds to be approximated across a range of frequencies using only data from a half-wavelength patch antenna simulation or measurement. Additionally, the study finds a strong correlation between the established radiation efficiency bounds and lower Q-factor limits (indicative of maximum bandwidth). This relationship is highly advantageous in the design process, as it illustrates how bandwidth and radiation efficiency can be optimized together.

## Index Terms

Microstrip patch antennas, physical bounds, radiation efficiency, gain, method of moments

## I. INTRODUCTION

Corresponding author: Ben A.P. Nel.

This work was supported by Excellence Center at Linköping – Lund in Information Technology (ELLIT) and the Hedda Andersson guest professor program at Lund University.

Ben A.P. Nel and Mats Gustafsson are with the Department of Electrical and Information Technology, Lund University, SE-221 00 Lund, Sweden (e-mail: {ben.nel,mats.gustafsson}@eit.lth.se).

Anja K. Skrivervik is with the Microwave Antenna Group, École Polytechnique Fédérale de Lausanne (EPFL), 1015 Lausanne, Switzerland and the Department of Electrical and Information Technology, Lund University, SE-221 00 Lund, Sweden (e-mail: anja.skrivervik@epfl.ch).

**M**ICROSTRIP patch antennas have been widely used for several decades [1], [2], [3]. Today, these antennas can be accurately modeled using commercially available computational electromagnetic software, such as, FEKO [4] or CST [5]. Making use of these simulation tools, antenna designers are able to determine performance parameters including radiation efficiency, gain, and bandwidth.

Radiation efficiency and gain are crucial performance metrics for accessing antenna losses. However, there is limited knowledge about the performance limitations of these parameters in the context of microstrip patch antennas. Understanding these performance limitations can enhance the antenna design process and lead to innovative designs. Early work computing radiation efficiency and gain bounds for antennas in free space can be found in [6]. More recent work has focused on using current optimization to obtain radiation efficiency bounds for arbitrary geometries [7], [8].

The goal of this paper is to aid microstrip patch antenna design by providing radiation efficiency and gain bounds. This is achieved by considering all possible patch geometries within a given design region using current optimization [9]. Some classical patch antenna designs are shown to perform near the bounds both for Ohmic losses in the patch region as well as for dielectric losses in the substrate. Therefore, practical design information is provided regarding the feasibility of obtaining the desired radiation efficiency as well as a benchmark to assess potential design improvements. The work presented here builds on previous formulations determining lower Q-factor bounds for microstrip patch antennas [10], [11].

In this paper, a single-layer microstrip patch antenna is considered, where currents are confined horizontally within the patch design region. To reduce the computational complexity, the ground plane and dielectric substrate are assumed to be infinite. These assumptions are known to be reasonable for moderately sized ground planes and dielectric substrates [2]. These microstrip patch antennas can be fed *e.g.*, with a probe feed coming from the ground plane. Note that there exist methods that may be used to improve the radiation efficiency of a self-resonant microstrip patch antenna, for instance using a shorting pin or by reducing the size of the ground plane and dielectric substrate [12], [13], [14], [15], which are not considered here. However, the bounds presented here serve as a first canonical case for analyzing maximum radiation efficiency for antennas that are in wide use.

Here, miniaturization refers to reducing the patch design region below its natural resonance in free space, such as approximately half a free-space wavelength for a rectangular design. Two methods for achieving miniaturization are evaluated: increasing the substrate permittivity (which enlarges the electrical size of the design region) and shaping the patch by removing metal from the patch

design region. The latter method can reduce the natural half wavelength (in the dielectric substrate) resonance frequency of the metal design region by forcing the current density around slots. Miniaturization is often required even though it is well known that reducing antenna size is challenging, coming at the cost of radiation efficiency [12], [13], [16].

Radiation efficiency and gain are recognized as critical design parameters for microstrip patch antennas, yet bandwidth is equally important for comprehensive performance evaluation [10]. This paper bridges the gap between maximum radiation efficiency and lower Q-factor bounds (directly related to the bandwidth). This is achieved by deriving an approximate expression that calculates radiation efficiency from the Q-factor. This relationship not only enhances the understanding of microstrip patch antenna performance but also provides a practical tool for antenna designers to optimize designs, ensuring that efficiency and bandwidth are simultaneously addressed.

The remainder of the paper is structured as follows; Section II introduces the microstrip patch antenna model and outlines the evaluation process for radiation efficiency and gain. Section III formulates the procedure to compute radiation efficiency and gain bounds using current optimization. Further, patch design region miniaturization is investigated in Section IV. Then, using derived semi-analytic expressions, Section V discusses bounds scaling for Ohmic and dielectric losses. Section VI provides a link between minimum Q-factor and maximum radiation efficiency. A brief discussion on adding vertical currents between the ground plane and patch antenna is presented in Section VII. The paper is concluded in Section VIII. Finally, the appendices provide additional mathematical and procedural details and summarize the used variables.

## II. MICROSTRIP PATCH ANTENNA MODEL

The geometry considered to model microstrip patch antennas is shown in Figure 1, where the design region  $\Omega$ , that can be of arbitrary shape, is situated at the interface between free space and a transversely infinite dielectric substrate. This dielectric, with relative permittivity  $\epsilon_r$  and thickness  $h$ , is on top of an infinite PEC ground plane.

In this paper, a rectangular design region  $\Omega$ , is chosen for simplicity, see Fig 2a. Classical patch geometries fitting within this rectangular design region, such as a half-wavelength patch (a) as well as miniaturized geometries that reduce the resonant frequency *e.g.*, slot loaded patch [17] (b), and H-shaped patch [17] (c), are shown in Figure 2. The radiation efficiency and gain of these classical patch geometries serve as a reference with which to compare the presented bounds. It should be noted that these bounds consider all possible patch geometries fitting within the design region  $\Omega$ , thereby obtaining a fundamental limit on achievable maximum radiation efficiency and gain for antenna geometries within  $\Omega$ .

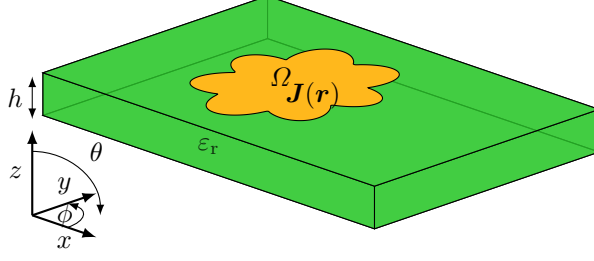


Figure 1: The microstrip patch antenna design region is given by  $\Omega$ . All metal patch geometries fitting within this region are considered. Surface current densities on this design region are denoted,  $\mathbf{J}(\mathbf{r})$ . The infinite dielectric substrate with relative permittivity,  $\epsilon_r$ , and thickness,  $h$ , is on top of an infinite PEC ground plane.

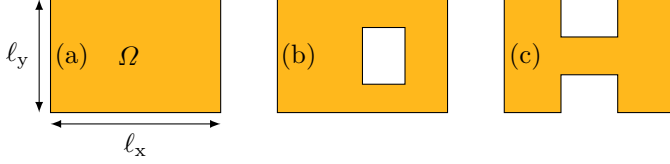


Figure 2: A rectangular design region  $\Omega$ , see Figure 1, having dimensions  $\ell_x$  and  $\ell_y$  is chosen in this paper. Classical metal patch geometries such as the half-wavelength patch (a), the slot-loaded patch (b), and the H-shaped patch (c) fit within this design region.

Radiation efficiency and gain are defined as [6]

$$\eta = \frac{P_r}{P_d} \quad \text{and} \quad G = 4\pi \frac{U}{P_d}, \quad (1)$$

respectively, where  $P_r$  denotes radiated power,  $P_d$  dissipated (accepted) power, and  $U$  radiation intensity. For a microstrip patch antenna, the dissipated power can be due to three different loss mechanisms that can be separately analyzed as

$$P_d = P_r + P_\Omega + P_\epsilon, \quad (2)$$

where the Ohmic losses on the patch are given by  $P_\Omega$  and losses in the substrate due to dielectric losses and surface waves are given by  $P_\epsilon$ . In reality, the dielectric substrate is always finite, leading to radiation from surface wave diffraction on the edge. However, this form of radiation is generally undesirable and therefore considered as a loss when analyzing radiation efficiency and gain [18]. The remainder of this section focuses on how to analyze the dissipated power, radiation intensity, and radiated power to evaluate the radiation efficiency and

gain (1) in a way suitable for current optimization [9]. It should be noted that Ohmic losses on the ground plane are not considered in this paper.

For a given microstrip patch antenna geometry and feed, the total dissipated power ( $P_d$ ) can be determined from the input voltage and current. However, in this paper, all possible geometries on a design region need to be considered and therefore another approach is required. To formulate a current optimization problem, all patch currents need to be related to dissipated power. This can be done using the method of moments (MoM) [19]. By making use of Green's functions, incorporating the effect of the dielectric substrate and the ground plane [18], the only unknowns of the system are the currents on the design region, see Figure 1. The current density  $\mathbf{J}(\mathbf{r})$  in the design region  $\Omega$  is expanded in  $N$  basis functions  $\psi_n(\mathbf{r})$  as

$$\mathbf{J}(\mathbf{r}) = \sum_{n=1}^N I_n \psi_n(\mathbf{r}), \quad (3)$$

where the position vector is given by  $\mathbf{r}$ . The MoM impedance matrix  $\mathbf{Z} \in \mathbb{C}^{N \times N}$  relates design region currents to voltages as [19]

$$\mathbf{Z}\mathbf{I} = \mathbf{V}, \quad (4)$$

where the expansion coefficient  $I_n$  are collected in  $\mathbf{I} \in \mathbb{C}^{N \times 1}$  and excitation voltages in  $\mathbf{V} \in \mathbb{C}^{N \times 1}$ . The MoM resistance matrix and reactance matrix are expressed in terms of the impedance matrix as

$$\mathbf{R} = \frac{\mathbf{Z} + \mathbf{Z}^H}{2} \quad \text{and} \quad \mathbf{X} = \frac{\mathbf{Z} - \mathbf{Z}^H}{2j}, \quad (5)$$

respectively, where the Hermitian transpose is denoted by superscript  $^H$  and  $j^2 = -1$ .

The dissipated power (2) required to obtain radiation efficiency and gain (1) can be computed from the patch currents (3) and MoM resistance matrix (5) as [19]

$$P_d = \frac{1}{2} \mathbf{I}^H \mathbf{R} \mathbf{I}. \quad (6)$$

To formulate efficiency and gain optimization problems, it is also required to relate patch currents to radiation intensity and radiated power. For this, analytic expressions of the far-field radiated by a horizontal electric (Hertzian) dipole (HED) located on top of the dielectric slab are used to determine the far-field of the basis functions in (3), see Appendix B for details. This relationship is used to relate the currents to the far-field in any arbitrary direction  $(\theta, \phi)$  as

$$\mathbf{F}(\theta, \phi) \approx \mathbf{F} \mathbf{I}, \quad (7)$$

where the far-field matrix  $\mathbf{F} \in \mathbb{C}^{2 \times N}$  relates patch currents to the far-field direction with  $\hat{\boldsymbol{\theta}}$  and  $\hat{\boldsymbol{\phi}}$  components.

The radiation intensity in a direction  $(\theta, \phi)$  used to evaluate gain in (1) is given by

$$U = \frac{|\mathbf{F}|^2}{2Z_0}. \quad (8)$$

From this, the radiated power is calculated by integrating over a hemispherical surface on the free-space side of the design region, neglecting surface wave effects near the grazing angle ( $\theta = \pi/2$ ). Using a set of quadrature points  $(\theta_n, \phi_n)$  together with quadrature weights, a matrix  $\mathbf{F}_s$  is constructed by using far-field matrices  $\mathbf{F}$  in (7) evaluated at  $(\theta_n, \phi_n)$  as rows. For simplicity, square roots for the quadrature weights are incorporated into  $\mathbf{F}_s$  such that the radiated power  $P_r$  from patch currents  $\mathbf{I}$  is determined by a radiation resistance matrix  $\mathbf{R}_r = \mathbf{F}_s^H \mathbf{F}_s$  *i.e.*,

$$P_r = \frac{1}{2} \mathbf{I}^H \mathbf{F}_s^H \mathbf{F}_s \mathbf{I} = \frac{1}{2} \mathbf{I}^H \mathbf{R}_r \mathbf{I}. \quad (9)$$

### III. BOUNDS ON RADIATION EFFICIENCY AND GAIN

This section formulates and presents upper bounds on radiation efficiency and gain using current optimization [7], [20]. Maximal efficiency (1) is in the form of a Rayleigh quotient [19], which can also be written as a quadratically constrained quadratic program (QCQP) [21] as

$$\begin{aligned} & \text{maximize} && \mathbf{I}^H \mathbf{R}_r \mathbf{I} \\ & \text{subject to} && \mathbf{I}^H \mathbf{R}_i \mathbf{I} = 2P_{\text{in}}, \end{aligned} \quad (10)$$

where the choice of input power  $P_{\text{in}}$  does not affect the bounds but only scales the currents. The solution of this optimization problem is in the form of a generalized eigenvalue problem [19]  $\eta_{\text{up}} = \max \text{eig}(\mathbf{R}_r, \mathbf{R}_i)$ .

To enforce self-resonance in the radiation efficiency optimization problem (10), the reactive power is set to zero to model a real-valued input impedance ( $\text{Im } Z_{\text{in}} = 0$ ). This additional reactive power constraint is written as a quadratic form over the reactance matrix ( $\mathbf{X}$ ) in (5) and reduces the search space of possible optimal currents resulting in the optimization problem

$$\begin{aligned} & \text{maximize} && \mathbf{I}^H \mathbf{R}_r \mathbf{I} \\ & \text{subject to} && \mathbf{I}^H \mathbf{R}_i \mathbf{I} = 2P_{\text{in}} \\ & && \mathbf{I}^H \mathbf{X} \mathbf{I} = 0. \end{aligned} \quad (11)$$

The QCQP (11) can be transformed to a dual problem [20] and written as a parameterized eigenvalue problem using a scalar parameter  $\nu$ . Where, given the condition  $\mathbf{R} + \nu \mathbf{X} \succeq \mathbf{0}$  and an indefinite  $\mathbf{X}$ , the scalar parameter is restricted to the range (29) shown in Appendix C. This leads to the use of the far-field matrix  $\mathbf{F}_s$  in (9) to express the solution of (11) as a parametrized ordinary eigenvalue problem

$$\eta_{\text{ub}} = \min_{\nu} \max \text{eig}(\mathbf{F}_s (\mathbf{R} + \nu \mathbf{X})^{-1} \mathbf{F}_s^H). \quad (12)$$

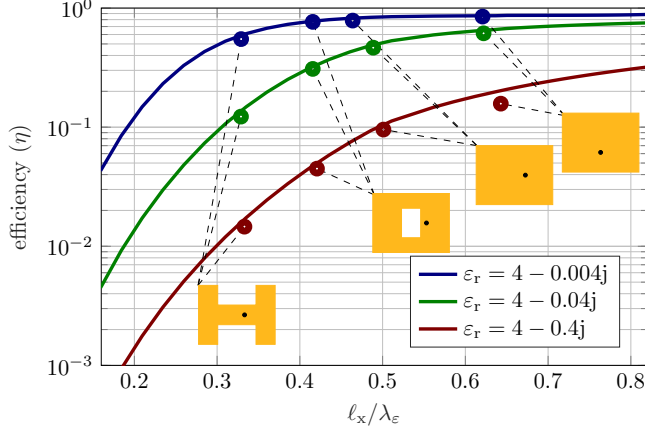


Figure 3: Upper bounds on radiation efficiency for all PEC microstrip patch antennas fitting within a rectangular design region  $\Omega$  with dimensions  $\ell_y = 0.77\ell_x$  (see Figure 2) having dielectric loss tangents  $\tan \delta \in \{0.001, 0.01, 0.1\}$  and substrate thickness  $h = 0.05\ell_x$  (see Figure 1). Radiation efficiencies computed using FEKO are shown by markers for the indicated patch antenna geometries (see insets a-c in Figure 2).

It should be noted that a simultaneous diagonalization of  $\mathbf{R}$  and  $\mathbf{X}$  can be used to reduce the computational complexity in (12) by inverting a diagonal matrix [20]. There is typically no dual gap for the QCQPs presented here with one or two quadratic constraints [22]. Therefore, the optimal currents (11) can be determined from eigenvectors in (12).

Figure 3 shows upper bounds on the radiation efficiency computed for PEC microstrip patch antennas with a dielectric substrate having  $\text{Re}\{\epsilon_r\} = 4$  and loss tangent  $\tan \delta \in \{0.001, 0.01, 0.1\}$  using (12). The design region  $\Omega$  has dimensions  $\ell_y = 0.77\ell_x$  and substrate thickness  $h = 0.05\ell_x$  (see Figure 1), where again it should be noted that the bounds provide a performance limit for all possible patch geometries within the design region. The bounds are shown for a varying patch length  $\ell_x$  normalized by the dielectric wavelength,  $\lambda_\epsilon = \lambda/\sqrt{\text{Re}\epsilon_r}$  (neglecting the imaginary part of permittivity). The bounds are tight from a practical point of view, as shown by the comparison with realistic antennas with an infinite ground plane simulated using commercial software (FEKO) and indicated by the markers to have near optimal performance. For instance, the half-wavelength patch (see Figure 2a) is shown to be essentially on the bounds for all presented loss tangents with only a slight deviation from the bounds when exciting the half-wavelength resonance along the shorter dimension ( $\ell_y$ ) and increasing the loss tangent to  $\tan \delta = 0.1$ . However, this deviation could

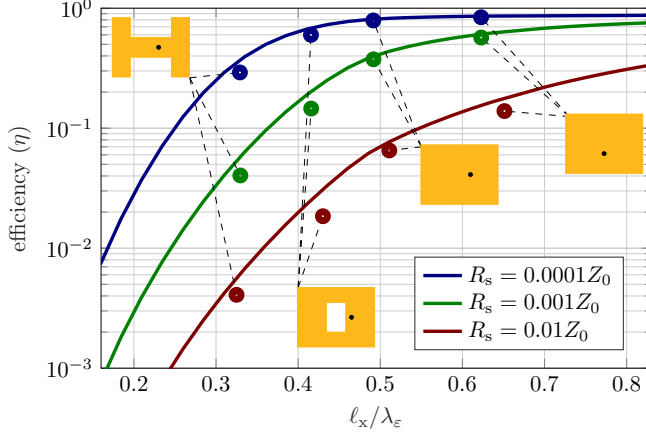


Figure 4: Upper bounds on the radiation efficiency for all microstrip patch antennas fitting within the rectangular design region with dimensions  $\ell_y = 0.77\ell_x$ , specified Ohmic losses, relative permittivity  $\epsilon_r = 4$ , and substrate thickness  $h = 0.05\ell_x$ . Radiation efficiencies for the classical patches in Figure 2 computed using FEKO are shown by markers.

potentially be minimized with a different feeding configuration. Considering miniaturized geometries, performance near the bounds is also observed for the slot-loaded patch (see Figure 2b) as well as the H-shaped patch (see Figure 2c).

The results in Figure 3, as expected, show that when the dielectric loss tangent is decreased or the electrical size is increased, the maximum radiation efficiency increases. For design regions smaller than half a wavelength in the dielectric ( $\ell_x/\lambda_\epsilon < 0.5$ ), the bounds show that for a high loss tangent *e.g.*,  $\tan \delta = 0.1$  miniaturized designs perform relatively poorly. To demonstrate this compare the bounds for  $\tan \delta = 0.1$  at  $\ell_x/\lambda_\epsilon \approx 1/3$  (realized by the H-shaped patch) around 1.5% efficiency and  $\ell_x/\lambda_\epsilon \approx 1/2$  (realized by half wavelength patch) around 10% efficiency. For a loss tangent  $\tan \delta = 0.001$  the same comparison leads to bounds at  $\ell_x/\lambda_\epsilon \approx 1/3$  of around 60% and at  $\ell_x/\lambda_\epsilon \approx 1/2$  around 80%. This emphasizes the importance of choosing a substrate with low dielectric losses when considering antennas that are smaller than half a wavelength in the dielectric. It should be noted that further improvements in radiation can be achieved using designs larger than  $\ell_x/\lambda_\epsilon > 0.5$ . This is done by exciting a half wavelength resonance on the shorter dimension ( $\ell_y$ ) as is well known. This is confirmed by both the bounds and the simulated patch antennas.

Radiation efficiency bounds computed using (12) for patches with varying surface resistivity  $R_s \in \{0.0377, 0.377, 3.77\} \Omega/\square$  (ohms per square) and a lossless dielectric are shown in Figure 4. The surface resistivity can model either a

resistive sheet or a solid conductor with a skin depth [23]. To demonstrate the practical application of the bounds, the performance of different patch designs (see Figure 2), is compared to the bounds using FEKO. This shows that the half-wavelength-patches (see Figure 2a) are essentially on the bounds and therefore optimal for these surface resistivities. Further, the slot-loaded patch (see Figure 2b) and H-shaped patch (see Figure 2c) perform near the bounds. The reason the slot-loaded patch and the H-shaped patch do not align with the bounds is that the currents are constrained in these designs, leading to high current densities resulting in less efficient use of the available surface area. Similar to Figure 3 it is observed that increasing design region dimensions may be used to compensate for high losses.

A further parameter of interest is gain (1). Upper bounds on gain can be determined by maximization of the radiation intensity and written as the current optimization problem

$$\begin{aligned} & \text{maximize} && \mathbf{I}^H \mathbf{F}^H \mathbf{F} \mathbf{I} \\ & \text{subject to} && \mathbf{I}^H \mathbf{R} \mathbf{I} = 2P_{\text{in}} \\ & && \mathbf{I}^H \mathbf{X} \mathbf{I} = 0, \end{aligned} \tag{13}$$

which can be formulated as an eigenvalue problem (see Appendix C for more information) using the range computed for  $\nu$  in (29) as [20]

$$G_{\text{ub,r}} \approx 4\pi \min_{\nu} \max \text{eig}(\mathbf{F}(\mathbf{R} + \nu \mathbf{X})^{-1} \mathbf{F}^H). \tag{14}$$

Upper bounds on gain for microstrip patch antennas with relative permittivity having real part  $\text{Re}\{\varepsilon_r\} = 4$ , varying loss tangent, substrate thickness  $h = 0.05\ell_x$  and design region dimensions  $\ell_y = 0.77\ell_x$  are shown in Figure 5. The bounds show that, as expected, an increased dielectric loss tangent reduces the gain. Further, the corresponding directivity ( $D = G/\eta$ ) values, shown by dashed lines, are on top of one another with only a weak dependence on the electrical size of the design region. This suggests that the maximum achievable gain is scaled by achievable radiation efficiency with directivity relatively unaffected. The gain bounds on Ohmic losses are not shown here, however, they lead to the same conclusion on directivity as the bounds with dielectric losses presented in Figure 5. This suggests that directivity is mostly determined by the electrical size of the structure when maximizing gain.

#### IV. SUBSTRATE IMPACT ON ANTENNA MINIATURIZATION

In this section, the trade-off between antenna miniaturization and radiation efficiency bounds is investigated. Miniaturizing patch antennas can be achieved by increasing the substrate's relative permittivity and/or shaping the patch geometry. A comparison between these two approaches for a given design region and free-space wavelength is provided here. This is done for a design region

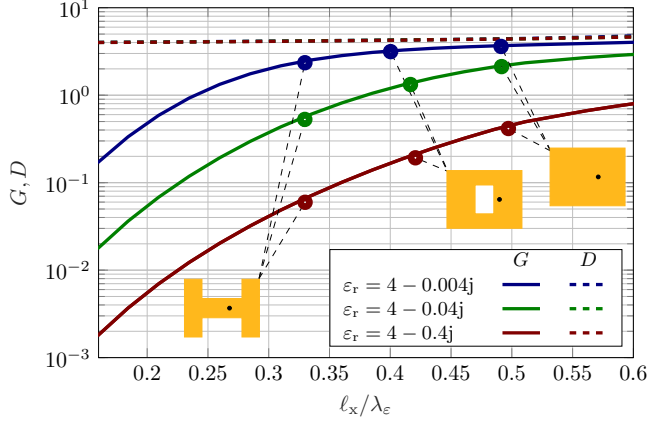


Figure 5: Upper bounds on the gain in the normal direction,  $\hat{z}$ , for microstrip patch antennas fitting within a rectangular design region with dimensions  $\ell_y = 0.77\ell_x$ , relative permittivity  $\text{Re}\{\varepsilon_r\} = 4$ , loss tangents  $\tan \delta \in \{0.001, 0.01, 0.1\}$ , and substrate thickness  $h = 0.05\ell_x$ . The corresponding realized directivities are shown by dashed lines.

with dimensions  $\ell_y = 0.77\ell_x$ , substrate thickness  $h = 0.05\ell_x$ , and relative permittivities  $\text{Re}\{\varepsilon_r\} = 2$  and  $\text{Re}\{\varepsilon_r\} = 4$ , investigating Ohmic as well as dielectric losses separately. In addition, the radiation efficiency bounds are compared to measurements of miniaturized patch antennas for a given substrate.

A comparison of the efficiency bounds for different substrate relative permittivities is shown in Figure 6 for patch Ohmic losses of  $R_s = 0.01 \Omega/\square$  (similar to copper) and lossless dielectrics. It is evident that the higher relative permittivity substrate ( $\varepsilon_r = 4$ ) has greater radiation efficiency bounds than the lower permittivity ( $\varepsilon_r = 1$  and  $\varepsilon_r = 2$ ) substrates, for structures miniaturized below its half a wavelength (in the  $\varepsilon_r = 4$  substrate)  $\ell_x/\lambda < 0.25$ . The enhanced efficiency of the high permittivity substrate ( $\varepsilon_r = 4$ ) can be attributed in part to its greater electrical thickness. This is demonstrated by comparing its efficiency bound with that of a thinner substrate,  $h = 0.0354\ell_x$ , equivalent to the electrical thickness of the  $\varepsilon_r = 2$  material. The results indicate that the substrate's electrical thickness is a critical factor in determining efficiency bounds for designs smaller than half a wavelength.

The performance differences among the various substrates become less pronounced for  $\ell_x/\lambda > 0.25$ , where all scenarios exhibit efficiencies ranging from around 85% to 95%. The  $\varepsilon_r = 2$  substrate demonstrates marginally better performance up to  $\ell_x/\lambda \approx 0.3$ , beyond which the free-space scenario ( $\varepsilon_r = 1$ ) excels. In this range, efficiency bounds for the two  $\varepsilon_r = 4$  substrates are

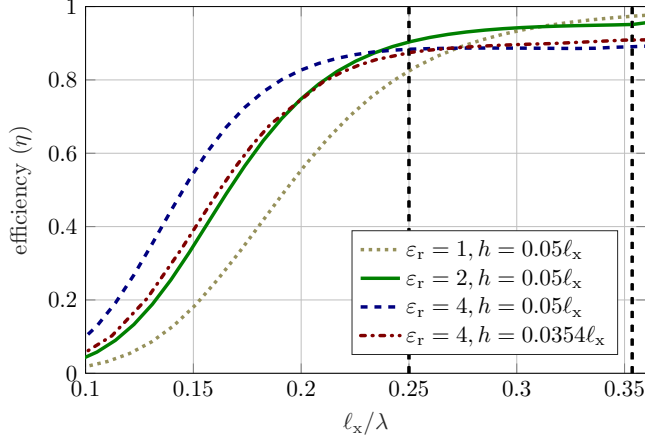


Figure 6: Upper bounds on radiation efficiency with surface resistivity  $R_s = 0.01 \Omega/\square$ . The design region has dimensions  $\ell_y = 0.77\ell_x$  and the substrate thickness  $h$  and relative permittivity  $\varepsilon_r$  are indicated in the legend. The vertical dashed lines indicate the half wavelength size for substrates with relative permittivity of 2 and 4.

comparable, with slightly better performance observed for the thinner substrate. The intricate behavior within this range arises from a combination of increased electrical size and increased surface wave losses for the higher permittivity substrates.

Further, considering only dielectric losses, the radiation efficiency bounds for relative permittivity  $\varepsilon_r = 2(1 - j \tan \delta)$  and  $\varepsilon_r = 4(1 - j \tan \delta)$  substrates are compared as shown in Figure 7. The interpretation remains consistent for the low-loss substrate with  $\tan \delta = 0.001$ , similar to the Ohmic losses depicted in Figure 6. Specifically, the high permittivity substrate ( $\text{Re}\{\varepsilon_r\} = 4$ ) exhibits the highest efficiency bound below  $\ell_x/\lambda < 0.25$ , while the lower permittivity substrate ( $\text{Re}\{\varepsilon_r\} = 2$ ) outperforms it above  $\ell_x/\lambda > 0.25$ . Once more, this phenomenon primarily stems from the larger electrical size in electrically small cases and the increased surface wave power for larger sizes. Using a thinner substrate of  $h = 0.0354\ell_x$  reduces the efficiency, bringing the values closer to those of the  $\text{Re}\{\varepsilon_r\} = 2$  case, although with a disparity larger than observed for the Ohmic losses in Figure 6.

In the case of higher dielectric losses with  $\tan \delta = 0.01$ , the higher permittivity substrate exhibits superior performance across the entire range  $\ell_x/\lambda < 0.36$ . This can be attributed in part to the dominance of material losses, which hide the impact of surface waves, resulting in lower efficiency overall. Furthermore, the enhancement observed beyond the dielectric's half a wavelength,  $\ell_x/\lambda > 0.25$ , is

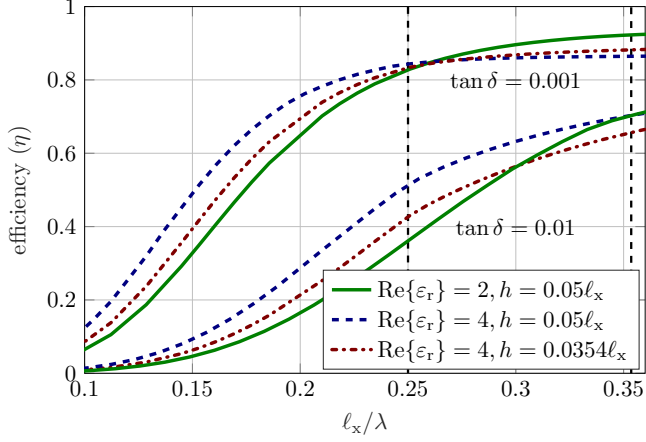


Figure 7: Upper bounds on radiation efficiency for two relative permittivities with substrate loss tangents  $\tan \delta \in [0.01, 0.001]$ . The design region has dimensions  $\ell_y = 0.77\ell_x$  and indicated substrate thickness  $h$  and relative permittivity  $\varepsilon_r$  in the legend. The vertical dashed lines indicate the half wavelength size for substrates with relative permittivity of 2 and 4.

attributable to the fact that the  $\ell_y$ -direction becomes half a wavelength increasing the width of the patch.

Based on these investigations, it is recommended that when considering miniaturization, a higher permittivity substrate should be preferred over reshaping the design region. The exact range over which it remains favorable to do so depends on several factors such as surface wave losses. From the cases considered here, it is observed that for low-loss cases it is favorable to miniaturize by increasing relative permittivity up to around half a wavelength. To better understand this a further study of how the surface wave depends on design parameters is presented in Section V.

For a given dielectric substrate, the bounds can be compared to measured antenna designs. This is both a validation of the bounds' usefulness for a finite ground plane as well as an investigation of miniaturized designs on the same dielectric substrate. The FR4 dielectric substrate chosen has dimensions  $100 \text{ mm} \times 100 \text{ mm}$  with thickness  $3.3 \text{ mm}$  and relative permittivity  $\varepsilon_r \approx 4.29(1 - j0.015)$ , based on material characterization at  $2 \text{ GHz}$  [24]. Three different design regions are considered and their radiation efficiency bounds determined between  $1.6 \text{ GHz} - 2 \text{ GHz}$  as indicated in Figure 8. The smallest design region ( $\Omega_C$ ) has significantly lower radiation efficiency bounds than the other two design regions ( $\Omega_A$  and  $\Omega_B$ ). When comparing the two largest design regions, the one with the largest maximum dimension has higher radiation efficiency bounds, confirming

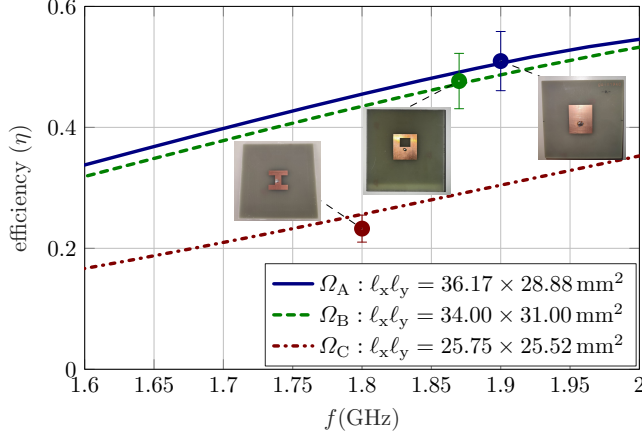


Figure 8: Upper bounds on radiation efficiency compared with measurements. The efficiency of three measured antennas is shown with markers. The design region's dimensions are given in the legend. The relative permittivity of the  $h = 3.3$  mm thick substrate is  $\epsilon_r = 4.29(1 - j0.015)$  and the used surface resistivity of copper is  $R_s = 0.01 \Omega/\square$ . Error bars are based on the precision of the measurement. The ground plane has dimensions  $100 \text{ mm} \times 100 \text{ mm}$ .

that for miniaturized geometries it is generally favorable to increase the largest dimension.

Since a finite ground plane is used, part of the undesired surface wave power is detected as radiated power in the measurement. However, since the ground plane is relatively large compared to the design region, the bounds should still be a good indication of optimal performance [2]. Should the surface wave have a larger effect on the radiation efficiency such as in the case of an electrically thicker dielectric substrate then this should be accounted for. When comparing the half-wavelength patch with design dimensions  $\Omega_A$  at 1.9 GHz to the bounds, the measured radiation efficiency is found to be very close to these bounds. Similarly, for the slot-loaded patch (designed within the design region  $\Omega_B$ ) the measured radiation efficiency is close to the bounds at 1.87 GHz. The H-shaped patch (designed within the design region  $\Omega_C$ ) has a slight deviation from the bounds at 1.8 GHz.

## V. SEMI-ANALYTIC APPROXIMATION OF BOUNDS

In this section the contribution of substrate and patch loss parameters pertaining to radiation efficiency bounds are further investigated, to see if this effect can be approximated to enhance understanding and simplify computations. With

this, insights can be derived as how the substrate or patch material properties affect the radiation efficiency bounds.

The dissipation factor [6], [7], defined as

$$\Delta = \frac{P_d - P_r}{P_r} = \frac{P_\varepsilon + P_\Omega}{P_r}, \quad (15)$$

is a natural parameter to consider when investigating the effect of loss parameters on the scaling of radiation efficiency bounds (obtained with (12)). The dissipation factor is related to the radiation efficiency as  $\eta = (1 + \Delta)^{-1}$ . Therefore, upper bounds on radiation efficiency provide lower bounds on dissipation factor.

As shown in [7] for antennas in free space, lower bounds on dissipation factor scale linearly with surface resistivity ( $R_s$ ). However, only considering this scaling for microstrip patch antennas does not account for surface wave effects, as, even with lossless materials,  $P_\varepsilon \neq 0$ . To account for this effect, an approximate expression [25]

$$\frac{P_{sw}}{P_r} \approx \Delta_{sw} = \frac{3\pi}{4} \frac{(\text{Re}\{\varepsilon_r\} - 1)^3 kh}{\text{Re}\{\varepsilon_r\}^2 (\text{Re}\{\varepsilon_r\} - 1) + \frac{2}{5} \text{Re}\{\varepsilon_r\}}, \quad (16)$$

relating the surface wave power to the radiated power of a HED is used, see Figure 9. The surface wave is strictly only defined for lossless dielectrics but in (16) it is assumed that the ratio between propagated power in the dielectric and radiated power (9) remains constant with increased loss tangent. Further, due to the choice of thin dielectric substrates, only the first transverse magnetic surface wave mode is propagating [26]. The thickness required to have the first transverse electric surface wave mode propagating in the substrate is  $h > \lambda/(4\sqrt{\varepsilon_r - 1})$  [18] in a lossless substrate. It should be noted that with a finite ground plane, the surface wave (16) introduces edge diffraction, which alters the main lobe of the radiation pattern and leads to the formation of sidelobes and increased back radiation, particularly in the E-plane [2].

For three electrical thicknesses over a range of relative permittivities, the expression (16) is used to approximate the surface wave to radiated power ratio as shown in Figure 9. In the figure the  $h = 0.0125\lambda$  at  $\varepsilon_r = 4$  corresponds to a relative permittivity of 4 substrate at half a dielectric wavelength in Figure 3 and Figure 4. It should be noted that by increasing the relative permittivity higher-order surface wave modes could be excited although this is not the case in Figure 9.

The normalized surface wave power (16) can be approximately removed from the dissipation factor (15) as

$$\Delta_\rho = \Delta - \Delta_{sw}. \quad (17)$$

This is applied to the lower dissipation factor bounds obtained using (12), along with normalizing with the surface resistivity ( $\Delta_\rho Z_0/R_s$ ), as shown in Figure 10.

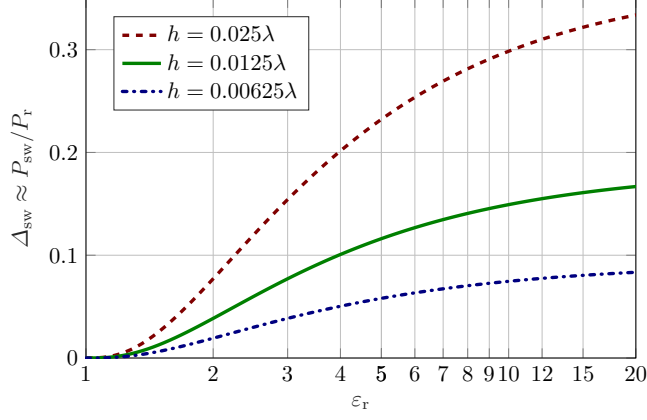


Figure 9: Ratio between the first surface wave mode power ( $P_{\text{sw}}$ ) and radiated power ( $P_r$ ) for an HED approximated by (16). The expression is evaluated over a range of relative permittivities and for three electrical thicknesses.

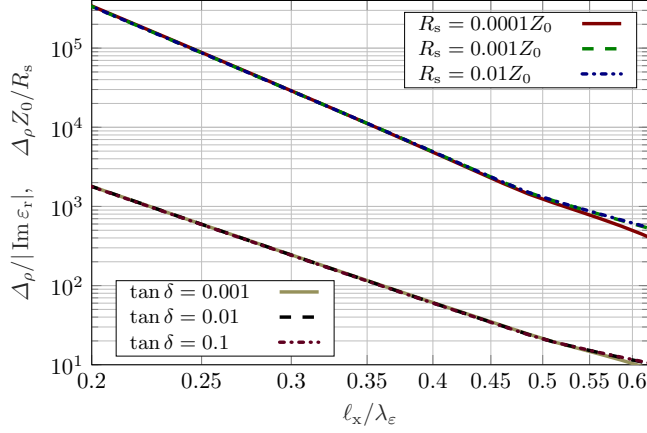


Figure 10: Lower dissipation factor (17) bounds with the surface wave contribution (16) subtracted. The bounds are shown for different surface resistivities normalized by surface resistivity and different dielectric loss tangents normalized by the imaginary part of permittivity. The substrate relative permittivity is  $\text{Re}\{\varepsilon_r\} = 4$ , thickness  $h = 0.05\ell_x$ , and the patch region dimensions are  $\ell_y = 0.77\ell_x$ .

The results show very little difference between the bounds for the different resistivities  $R_s$  when removing the two main contributions (surface resistivity and surface wave). It is noted that as the electrical size increases, the bounds start to deviate slightly. This is due to the surface wave approximation (16) not being accurate for these cases [25] along with the optimal currents trying to suppress these losses as they become more significant. It is very important to note that (16) does not indicate a bound on the ratio between surface wave and radiated power. However, it is an excellent approximation when the surface wave power is not a dominant contribution to radiation efficiency as confirmed in Figure 10.

To investigate the bounds' dependence on dielectric losses, the relationship between dissipated power in the dielectric substrate and the imaginary part of the relative permittivity is required. This is given by

$$P_\epsilon = \frac{-1}{2} \int \text{Im}\{\epsilon_r(\mathbf{r})\} |\mathbf{E}(\mathbf{r})|^2 dV, \quad (18)$$

where it is sufficient to integrate over the volume of the substrate. Assuming that the non-propagating (excluding surface waves) part of the electric field in the substrate remains constant when the dielectric losses are increased, then the dissipation factor (15) should scale linearly with respect to the dielectric losses (18), neglecting the surface wave. Further, as only the real part of the relative permittivity is taken in (16), the ratio between radiated and surface wave power is assumed to remain constant.

The normalized lower bounds on the dissipation factor for varying dielectric loss tangents are shown in Figure 10. The bounds with this normalization, along with subtracting the surface wave power (16), are approximately equal for all presented loss tangents. This means that the lower dissipation factor bounds scale approximately linearly with respect to loss tangent after the approximate surface wave power is removed, implying negligible changes to the near field. Further, the ratio of surface wave power to radiated power approximately follows (16) except for electrically large patches.

## VI. CLOSED FORM EXPRESSION OF MAXIMUM RADIATION EFFICIENCY LINKED TO MINIMUM Q-FACTOR

In this section, a link between stored electric energy in the substrate and dielectric losses is established [27]. This allows for the microstrip patch antenna Q-factor to be related to its radiation efficiency leading to a link between maximum radiation efficiency and minimum Q-factor (maximum bandwidth). This link requires that most of the stored electric energy is confined in the dielectric substrate similar to the assumption made in the cavity model [3]. With this assumption, the stored electric energy can be related to the dissipated power

in the near field (due to dielectric substrate losses) and along with surface wave power (16) can be related to the total dissipated power in the substrate as

$$P_\varepsilon \approx 2\omega W_e \tan \delta + P_{\text{sw}}, \quad (19)$$

where the stored electric energy is given by  $W_e$ . Adding the radiated power to (19) and using the total dissipated power (2), leads to

$$P_d \approx P_r + P_{\text{sw}} + 2\omega W_e \tan \delta, \quad (20)$$

assuming no Ohmic losses. It is useful to rewrite (20) in terms of the Q-factor that can be approximated from the fractional bandwidth or input impedance frequency derivative [28] as shown in Appendix D. This can easily be measured with *e.g.*, a VNA.

Self-resonant antennas have equal stored electric and magnetic energies, which simplifies the Q-factor [28] to

$$Q = \frac{2\omega W_e}{P_d}. \quad (21)$$

Substituting the Q-factor (21) into (20) normalized by dissipated power and identification of the efficiency (1) yields

$$1 \approx \eta + \frac{P_{\text{sw}}}{P_d} + Q \tan \delta. \quad (22)$$

Using the approximation (16) for the surface wave power, the radiation efficiency can be factored out in (22) and expressed as

$$\eta \approx \frac{1 - Q \tan \delta}{1 + \Delta_{\text{sw}}}. \quad (23)$$

Assuming the ratio of surface wave power to radiated power ( $\Delta_{\text{sw}}$ ) remains constant when the loss tangent is increased, it is clear from (23) that minimizing Q-factor is equivalent to maximizing radiation efficiency. This means that maximizing bandwidth and radiation efficiency are closely related for self-resonant microstrip patch antennas.

Lower Q-factor bounds of a lossless substrate can be related to maximum radiation efficiency [29] of a lossy substrate when the radiated Q-factor ( $Q/\eta$ ) is assumed to be invariant with respect to loss tangent, as suggested by results presented in Figure 10. The lower Q-factor bounds for a patch antenna on a lossless substrate ( $Q_{\text{lb}}$ ) are here defined in terms of the Q-factor of a half wavelength patch ( $Q_{\text{hw}}$ ) with dielectric losses as

$$Q_{\text{lb}} = \frac{Q_{\text{hw}}}{\eta(1 + \Delta_{\text{sw}})}. \quad (24)$$

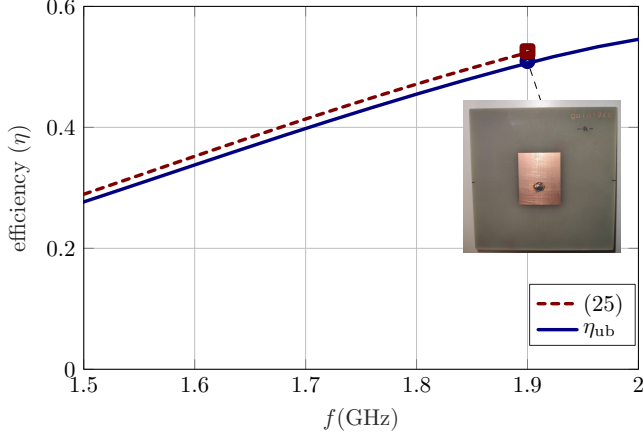


Figure 11: Upper bounds on radiation efficiency determined using current optimization (12) are compared to an approximation of the bounds from the Q-factor (25). The Q-factor comes from a measured half-wavelength microstrip patch antenna with relative permittivity  $\epsilon_r = 4.29(1 - j0.015)$ , substrate thickness  $h = 3.3$  mm, design region dimensions  $\ell_x \ell_y = 36.17 \times 28.88 \text{ mm}^2$  and the ground plane has dimensions  $100 \text{ mm} \times 100 \text{ mm}$ .

Substituting this into the expression relating efficiency to Q-factor (23) leads to an approximation of maximum radiation efficiency in terms of the lower Q-factor bound for a patch antenna on a lossless substrate as

$$\eta_{ub} \approx \frac{1}{(Q_{lb} \tan \delta + 1)(\Delta_{sw} + 1)}. \quad (25)$$

The lower Q-factor bounds in this expression can be determined from results presented in [10] by comparing the result with the maximum radiation efficiency obtained from (12).

The steps required to approximate radiation efficiency bounds from the Q-factor of a single half-wavelength patch antenna assuming negligible Ohmic losses are outlined in Appendix E. This can be useful as the Q-factor can be determined from measurements and simulations. The results, as shown in Figure 11, indicate that lower Q-factor bounds of a microstrip patch antenna are a good approximation of maximum achievable radiation efficiency when dielectric losses are added. Further, applying a scaling rule, the measured results can be used to approximate the maximum achievable radiation efficiency for miniaturized designs as shown by the dashed line in Figure 11.

In [3], the Q-factor is linked to Ohmic losses of half wavelength microstrip patch antennas by using the cavity model approximation. This can be used to write a similar expression to (25) for only Ohmic losses by replacing  $\tan \delta$  in (25)

with  $2R_s/(khZ_0)$ . This assumes Ohmic losses on both the ground plane and patch. The assumption made here of only Ohmic losses on the patch region can be made by replacing with  $R_s/(khZ_0)$  instead. This expression is expected to be less accurate than (25) as the stored energy is less clearly linked to Ohmic losses in a general setting.

## VII. VERTICAL CURRENTS

In this paper, the bounds constraints do not consider vertical currents between the ground plane and the dielectric substrate. However, it is worth noting an interesting miniaturization approach, consisting of using a shorting pin/wall to miniaturize the patch [12]. This avoids having to reshape the rectangular metal design region into for instance an H-shaped patch (see Figure 2c) but requires the addition of vias, leading to planar inverted-F antenna (PIFA) designs. These antennas can be simulated in commercial software using a shorting wall, as shown in Figure 12, demonstrating significantly higher radiation efficiency compared to the self-resonant bounds. To better understand the reason for this discrepancy, the self-resonant constraint is removed (10), demonstrating significantly higher radiation efficiency compared to the self-resonant bounds below half a wavelength. This leads to bounds performance similar to the PIFA radiation efficiency, suggesting that PIFA antennas essentially make the optimal Ohmic loss patch currents self-resonant. It should be noted that the PIFA also performs better than the self-resonant dielectric loss bounds. However, when the self-resonant constraint is removed, highly inductive loop currents that do not radiate in the normal direction and produce high Ohmic losses, lead to significantly higher radiation efficiency bounds.

## VIII. CONCLUSION

This paper investigates the performance limitations of microstrip patch antennas by presenting radiation efficiency and gain bounds. These bounds provide a realistic benchmark for assessing the feasibility and evaluating trade-offs involved in antenna design. Through a comprehensive study, the close alignment of these theoretical bounds with practical designs is demonstrated, highlighting their practical relevance. This closeness has been challenging to achieve on previous formulations of radiation efficiency bounds, especially for miniaturized designs [20]. The paper also presents a relationship between maximum bandwidth and maximum radiation efficiency, which could be very useful in the design process.

The following key findings summarize the contributions of this work:

- The radiation efficiency and gain bounds presented in this paper are shown to be close to the practical microstrip patch antenna design's performance.

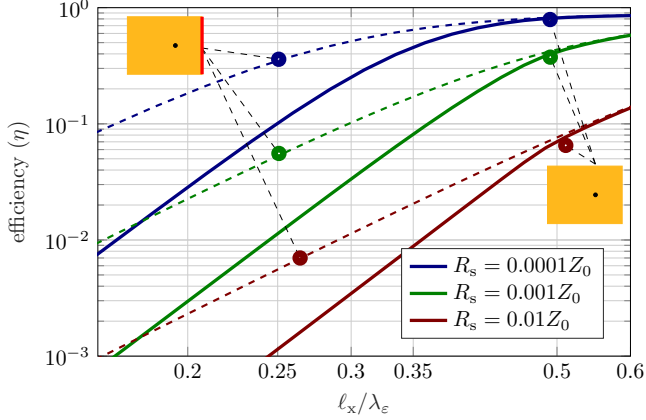


Figure 12: Upper bounds on radiation efficiency compared with (11) (solid) and without (10) (dashed) self-resonant constraint. The bounds are given for varying surface resistivities. Along with the performance of half-wavelength patch antennas, some PIFAs' radiation efficiency is also shown. The side of the PIFAs shorted to the ground is indicated with red. The design region dimensions are  $\ell_y = 0.77\ell_x$ , the substrate thickness is  $h = 0.05\ell_x$  and relative permittivity is  $\epsilon_r = 4$ .

This emphasizes the usefulness of these bounds as they serve as a realistic benchmark to assess feasibility and evaluate trade-offs.

- The bounds highlight the performance trade-offs linked to patch miniaturization, indicating that utilizing a higher permittivity substrate is often more beneficial than reshaping the patch design region for miniaturization
- Since the formulation for obtaining the bounds is not currently available in commercial solvers, an approximation is derived using the performance of a single half-wavelength patch antenna. This allows the antenna design community to utilize the bounds when considering the miniaturization of microstrip patch antennas.
- The bounds are further used to present an approximate relationship between maximum bandwidth (minimum Q-factor) and maximum radiation efficiency. This new finding suggests that in many instances, optimizing one of these parameters also implicitly optimizes the other.

This study makes significant advancements in understanding the performance limits of microstrip patch antennas. By establishing these bounds, a valuable tool for antenna designers is provided to benchmark their designs against the theoretical limits. The close agreement between the bounds and practical designs underscores their relevance and utility. However, future research should focus on

addressing the remaining open questions, including the effects of finite ground planes and the inclusion of vertical currents in the bounds formulation. These investigations will further refine the bounds and extend their applicability, ultimately aiding in the development of more efficient and effective antenna designs.

## ACKNOWLEDGMENT

We thank Hannes Bartle and Dr. Ismael Triviño from EPFL for helping with the measurements.

## APPENDIX A NOTATION USED

In Table I, a summary of the notation used in the paper is provided.

TABLE I: Definitions of Frequently Used Parameters in the paper

Parameter	Definition	Eqn/Fig
$\eta$	Radiation efficiency	(1)
$G$	Gain	(1)
$P_r$	Radiated power	(1)
$P_d$	Dissipated power	(1)
$P_\Omega$	Ohmic losses	(2)
$P_\varepsilon$	Dielectric losses	(2)
$\Omega$	Design region	(3)
$h$	Substrate thickness	Figure 1
$\varepsilon_r$	Relative permittivity	Figure 1
$\mathbf{J}(\mathbf{r})$	Current density	(3)
$\mathbf{I}$	patch currents	(4)
$\mathbf{Z}$	MoM impedance matrix	(4)
$\mathbf{R}$	Resistance matrix	(5)
$\mathbf{X}$	Reactance matrix	(5)
$\mathbf{F}_s$	Far-field matrix	(7)
$\mathbf{R}_r$	Radiation resistance	(9)

## APPENDIX B FAR FIELD EXPRESSIONS

The current density  $\mathbf{J}(\mathbf{r})$  in (3) in the design region is related to the radiated power by integration of the radiation intensity. Linked to the radiation intensity is the far field,  $\mathbf{F} = F_\theta \hat{\boldsymbol{\theta}} + F_\phi \hat{\boldsymbol{\phi}}$ , that is defined in terms of the electric field ( $re^{jkr} \mathbf{E}$ ) by letting the radial distance  $r \rightarrow \infty$  using spherical coordinates, where the elevation angle is given by  $\theta \in [0, \pi/2)$  and the azimuthal angle is given by  $\phi \in [0, 2\pi]$ , with the coordinate system shown in Figure 1.

The far-field contribution from an  $\hat{\mathbf{x}}$ -directed HED with dipole moment  $J_h$  (having units Am) is [18]

$$\begin{aligned} F_\theta &= \frac{Z_0}{2\pi} \frac{-J_h j k n_\theta \cos \phi \cos \theta}{n_\theta - j \varepsilon_r \cos \theta \cot(k h n_\theta)} \\ F_\phi &= \frac{Z_0}{2\pi} \frac{J_h j k \sin \phi \cos \theta}{\cos \theta - j n_\theta \cot(k h n_\theta)}, \end{aligned} \quad (26)$$

where  $Z_0$  is the free space impedance and  $n_\theta = \sqrt{\varepsilon_r - \sin^2 \theta}$ . A simple coordinate rotation can be used to calculate the far field from a  $\hat{\mathbf{y}}$ -directed HED. It should be noted that (26) was derived for a lossless dielectric substrate [18] and is here extended to the case of lossy substrates. These expressions can be shown to also be valid for lossy dielectric substrates and can alternatively be derived using reciprocity [30].

## APPENDIX C OPTIMIZATION FORMULATION

The upper bound on efficiency is determined by multiplying the second constraint in the QCQP (11) with a scalar parameter  $\nu$  and adding the two constraints  $\mathbf{I}^H \nu \mathbf{X} \mathbf{I} = 0$  and  $\mathbf{I}^H \mathbf{R} \mathbf{I} = 2P_{\text{in}}$  which yields

$$\begin{aligned} \min_{\nu} \max_{\mathbf{I}} \quad & \mathbf{I}^H \mathbf{R}_r \mathbf{I} \\ \text{subject to} \quad & \mathbf{I}^H (\mathbf{R} + \nu \mathbf{X}) \mathbf{I} = 2P_{\text{in}}. \end{aligned} \quad (27)$$

This problem is in the form of a Rayleigh quotient [7] and solved as a parametrized eigenvalue problem

$$\eta_{\text{ub}} = \min_{\nu} \max_{\mathbf{I}} \text{eig}(\mathbf{R}_r, \mathbf{R} + \nu \mathbf{X}), \quad (28)$$

where, given the condition  $\mathbf{R} + \nu \mathbf{X} \succeq \mathbf{0}$  and an indefinite  $\mathbf{X}$ , the scalar parameter is restricted to the range

$$\frac{-1}{\max \xi_a} \leq \nu \leq \frac{-1}{\min \xi_a}, \quad (29)$$

where  $\xi_a = \text{eig}(\mathbf{X}, \mathbf{R})$ , resembles characteristic modes [31]. The far-field matrix  $\mathbf{F}_s$  (9) is used to rewrite (27) as an ordinary eigenvalue problem given by (12).

The upper bound on gain based on solving (14) may present some challenges in recovering the optimal currents from the eigenvectors to test for no dual gap or calculation of the directivity. To avoid this, the first constraint in (13) can be added to the objective and then rewritten as an eigenvalue problem similar to (28). It should be noted that, for all optimization problems presented here, the problem can be reformulated to only search for solutions with radiating currents to improve numerical stability. Further, using semidefinite programming (SDP) the bounds can be computed in an alternative way [21].

## APPENDIX D

### Q-FACTOR

Q-factor can be approximated from the fractional bandwidth  $B_{\Gamma_0}$  in the case of a single resonance as [28]

$$Q \approx \frac{2}{B_{\Gamma_0}} \frac{\Gamma_0}{\sqrt{1 - \Gamma_0^2}}, \quad (30)$$

where  $\Gamma_0$  is the chosen reflection coefficient threshold. The frequency derivative of the input impedance can also be used to approximate the Q-factor as [28]

$$Q \approx \frac{\sqrt{(\omega R'_{\text{in}})^2 + (\omega X'_{\text{in}} + |X_{\text{in}}|)^2}}{2R_{\text{in}}}, \quad (31)$$

where the angular frequency derivative is given by  $'$  and  $R_{\text{in}}$  and  $X_{\text{in}}$  are the real and imaginary parts of the input impedance, respectively.

## APPENDIX E

### RELATION BETWEEN Q-FACTOR AND RADIATION EFFICIENCY

This appendix outlines the steps to go from the Q-factor of a lossy substrate to an approximation of the maximum radiation efficiency of a miniaturized design region and provides a practical example. Here the Q-factor is obtained from a half-wavelength patch measurement, however, a simulation could also have been used. Since the dielectric losses are relatively high using an FR4 substrate, the Ohmic losses are ignored when going from Q-factor to radiation efficiency in the following example.

To illustrate the practical use of the expressions in section VI on how to use the Q-factor of a half wavelength patch antenna to approximate the maximum achievable radiation efficiency for a miniaturized design region, the following steps are used:

- 1) Measure Q-factor of half wavelength patch *e.g.*, from bandwidth (30) or impedance (31) [28]
- 2) Approximate the ratio of surface wave power to radiated power using (16)
- 3) Determine the approximate radiation efficiency using (23)
- 4) Determine the approximate lossless substrate Q-factor using  $Q_{\text{lb}} = Q/(1 - Q \tan \delta)$
- 5) Scale the Q-factor [10]
- 6) Compute new approximate surface wave to radiated power ratio using (16)
- 7) Convert scaled Q-factor to approximate radiation efficiency bounds using (25)

As a practical example, using the half wavelength patch in Figure 11, resonant at 1.9 GHz these steps can be demonstrated. This design region has dimensions

$\ell_x = 36.17$  mm ( $\ell_x/\lambda_\varepsilon = 0.476$ ),  $\ell_y = 28.88$  mm and  $h = 3.3$  mm. The substrate relative permittivity is  $\varepsilon_r = 4.29(1 - j0.015)$ . For step 1, the Q-factor of this patch antenna is determined from its fractional bandwidth to be  $Q_{\text{hw}} = 25.4$  (approximately the same value can be obtained from the input impedance frequency derivative). Then step 2 the surface wave power to radiated power ratio is determined from (16) to be  $\Delta_{\text{sw}} = 0.178$ . Using the first two steps, in step 3 the approximate radiation efficiency of the half wavelength patch is calculated from (23). The resulting approximate efficiency is  $\eta \approx 0.526$ . This radiation efficiency approximation is added to the bounds shown in Figure 11 and shows a near-optimal value compared to the bounds. Then step 4 is to approximately convert the Q-factor with dielectric losses removed. This leads to  $Q_{\text{lb}} = 41$ . It may be of interest to assess what the expected approximate maximum radiation efficiency will be miniaturizing to 1.5 GHz with the same design parameters. Then in step 5, scaling the Q-factor to this frequency, the approximate lower bounds are  $Q_{\text{lb}} \approx 135.4$ . Now, the approximate surface wave to radiated power is calculated in step 6 as  $\Delta_{\text{sw}} = 0.14$ . Finally in step 7, the approximate achievable radiation efficiency at 1.5 GHz is  $\eta \approx 0.29$ . The approximated bounds between these two points are approximated by a dashed line.

#### REFERENCES

- [1] D. M. Pozar, "Microstrip antenna," *Proc. IEEE*, vol. 80, no. 1, pp. 79–91, 1992.
- [2] R. Garg, P. Bhartia, I. Bahl, and A. Ittipiboon, *Microstrip Antenna Design Handbook*. Artech House, 2001.
- [3] J. R. James and P. S. Hall, *Handbook of microstrip antennas*. Peregrinus on behalf of the Institution of Electrical Engineers London, U.K, 1989.
- [4] (2022) FEKO. Altair. [Online]. Available: <https://altairhyperworks.com/product/Feko>
- [5] (2022) CST Studio Suite 3D EM simulation and analysis software. [Online]. Available: <https://www.cst.com/>
- [6] R. F. Harrington, "Effect of antenna size on gain, bandwidth and efficiency," *Journal of Research of the National Bureau of Standards – D. Radio Propagation*, vol. 64D, pp. 1–12, January – February 1960.
- [7] M. Gustafsson, M. Capek, and K. Schab, "Tradeoff between antenna efficiency and Q-factor," *IEEE Trans. Antennas Propag.*, vol. 67, no. 4, pp. 2482–2493, April 2019.
- [8] L. Jelinek and M. Capek, "Optimal currents on arbitrarily shaped surfaces," *IEEE Trans. Antennas Propag.*, vol. 65, no. 1, pp. 329–341, 2017.
- [9] M. Gustafsson and S. Nordebo, "Optimal antenna currents for Q, superdirectivity, and radiation patterns using convex optimization," *IEEE Trans. Antennas Propag.*, vol. 61, no. 3, pp. 1109–1118, 2013.

- [10] B. A. P. Nel, A. K. Skrivervik, and M. Gustafsson, "Q-factor bounds for microstrip patch antennas," *IEEE Trans. Antennas Propag.*, vol. 71, no. 4, pp. 3430–3440, 2023.
- [11] D. Tayli and M. Gustafsson, "Physical bounds for antennas above a ground plane," *IEEE Antennas Wireless Propag. Lett.*, vol. 15, pp. 1281–1284, 2016.
- [12] A. K. Skrivervik, J.-F. Zürcher, O. Staub, and J. R. Mosig, "PCS antenna design: The challenge of miniaturization," *IEEE Antennas Propag. Mag.*, vol. 43, no. 4, pp. 12–27, Aug. 2001.
- [13] K. Fujimoto, A. Henderson, K. Hirasawa, and J. R. James, *Small Antennas*, ser. Antenna Series. Letchworth, England: Research Studies Press, 1988.
- [14] K.-F. Lee and K.-F. Tong, "Microstrip patch antennas—basic characteristics and some recent advances," *Proc. IEEE*, vol. 100, no. 7, pp. 2169–2180, 2012.
- [15] Z. Shao and Y. Zhang, "A single-layer miniaturized patch antenna based on coupled microstrips," *IEEE Antennas Wirel. Propag. Lett.*, vol. 20, no. 5, pp. 823–827, 2021.
- [16] H. Mosallaei and K. Sarabandi, "Antenna miniaturization and bandwidth enhancement using a reactive impedance substrate," *IEEE Trans. Antennas Propag.*, vol. 52, no. 9, pp. 2403–2414, 2004.
- [17] J. R. James, P. S. Hall, and C. Wood, *Microstrip antenna : theory and design*. Peregrinus on behalf of the Institution of Electrical Engineers London ; New York, 1981.
- [18] J. R. Mosig and F. E. Gardiol, "A dynamical radiation model for microstrip structures," in *Advances in Electronics and Electron Physics*, P. W. Hawkes, Ed. Academic Press, 1982, vol. 59, pp. 139 – 237.
- [19] R. F. Harrington, *Field Computation by Moment Methods*. New York, NY: Macmillan, 1968.
- [20] M. Gustafsson and M. Capek, "Maximum gain, effective area, and directivity," *IEEE Trans. Antennas Propag.*, vol. 67, no. 8, pp. 5282–5293, 2019.
- [21] S. P. Boyd and L. Vandenberghe, *Convex Optimization*. Cambridge Univ. Pr., 2004.
- [22] A. Beck and Y. C. Eldar, "Strong duality in nonconvex quadratic optimization with two quadratic constraints," *SIAM Journal on Optimization*, vol. 17, no. 3, pp. 844–860, 2006.
- [23] E. F. Knott, J. F. Shaeffer, and M. T. Tuley, *Radar Cross Section*. 5601 N. Hawthorne Way, Raleigh, NC 27613: SciTech Publishing Inc., 2004.
- [24] Y. Su, M. Pellaton, C. Affolderbach, G. Mileti, and A. K. Skrivervik, "Mode suppression and homogeneous field bandwidth enhancement of a tuning-free micro-loop-gap resonator using FR4 for chip-scale rubidium clock," *IEEE Trans. Microwave Theory Tech.*, pp. 1–11, 2024.
- [25] J. R. Mosig, R. C. Hall, and F. E. Gardiol, "Numerical analysis of microstrip patch antennas," in *Handbook of Microstrip Antennas*, J. R. James and P. S.

- Hall, Eds. London: Peregrinus, 1989, pp. 391–453.
- [26] J. R. Mosig, “Closed formula for the static three-dimensional Green function in microstrip structures,” *Electronics Letters*, vol. 14, pp. 544–546, 1978.
  - [27] B. A. P. Nel, A. K. Skrivervik, and M. Gustafsson, “Stored energies and Q-factor expressed in material derivatives,” *IEEE Antennas and Wireless Propagation Letters*, vol. 23, no. 1, pp. 19–23, 2024.
  - [28] A. D. Yaghjian and S. R. Best, “Impedance, bandwidth, and  $Q$  of antennas,” *IEEE Trans. Antennas Propag.*, vol. 53, no. 4, pp. 1298–1324, 2005.
  - [29] E. Newman, P. Bohley, and C. Walter, “Two methods for the measurement of antenna efficiency,” *IEEE Trans. Antennas Propag.*, vol. 23, no. 4, pp. 457–461, 1975.
  - [30] J. M. Jin, *Theory and Computation of Electromagnetic Fields*. Wiley, 2011.
  - [31] R. F. Harrington and J. R. Mautz, “Theory of characteristic modes for conducting bodies,” *IEEE Trans. Antennas Propag.*, vol. 19, no. 5, pp. 622–628, 1971.

## Paper III

## Paper III

*Reproduced, with permission, from: IEEE*

B. A. P. Nel, A. K. Skrivervik, and M. Gustafsson. Stored Energies and Q-factor expressed in Material derivatives. *IEEE Antennas and Wireless Propagation Letters*, 23(1), pp. 19–23, 2024. doi: 10.1109/LAWP.2023.3314859

# Stored Energies and Q-factor expressed in Material derivatives

Ben A. P. Nel, Anja K. Skrivervik, and Mats Gustafsson, *Senior Member, IEEE*

## Abstract

Stored energies of radiating systems have generated research interest for several decades due to their relationship with Q-factor and fractional bandwidth. In this paper material derivatives are used to provide a new interpretation of widely used stored energy expressions. This provides a fundamental relationship between stored energies of radiating systems and their electromagnetic material properties. It is shown that electric stored energy is related to the electric material parameter (permittivity) derivative. Similarly, magnetic stored energy is linked to the derivative of the permeability. Further, as an extension Cauchy-Riemann equations are used to relate stored energy to dissipation.

## Index Terms

Stored energy, reactive energy, dissipated energy, Q-factor, permittivity, permeability.

## I. INTRODUCTION

THE concept of stored electric and magnetic energy of radiating systems has interested researchers for several decades [1]. This interest comes mainly from the fact that stored energies are used to evaluate Q-factors, which provide good approximations of fractional bandwidths. Although much progress has been made in understanding stored energies, alternative methods of interpreting these quantities are still useful in providing further physical insight.

Corresponding author: Ben A.P. Nel.

This work was supported by the Swedish Research Council (2017-04656) and the Hedda Andersson guest professor program at Lund University.

Ben A.P. Nel and Mats Gustafsson are with the Department of Electrical and Information Technology, Lund University, SE-221 00 Lund, Sweden (e-mail: {ben.nel,mats.gustafsson}@eit.lth.se).

Anja K. Skrivervik is with the Microwave Antenna Group, École Polytechnique Fédérale de Lausanne (EPFL), 1015 Lausanne, Switzerland and the Department of Electrical and Information Technology, Lund University, SE-221 00 Lund, Sweden (e-mail: anja.skrivervik@epfl.ch).

Past research on stored energies and Q-factor of radiating systems include many approaches [1]. One classical technique is based on subtracting the far-field from the total energy [2], [3], [4]. Other approaches include taking frequency derivatives of the antenna input impedance [5], [6] and the method of moments (MoM) impedance matrix [7], [8], [9].

Linking electrostatic and magnetostatic energies to material perturbations is well established. Stratton [10, ch. II] notably proposed this nearly a century ago, see also [11, ch. II], [12, ch. VI]. He related a perturbation of the background permittivity and background permeability of a material to the changes in electrostatic and magnetostatic energies, respectively. This showed that, given constant charge, electrostatic energy is inversely proportional to the permittivity. Similarly, given constant current, magnetostatic energy is directly proportional to the permeability. Using material perturbations to interpret stored energies of radiating systems is more complex, emphasized by the fact that there is still no consensus on its definition [1].

The goal of this paper is to relate stored energies and Q-factors of radiating systems to changes in material parameters. To this end, stored energies are expressed in material derivatives by showing equality with energy expressions proposed by Harrington, Mautz, and Vandebosch [7], [8] based on frequency derivatives. This shows that electric stored energy is linked to a permittivity derivative and magnetic stored energy is linked to a permeability derivative. Once these relationships between stored energies and material derivatives are established, it follows from Cauchy–Riemann equations that there is a link to material losses. This is the first time that dissipated power has been used to express stored energies. Further, to demonstrate the versatility of the approach, material derivatives of antenna input impedance are related to their Q-factor.

Section II provides a background on stored energies of radiating systems and then section III derives identities between frequency and material derivatives of the Green’s function as well as the MoM impedance matrix. These identities are used in section IV to express stored energies with MoM matrices in terms of material derivatives. Further, section V presents antenna Q-factor in terms of material derivatives of input impedance. The paper is concluded in section VI. Finally, the appendices contain complementary information regarding the required mathematical derivations.

## II. BACKGROUND ON STORED ENERGIES AND Q-FACTOR

There have been several attempts over the years to compute stored electric and magnetic energies of antennas for time-harmonic fields in a homogeneous lossless background, see [1] for an overview. Currently, there is no consensus on a definition for stored energies of radiating systems [1]. However, useful methods

of approximating stored energies of electrically small antenna in free space are available [1].

One formulation isolates stored energy of a radiating system by subtracting the radiated energy density approximated by the far-field amplitude  $|\mathbf{F}|^2$  from the time-averaged total electromagnetic energy density [2], [6], [9] as

$$W_F = \frac{1}{4} \int_{\mathbb{R}^3} \varepsilon_0 |\mathbf{E}(\mathbf{r})|^2 + \mu_0 |\mathbf{H}(\mathbf{r})|^2 - 2\varepsilon_0 \frac{|\mathbf{F}|^2}{|\mathbf{r}|^2} dV, \quad (1)$$

where the electric and magnetic energy densities are given by  $\varepsilon_0 |\mathbf{E}|^2/4$  and  $\mu_0 |\mathbf{H}|^2/4$ , respectively, and  $\mathbf{r}$  denotes the position vector. The vacuum permittivity  $\varepsilon_0$  and permeability  $\mu_0$  in (1) can easily be generalized to a homogeneous background material. A flaw in (1) is that it is coordinate dependent and therefore not a proper definition of stored energies [6], [13]. Nevertheless, this is a good definition of stored energies of electrically small antennas [1].

Vandenbosch [7] proposed expressing the stored energy in the current density instead of fields. These expressions are equivalent to (1), except for a coordinate-dependent term [13, eq. 5]. In numerical calculations, the current density is expanded in basis functions and the stored energy is conveniently written using matrix notation producing quadratic forms proposed by Harrington and Mautz [8], where stored electric and magnetic energies are expressed as

$$W_e = \frac{1}{8} \mathbf{I}^H \left( \frac{\partial \mathbf{X}}{\partial \omega} - \frac{\mathbf{X}}{\omega} \right) \mathbf{I} \text{ and } W_m = \frac{1}{8} \mathbf{I}^H \left( \frac{\partial \mathbf{X}}{\partial \omega} + \frac{\mathbf{X}}{\omega} \right) \mathbf{I}, \quad (2)$$

respectively. Here,  $\mathbf{I}$  is a column matrix representing the current density  $\mathbf{J}(\mathbf{r})$ , the Hermitian transpose is denoted by superscript  $^H$ ,  $\mathbf{X}$  denotes the MoM reactance matrix, and the angular frequency is given by  $\omega$ .

Generally, practical interest into stored energies concerns the inverse relationship between fractional bandwidth and Q-factor that is defined as [6]

$$Q = \frac{2\omega \max\{W_e, W_m\}}{P_d}, \quad (3)$$

where dissipated power is given by  $P_d$ . While there is currently only indirect methods to measure Q-factor of an antenna such as the one in [6] that proposes to estimate the Q-factor, which for a self-resonant input impedance simplifies to

$$Q_{Z_{in}} = \frac{\omega}{2R_{in}} \left| \frac{\partial Z_{in}}{\partial \omega} \right| = \omega \left| \frac{\partial \Gamma}{\partial \omega} \right|, \quad (4)$$

where  $Z_{in}$  is the input impedance with real part given by  $R_{in}$  and  $\Gamma$  is the reflection coefficient for a matched load. This approach has been shown to generally agree well with Q-factor determined from frequency derivatives of the MoM reactance matrix (2), see [1].

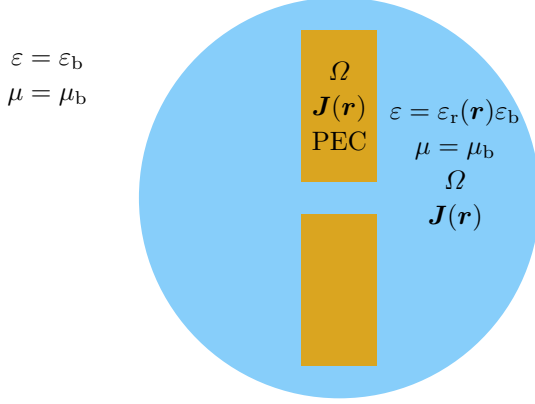


Figure 1: The background material with permittivity  $\varepsilon_b$  and permeability  $\mu_b$  encloses an antenna region  $\Omega$  with a PEC conducting region and a dielectric region with permittivity  $\varepsilon_r(\mathbf{r})\varepsilon_b$ . PEC regions have surface current densities and dielectric regions contrast currents densities both denoted  $\mathbf{J}(\mathbf{r})$ .

### III. MATERIAL PERTURBATIONS

Dyadic Green's functions are used to express the electromagnetic fields in terms of currents [14]. Therefore, this function can be used to relate the electromagnetic fields in expression (1) for stored electric and stored magnetic energies to source currents [13]. In this section angular frequency derivatives of the Green's function and MoM impedance matrix are transformed to permittivity and permeability derivatives. These expressions are used in the next section to provide an alternative interpretation of stored electric and magnetic energies derived from frequency derivatives of the MoM impedance matrix shown in (2).

To investigate the effect of material perturbations on an antenna structure, all material parameters are expressed in terms of the background material, serving as a reference point as shown in Figure 1. The permittivity and permeability of the background material are given by  $\varepsilon_b$  and  $\mu_b$ , respectively. The background material can be considered as vacuum, but here is allowed to be any nondispersive permittivity and permeability. A heterogeneous non-magnetic material distribution is expressed in terms of the background permittivity as  $\varepsilon = \varepsilon_r\varepsilon_b$ , where  $\varepsilon_r$  is a relative value allowing all dielectric parameters to be defined in terms of the background permittivity. Further, a PEC structure with surface current density may be confined withing a dielectric region having contrast current density.

The scalar Green's function (fundamental solution to the Helmholtz equation in a homogeneous background) has derivatives with respect to background material parameters  $\varepsilon_b, \mu_b$  and angular frequency  $\omega$  that can be equivalently

expressed as

$$\begin{aligned} \varepsilon_b \frac{\partial}{\partial \varepsilon_b} \frac{e^{-j\omega\sqrt{\varepsilon_b\mu_b}R}}{4\pi R} &= \mu_b \frac{\partial}{\partial \mu_b} \frac{e^{-j\omega\sqrt{\varepsilon_b\mu_b}R}}{4\pi R} \\ &= \frac{-j\omega\sqrt{\varepsilon_b\mu_b}}{2} \frac{e^{-j\omega\sqrt{\varepsilon_b\mu_b}R}}{4\pi} = \frac{\omega}{2} \frac{\partial}{\partial \omega} \frac{e^{-j\omega\sqrt{\varepsilon_b\mu_b}R}}{4\pi R}, \end{aligned} \quad (5)$$

where  $R$  is the distance between source and observer points and the time convention  $e^{j\omega t}$  is used. This expression shows that frequency and material perturbations of the scalar Green's function are interchangeable. This can be understood in the lossless case by the fact that both permittivity and permeability affect the velocity of the electromagnetic wave. The resulting decrease in wavelength when the frequency is increased and material kept constant is interchangeable with increasing permittivity or permeability and keeping frequency constant. However, the square root of permittivity and permeability accounts for the factor  $1/2$  in (5) when taking derivatives with respect to angular frequency of the scalar Green's function.

The dyadic Green's function (based on the scalar Green's function) in a homogeneous background material described by  $\varepsilon_b, \mu_b$  is [14]

$$\mathbf{G} = \left( \mathbf{1} + \frac{1}{\omega^2 \varepsilon_b \mu_b} \nabla \nabla \right) \frac{e^{-j\omega\sqrt{\varepsilon_b\mu_b}R}}{4\pi R}. \quad (6)$$

The same relationship (5) of material and frequency derivatives as for the scalar Green's function also hold for the dyadic Green's function

$$\varepsilon_b \frac{\partial \mathbf{G}}{\partial \varepsilon_b} = \mu_b \frac{\partial \mathbf{G}}{\partial \mu_b} = \frac{\omega}{2} \frac{\partial \mathbf{G}}{\partial \omega}. \quad (7)$$

To account for different material properties in the antenna region, volumetric MoM [15] is used. The MoM matrix can then be split into two parts

$$\mathbf{Z} = \mathbf{Z}_0 + \mathbf{Z}_\rho, \quad (8)$$

where  $\mathbf{Z}_0$  is the background term and the non-magnetic material part is given by  $\mathbf{Z}_\rho$  (described in Appendix A). The background term is evaluated using the dyadic Green's function (6) as

$$Z_{0,mn} = j\omega\mu_b \int_{\Omega} \int_{\Omega} \boldsymbol{\psi}_m(\mathbf{r}') \cdot \mathbf{G}(\mathbf{r}', \mathbf{r}) \cdot \boldsymbol{\psi}_n(\mathbf{r}) dV' dV, \quad (9)$$

where  $\boldsymbol{\psi}_m$  denotes the basis functions [16].

The MoM impedance matrix (8) is differentiated with respect to permittivity and permeability using (7) for  $\mathbf{Z}_0$  and Appendix A for  $\mathbf{Z}_\rho$  and then written as

$$\varepsilon_b \frac{\partial \mathbf{Z}}{\partial \varepsilon_b} = \frac{\omega}{2} \frac{\partial \mathbf{Z}}{\partial \omega} - \frac{\mathbf{Z}}{2} \quad \text{and} \quad \mu_b \frac{\partial \mathbf{Z}}{\partial \mu_b} = \frac{\omega}{2} \frac{\partial \mathbf{Z}}{\partial \omega} + \frac{\mathbf{Z}}{2}, \quad (10)$$

in terms of angular frequency derivatives.

The background material may be lossy and therefore have complex valued permittivity and permeability. Using holomorphic properties of  $\mathbf{Z}$  for passive material models leads to Cauchy–Riemann equations [5], [17], [18]

$$\frac{\partial \mathbf{X}}{\partial \operatorname{Re} \varepsilon_b} = -\frac{\partial \mathbf{R}}{\partial \operatorname{Im} \varepsilon_b} \quad \text{and} \quad \frac{\partial \mathbf{X}}{\partial \operatorname{Re} \mu_b} = -\frac{\partial \mathbf{R}}{\partial \operatorname{Im} \mu_b}, \quad (11)$$

where only one of the Cauchy–Riemann equations is used. The other containing *e.g.*,  $\partial \mathbf{X} / \partial \operatorname{Im} \varepsilon_b = \partial \mathbf{R} / \partial \operatorname{Re} \varepsilon_b$ , is less clearly linked to stored energy. The Cauchy–Riemann equation (11) demonstrates that the reactance matrix ( $\mathbf{X}$ ), when differentiated with respect to real material parameters, can be expressed in terms of the resistance matrix ( $\mathbf{R}$ ) differentiated with respect to material losses. These matrices are defined in terms of the MoM impedance matrix as

$$\mathbf{X} = \frac{\mathbf{Z} - \mathbf{Z}^H}{2j} \quad \text{and} \quad \mathbf{R} = \frac{\mathbf{Z} + \mathbf{Z}^H}{2}, \quad (12)$$

where the reactance matrix ( $\mathbf{X}$ ), also used in (2), is the imaginary part of the MoM impedance matrix and relates currents to the difference between magnetic and electric energies. The resistance matrix ( $\mathbf{R}$ ) relates currents to radiated power and dissipated power in the material.

#### IV. STORED ENERGIES

In this section, it is shown that stored energies derived from frequency derivatives of the MoM impedance matrix (2) can equivalently be expressed in terms of material derivatives of the MoM impedance matrix. For these expressions the limit of no background material losses are assumed. This new relationship of stored electric energy is summarized in the diagram shown in Figure 2.

This relationship identifies that the effect on the MoM impedance matrix of differentiating with respect to permittivity (10) is, besides a scaling factor, identical to the matrix multiplied with the current vector in (2), where stored electric energy is computed from frequency derivatives of the MoM reactance matrix. This leads to an expression for stored electric energy as a derivative of the reactance matrix with respect to the background permittivity. Similarly, the relationship between stored magnetic energy (2) and a derivative with respect to the background permeability can be obtained through the MoM impedance matrix differentiated with respect to the background permeability (10) and Cauchy–Riemann equation (11), in the limit of no background material losses, *i.e.*,  $\operatorname{Im} \varepsilon_b \rightarrow 0$  and  $\operatorname{Im} \mu_b \rightarrow 0$ , the derivatives can be applied to the reactance matrix (12) as

$$W_e = \frac{\varepsilon_b}{4\omega} \mathbf{I}^H \frac{\partial \mathbf{X}}{\partial \operatorname{Re} \varepsilon_b} \mathbf{I} \quad \text{and} \quad W_m = \frac{\mu_b}{4\omega} \mathbf{I}^H \frac{\partial \mathbf{X}}{\partial \operatorname{Re} \mu_b} \mathbf{I}. \quad (13)$$

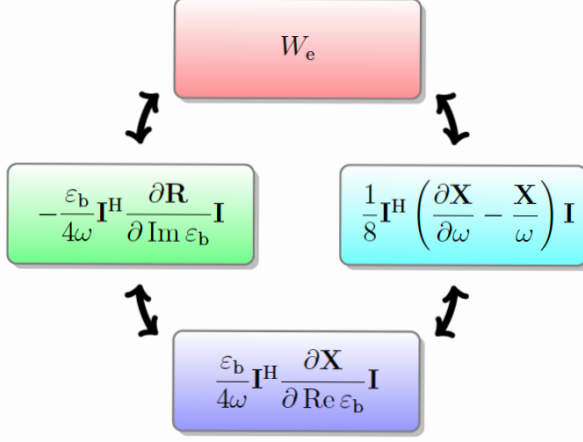


Figure 2: Stored electric energy in the limit of no background material losses expressed in terms of derivatives, with respect to frequency, permittivity, and dielectric losses.

The expressions in (13) show that the MoM reactance matrix's derivatives with respect to the electric material parameter namely permittivity and the magnetic material parameter namely permeability leads to equivalent expressions for stored energies as ones based on taking frequency derivatives (2).

Additionally these expressions show for the first time that electric stored energy depends on the reactance sensitivity to electric material changes. Similarly, the magnetic stored energy depends on the reactance sensitivity to magnetic material changes. This is related to the accepted relation between electric energy and permittivity in electrostatics and magnetic energy and permeability in magnetostatics [10], [11]. However, in the case where there is a radiated field, stored electric energy and stored magnetic energy (13) are both functions of permittivity and permeability leading to a complex relationship between these parameters.

The expressions for stored energies from material derivatives (13) can further be reformulated using the Cauchy–Riemann equation (11), in the limit of no background material losses. These equations express stored electric and magnetic energies (13) as

$$W_e = \frac{-\varepsilon_b}{4\omega} \mathbf{I}^H \frac{\partial \mathbf{R}}{\partial \text{Im } \varepsilon_b} \mathbf{I} \text{ and } W_m = \frac{-\mu_b}{4\omega} \mathbf{I}^H \frac{\partial \mathbf{R}}{\partial \text{Im } \mu_b} \mathbf{I}, \quad (14)$$

respectively. Equality between expressions in (14) and (13) lead to an interpretation of stored energies in terms of sensitivity (derivative) to background material losses of the resistance matrix. The negative sign in these expressions is

due to the choice of time convention. Here, it should be noted that material derivative expressions can be written equal to (2), not only in the lossless limit using complex derivatives (10) [19] leading to *e.g.*,  $W_e = \text{Im} \frac{\varepsilon_b}{4\omega} \mathbf{I}^H \frac{\partial \mathbf{Z}}{\partial \varepsilon_b} \mathbf{I} = \text{Re} \frac{\varepsilon_b}{2\omega} \mathbf{I}^H \frac{\partial \mathbf{X}}{\partial \varepsilon_b} \mathbf{I} = \text{Im} \frac{\varepsilon_b}{2\omega} \mathbf{I}^H \frac{\partial \mathbf{R}}{\partial \varepsilon_b} \mathbf{I}$ . Similar expressions for stored magnetic energy are obtained by replacing background permittivity with permeability. However, for lossy background material these expressions are difficult to interpret and may require another approach [20].

The resistance matrix (12) used to formulate stored energies in (14) is related to dissipated power of an antenna. This power can be split into power leaving a volume (*e.g.*, radiation) and power lost within the volume (*e.g.*, material losses). Stored energies are generally thought to only be related to changes in antenna reactance. However, in (14) it is shown that they also relate to changes in dissipated power. This is demonstrated by using Cauchy-Riemann equations (11) to express material derivatives of resistance and reactance in terms of one another.

When the derivatives with respect to material loss in (14) produce negative definite matrices as is the case for electrically small structures they are a reliable approximation of stored energies. For this case the dissipated power is increased by these material loss perturbations. However, it should be noted that for electrically large structures the expressions (14) can produce negative values [21]. One interpretation of this is that the reduction in power leaving a volume may exceed the increase in power lost within the volume when perturbing material losses.

## V. Q-FACTOR FROM INPUT IMPEDANCE

The material derivative identities of the MoM matrix (10) can be used to reinterpret the Q-factor from input impedance (4). By doing this, the versatility of material derivative approach is demonstrated.

The derivatives of the MoM matrix (10) are related to material derivatives of the input impedance  $Z_{\text{in}}$  shown in Appendix B leading to

$$\varepsilon_b \frac{\partial Z_{\text{in}}}{\partial \varepsilon_b} = \frac{\omega}{2} \frac{\partial Z_{\text{in}}}{\partial \omega} - \frac{Z_{\text{in}}}{2} \text{ and } \mu_b \frac{\partial Z_{\text{in}}}{\partial \mu_b} = \frac{\omega}{2} \frac{\partial Z_{\text{in}}}{\partial \omega} + \frac{Z_{\text{in}}}{2}. \quad (15)$$

Using these expressions valid for a lossy background material, Q-factor formulated with frequency derivatives of input impedance (4) can equivalently be expressed using (15) as

$$Q_{Z'_{\text{in}}} = \frac{1}{2R_{\text{in}}} \left| \varepsilon_b \frac{\partial Z_{\text{in}}}{\partial \varepsilon_b} + \mu_b \frac{\partial Z_{\text{in}}}{\partial \mu_b} \right|, \quad (16)$$

leading to an interpretation of Q-factor in terms of material sensitivity of the input impedance. It should be noted that in (16) self resonance is assumed.

## VI. CONCLUSION

In this paper a relationship between stored energies of radiating systems and material derivatives is investigated. From this investigation it is shown that widely used expressions to evaluate stored energies can be interpreted in terms of material derivatives. This leads to the fundamental relationship between stored electric energy and electric material properties namely permittivity. Similarly, stored magnetic energy is related to permeability. Further, the MoM resistance matrix is used to interpret stored energies for the first time. This demonstrates a new link between material losses and stored energies of radiating systems. Lastly, it is also shown that frequency derivatives used to compute Q-factor from input impedance can be replaced by material derivatives.

### APPENDIX A VOLUMETRIC MoM MATERIAL DERIVATIVES

The MoM material part (8) assuming only non-magnetic properties is given by

$$Z_{\rho, mn} = \int_{\Omega} \boldsymbol{\psi}_m(\mathbf{r}) \cdot \boldsymbol{\rho}(\mathbf{r}) \cdot \boldsymbol{\psi}_n(\mathbf{r}) dV, \quad (17)$$

where the complex resistivity is  $\rho = -j/(\omega\epsilon_b\chi_e)$  and where  $\chi_e$  is the electric susceptibility when the background permittivity is equal to vacuum. The derivative with respect to background permittivity of  $\mathbf{Z}_{\rho}$  can be expressed as

$$\epsilon_b \frac{\partial \mathbf{Z}_{\rho}}{\partial \epsilon_b} = \frac{\omega}{2} \frac{\partial \mathbf{Z}_{\rho}}{\partial \omega} - \frac{\mathbf{Z}_{\rho}}{2}, \quad (18)$$

since  $\partial \mathbf{Z}_{\rho} / \partial \omega = -\mathbf{Z}_{\rho} / \omega$ . Further, due to the assumption of non-magnetic media, the derivative with respect to background permeability is

$$\mu_b \frac{\partial \mathbf{Z}_{\rho}}{\partial \mu_b} = \frac{\omega}{2} \frac{\partial \mathbf{Z}_{\rho}}{\partial \omega} + \frac{\mathbf{Z}_{\rho}}{2} = \mathbf{0}. \quad (19)$$

### APPENDIX B MoM MATRIX RELATED TO INPUT IMPEDANCE

From the MoM impedance matrix (8), the admittance matrix is  $\mathbf{Y} = \mathbf{Z}^{-1}$  and is related to the input admittance as

$$Y_{\text{in}} = \frac{1}{Z_{\text{in}}} = \frac{\mathbf{V}^T \mathbf{Y} \mathbf{V}}{V_{\text{in}}^2}, \quad (20)$$

where  $Z_{\text{in}}$  is the input impedance. Assuming a frequency and material independent input voltage,  $V_{\text{in}}$ , frequency differentiation of the input admittance lead to

$$V_{\text{in}}^2 \frac{\partial Y_{\text{in}}}{\partial \omega} = \mathbf{V}^T \frac{\partial \mathbf{Y}}{\partial \omega} \mathbf{V} = -\mathbf{V}^T \mathbf{Z}^{-1} \frac{\partial \mathbf{Z}}{\partial \omega} \mathbf{Z}^{-1} \mathbf{V}. \quad (21)$$

Similarly the background permittivity derivative of the admittance matrix can be written as

$$\frac{\partial \mathbf{Y}}{\partial \varepsilon_b} = -\mathbf{Z}^{-1} \frac{\partial \mathbf{Z}}{\partial \varepsilon_b} \mathbf{Z}^{-1}. \quad (22)$$

Then, using the relation between derivative of background permittivity and frequency of the MoM matrix (10) (inverse of admittance matrix) this can be equivalently expressed in terms of a derivative with respect to the background permittivity as

$$\varepsilon_b \frac{\partial \mathbf{Y}}{\partial \varepsilon_b} = \frac{\omega}{2} \frac{\partial \mathbf{Y}}{\partial \omega} + \frac{\mathbf{Y}}{2}. \quad (23)$$

It follows from the relationship between frequency derivatives of the input admittance and admittance matrix (21) that

$$\varepsilon_b \frac{\partial Y_{\text{in}}}{\partial \varepsilon_b} = \frac{\omega}{2} \frac{\partial Y_{\text{in}}}{\partial \omega} + \frac{Y_{\text{in}}}{2}, \quad (24)$$

this leads to

$$\varepsilon_b \frac{-\frac{\partial Z_{\text{in}}}{\partial \varepsilon_b}}{Z_{\text{in}}^2} = \frac{\omega}{2} \frac{-\frac{\partial Z_{\text{in}}}{\partial \omega}}{Z_{\text{in}}^2} + \frac{1}{2Z_{\text{in}}}, \quad (25)$$

and can be rewritten as the left-hand side of (15). Similarly, differentiation with respect to background permeability can be shown to lead to the right-hand side of (15).

## REFERENCES

- [1] K. Schab, L. Jelinek, M. Capek, C. Ehrenborg, D. Tayli, G. A. Vandenbosch, and M. Gustafsson, "Energy stored by radiating systems," *IEEE Access*, vol. 6, pp. 10 553 – 10 568, 2018.
- [2] R. L. Fante, "Quality factor of general ideal antennas," *IEEE Trans. Antennas Propag.*, vol. 17, no. 2, pp. 151–155, Mar. 1969.
- [3] C. Levis, "A reactance theorem for antennas," *Proceedings of the IRE*, vol. 45, no. 8, pp. 1128–1134, 1957.
- [4] D. R. Rhodes, "Observable stored energies of electromagnetic systems," *Journal of the Franklin Institute*, vol. 302, no. 3, pp. 225–237, 1976.
- [5] D. Rhodes, "A reactance theorem," *Proc. R. Soc. A*, vol. 353, no. 1672, pp. 1–10, 1977.
- [6] A. D. Yaghjian and S. R. Best, "Impedance, bandwidth, and  $Q$  of antennas," *IEEE Trans. Antennas Propag.*, vol. 53, no. 4, pp. 1298–1324, 2005.
- [7] G. A. E. Vandenbosch, "Reactive energies, impedance, and  $Q$  factor of radiating structures," *IEEE Trans. Antennas Propag.*, vol. 58, no. 4, pp. 1112–1127, 2010.
- [8] R. F. Harrington and J. R. Mautz, "Control of radar scattering by reactive loading," *IEEE Trans. Antennas Propag.*, vol. 20, no. 4, pp. 446–454, 1972.

- [9] M. Gustafsson and B. L. G. Jonsson, “Stored electromagnetic energy and antenna Q,” *Progress In Electromagnetics Research (PIER)*, vol. 150, pp. 13–27, 2015.
- [10] J. A. Stratton, *Electromagnetic Theory*. New York, NY: McGraw-Hill, 1941.
- [11] L. D. Landau and E. M. Lifshitz, *Electrodynamics of Continuous Media*, 1st ed. Oxford: Pergamon Press, 1960.
- [12] W. K. Panofsky and M. Phillips, *Classical Electricity and Magnetism*, 2nd ed. Reading, MA: Addison-Wesley, 1962.
- [13] M. Gustafsson and B. L. G. Jonsson, “Antenna Q and stored energy expressed in the fields, currents, and input impedance,” *IEEE Trans. Antennas Propag.*, vol. 63, no. 1, pp. 240–249, 2015.
- [14] G. Kristensson, *Scattering of Electromagnetic Waves by Obstacles*. Edison, NJ: SciTech Publishing, an imprint of the IET, 2016.
- [15] J. M. Jin, *Theory and Computation of Electromagnetic Fields*. Wiley Online Library, 2010.
- [16] R. F. Harrington, *Field Computation by Moment Methods*. New York, NY: Macmillan, 1968.
- [17] R. E. Greene and S. G. Krantz, *Function Theory of One Complex Variable*, 3rd ed. Providence, RI: American Mathematical Society, 2006.
- [18] W. Geyi, “Stored energies and radiation Q,” *IEEE Trans. Antennas Propag.*, vol. 63, no. 2, pp. 636–645, 2015.
- [19] W. Wirtinger, “Zur formalen Theorie der Funktionen von mehr komplexen Veränderlichen,” *Mathematische Annalen*, vol. 97, pp. 357–376, 1927.
- [20] M. Gustafsson and C. Ehrenborg, “State-space models and stored electromagnetic energy for antennas in dispersive and heterogeneous media,” *Radio Sci.*, vol. 52, 2017.
- [21] M. Gustafsson, M. Cismasu, and B. L. G. Jonsson, “Physical bounds and optimal currents on antennas,” *IEEE Trans. Antennas Propag.*, vol. 60, no. 6, pp. 2672–2681, 2012.



## **Paper IV**

## Paper IV

*Accepted*

B. A. P. Nel, A. K. Skrivervik, J. Lundgren, and M. Gustafsson. Impact of Metasurface Element Designs on Infrared-Based Antenna Near-Field Measurements. Accepted. In Proceedings of the 19th European Conference on Antennas and Propagation (EuCAP), 2025, Accepted.

# Impact of Metasurface Element Designs on Infrared-Based Antenna Near-Field Measurements

Ben A.P. Nel\*, Anja K. Skrivervik<sup>†</sup>\*, Johan Lundgren\*, Mats Gustafsson\*

\*Lund University, Lund, Sweden, ben.nel@eit.lth.se <sup>†</sup>Ecole Polytechnique Fédérale de Lausanne, Lausanne, Switzerland, anja.skrivervik@epfl.ch

## Abstract

The measurement of electromagnetic fields near a radiating device is often required in compliance testing. In this paper, the measurement of placing the radiating device near a metasurface designed to induce heat from radio frequency fields is considered. This heat distribution on the surface can be imaged with an infrared camera. A metasurface is placed between the infrared camera and the device in this measurement setup. The metasurface design is essential as it must respond to the source field in a way that is interpretable by the infrared camera. Thus three possible metasurface designs are examined. The sensitivity of these metasurface designs to two orthogonal linear polarizations is investigated. Further, the power dissipated on the metasurface and how it compares to the field from the source is studied. The paper finds that the metasurface element's dissipated power correlates better with the incident power density than with the electric energy density.

## Index Terms

Metasurface, near-field imaging, IR radiation

## I. INTRODUCTION

The near field from a device *e.g.*, a mobile phone, can be imaged using a metasurface and an infrared (IR) camera [1]. This method utilizes the relationship between heat (proportional to dissipated power) and the generation of IR photons. Here the metasurface serves as a tool for up-converting the radiated radio frequency (RF) field from the device into IR radiation that is detected by the camera. When analyzing this conversion, the metasurface design can present many trade-offs such as between absorbed power and reflected power.

Corresponding author: Ben A.P. Nel.

This work was supported by Excellence Center at Linköping – Lund in Information Technology (ELLIIT) and the Hedda Andersson guest professor program at Lund University.

IR cameras have been used in indirect measurements of RF fields for a few decades [2], [3], [4], [5], [6], [7]. However, this was initially done with a homogeneous sheet. More recently it has been proposed to use a metasurface designed to dissipate power from mmWaves using sub-wavelength elements. This method also uses thermal imaging with an IR camera to observe the increase in IR photons released due to the heat on localized metasurface elements [1] rather than the whole homogeneous sheet. An advantage of using metasurface elements over a homogeneous sheet is the ability to discriminate between two orthogonal polarizations. The metasurface technique has also been applied for defect detection in the radiating structure under test [8].

Metasurface sensors [9], [10] can be used in real-time and are less complex than some other measurement environments [1]. However, the metasurface elements may have a significant impact on the electromagnetic field that is being measured. First, the reflected power can interact with the source, and second, the metasurface elements can interact with one another (mutual coupling). Overcoming these challenges may be crucial to obtaining useful information from the dissipated power on the metasurface elements.

This paper investigates how the design of the metasurface elements affects the ability to convert the radiated RF field from the source (device) into dissipated power from Ohmic losses on the elements. Three different elements are considered, namely, dipole, U-shaped, and cross potent. The ability of these elements to absorb power, be frequency selective, and have polarization properties, is investigated. Further, the dissipated power in metasurface elements is compared numerically with the free space electric energy density, and incident power density from a radiating Herzian dipole (source), to better understand the imaging of field distributions.

The remainder of the paper is structured as follows. Section II provides background on the metasurface electromagnetic properties for the metasurfaces being used. Section III analyzes and provides a discussion on the performance of the metasurface. Then finally the paper has the conclusion and discussion in Section IV.

## II. METASURFACE ELECTROMAGNETIC PROPERTIES

An example of a metasurface placed between a source that radiates an electromagnetic field, and an IR camera that captures IR photons proportional to the temperature on the surface, is shown in Figure 1. The increase in temperature on the surface is proportional to the dissipated power due to Ohmic losses on the metasurface elements. This paper focuses on the source and metasurface part of this measurement setup. However, it is worth noting that the use of the IR camera places some design constraints on the metasurface, that are not considered. For

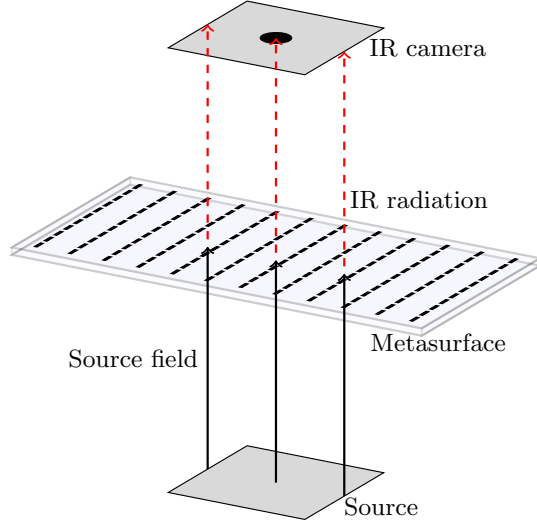


Figure 1: The measurement setup with the metasurface placed between the electromagnetic source and the IR camera.

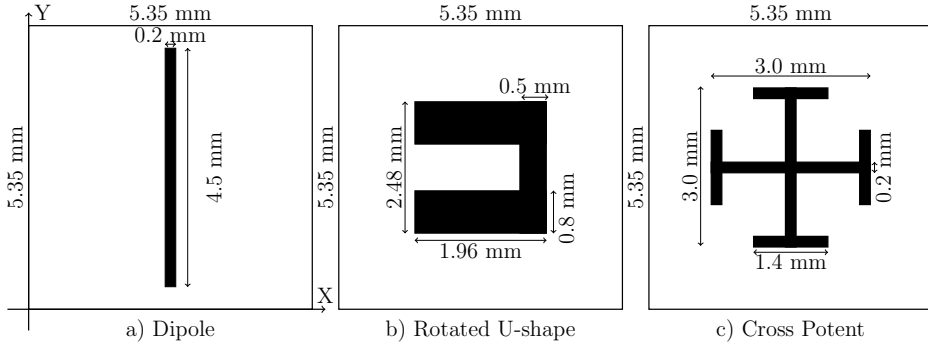


Figure 2: The three elements along with their dimensions. They are all confined within a unit cell of  $5.35 \times 5.35 \text{ mm}^2$ . The elements have three different surface resistivities,  $6.45 \text{ } \Omega/\square$  for the dipole,  $7.3 \text{ } \Omega/\square$  for the U-shape and  $10.3 \text{ } \Omega/\square$  for the cross potent.

instance, the dissipated power in the form of heat should be detectable, and the metasurface should have a low mass [1].

For the metasurface in Figure 1, a substrate, that is here electromagnetically characterized with a relative permittivity of 3.1, is used. The surface is electrically thin, with a thickness of 0.05 mm, thus it is not expected to greatly affect the electromagnetic behavior of the metasurface elements. The metasurface elements

are distributed on the IR camera side of the metasurface, as can be seen in Figure 1.

The goal of the metasurface is to extract part of the power from an electromagnetic field with a frequency located in the microwave or mm-wave bands. As an example, a frequency ( $f$ ) of 28 GHz (Ka-band) is selected, having a wavelength of approximately 10.7 mm, as is used in 5G communication [11]. Performance of the three metasurface elements shown in Figure 2 are compared. The elements are designed to maximize absorptance at around 28 GHz. The dimensions of these elements are shown and are confined within a square unit cell with a side length of around half-a-wavelength (5.35 mm).

When an incident plane wave, here considered to be linearly polarized, impinges on an infinite periodic metasurface, the metasurface performance can be analyzed by assessing the transmittance  $T$ , reflectance  $R$ , and absorptance  $A$ . For the purpose of this paper, the goal is to have as much absorbed power (related to absorptance) as possible while maintaining a low level of reflected power (related to reflectance), as this will interfere with the source and affect the measurement. Conservation of power relates these quantities as

$$R + A + T = 1. \quad (1)$$

The maximum absorptance for an infinitely thin sheet is 50%. For this case, the transmittance is 25% and the reflectance is also 25%. By adjusting the surface resistivity of the elements, the values of  $R, A, T$  in (1) can be altered [1]. Here, having an absorptance of approximately 44% is a trade-off to reduce the reflectance.

The three metasurface elements used are shown in Figure 2. Their transmittance, reflectance and absorptance for a y-polarized plane wave are simulated using FEKO [12] and are shown in Figure 3. As a starting point, the U-shaped presented in [8] is used. This element has a surface resistance of  $7.3 \text{ } \Omega/\square$  (ohms per square), the dipole  $10.3 \text{ } \Omega/\square$  and the cross potent  $6.45 \text{ } \Omega/\square$ . For these parameters, the performance is nearly identical at 28 GHz. However, all structures have variations in bandwidth [13] that can be seen by the difference in performance away from the center frequency.

While the results in Figure 3 suggest a similarity in performance between the elements, this is only for the y-polarized case and a plane wave. In the next section, the case of an x-polarized plane wave is used to assess the polarization purity of the elements. Along with this, an ideal source placed in the near field is assessed.

### III. ANALYSIS AND RESULTS

This section examines the ability of the metasurface elements to only dissipate power for one polarization (polarization purity) [14]. Further, how the antenna

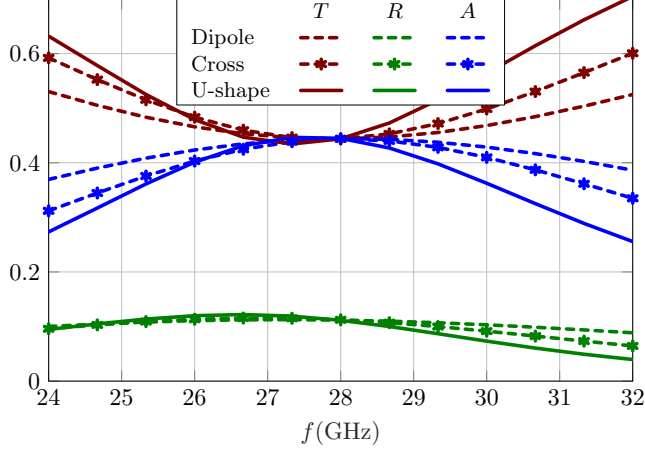


Figure 3: Transmittance, reflectance, and absorptance over a frequency range for the three antenna elements in Figure 2.

elements relate to measurable electromagnetic field properties, is also examined. The electromagnetic field properties chosen here are the electric energy density and incident power density. These field properties are first determined without the metasurface and then compared to the dissipated power on the metasurface elements.

#### A. Polarization purity

The ability of the metasurface element to discern between two polarizations may be desirable [14]. This performance is examined in Figure 4 where, from a plane wave, the absorptance on an element from a y-polarized wave and an x-polarized wave are compared. First, for the cross potent, the results are independent of polarization as expected from the element symmetry. In contrast, the dipole primarily dissipates power from a y-polarized plane wave. The U-shaped element, although it can be confined within the smallest circular region, has non-negligible x-polarized plane wave power dissipated on the element that can cause measurement ambiguity when interpreting results, especially away from the center frequency (28 GHz).

#### B. Near-field imaging

The goal of the metasurface is to image the field radiated by the device under test. To assess this ability for a specific metasurface element, the field distribution of an ideal electric dipole (source) is placed one wavelength below the metasurface (see Figure 1) and is y-polarized. First, the near field is assessed without the

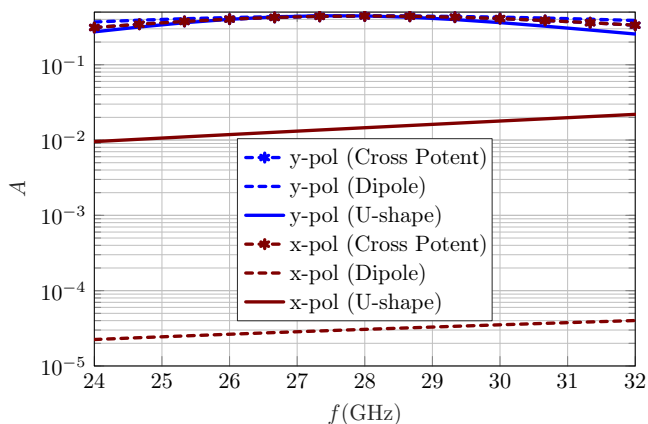


Figure 4: The absorptance for y-polarized and x-polarized plane wave impinging on a metamaterial sheet for the three elements in Figure 2.

metasurface. This is done, as shown in Figure 5, by examining the distribution of the normalized electric energy density, excluding the z-directed (normal) part of the field. The elements are sensitive to the electric field component of the energy density. For dipole and U-shaped elements, this is expected to be primarily for the y-polarized component. Therefore, this component of the electric field is examined, as shown in Figure 6. This distribution scales more rapidly in the y-direction, as much of the radial near field produced by the idealized electric dipole is not included. The incident power density is shown in Figure 7. This field distribution scales more rapidly in all directions from the center (peak).

A metasurface with  $11 \times 11$  dipole elements (see Figure 2a) illuminated by an ideal y-polarized dipole placed one wavelength below the center element of the surface is considered first. The normalized distribution of dissipated power in the dipole elements is shown in Figure 8. The presented data in the figure correctly shows that the field is the strongest in the center. When comparing the normalized values with the field distributions in Figure 5-7, it best resembles the scaling of the incident power density in Figure 7.

Absorbed power in the  $11 \times 11$  U-shaped and cross potent metasurface elements are shown in Figure 9 and Figure 10, respectively. These results also show a similar rapid scaling as observed for the incident power density in Figure 7.

#### IV. CONCLUSION AND DISCUSSION

This paper investigates the potential of using a metasurface along with an IR camera to image RF fields. Three metasurface elements are designed to have similar transmittance, reflectance, and absorptance for a 28 GHz, y-

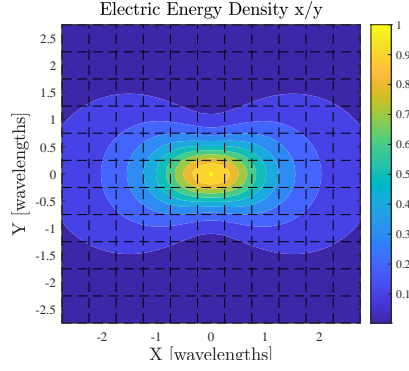


Figure 5: Tangential part (x and y components) of the electric energy density from a y-directed ideal electric dipole placed one wavelength below the center.

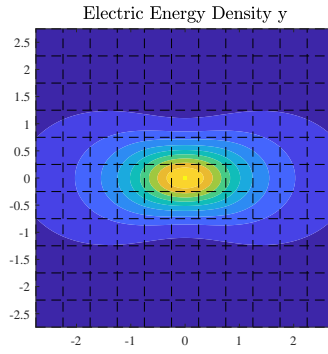


Figure 6: The y component of the electric energy density from a y-directed ideal electric dipole placed one wavelength below the center.

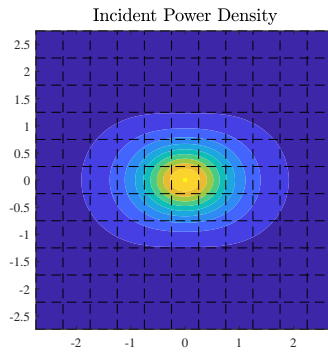


Figure 7: Incident power density in the normal direction from a y-directed ideal electric dipole placed one wavelength below the center.

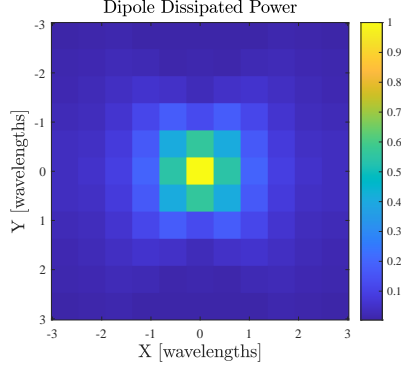


Figure 8: Dissipated power in each dipole element (see Figure 2a) of an  $11 \times 11$  element metasurface. The surface is illuminated by an ideal y-directed electric dipole placed one wavelength below the surface.

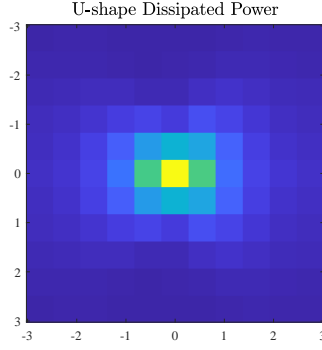


Figure 9: Dissipated power in each U-shaped element (see Figure 2b) of an  $11 \times 11$  element metasurface. The surface is illuminated by an ideal y-directed electric dipole placed one wavelength below the surface.

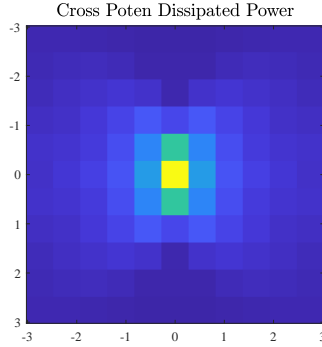


Figure 10: Dissipated power in each cross potent element (see Figure 2a) of an  $11 \times 11$  element metasurface. The surface is illuminated by an ideal y-directed electric dipole placed one wavelength below the surface.

polarized plane wave. Further, when adjusting the plane wave to x-polarized, the polarization purity is shown to significantly vary for the three metasurfaces.

The metasurface dissipated power from an ideal electric dipole source is shown to have similarities to the field under test. The scaling of the dissipated power on the elements more closely resembles the incident power density than the electric energy density.

Future work could investigate how, by changing the design of the metasurface, the dissipated power distribution can more closely resemble the field distribution of the device under test. Further, along with the shown example, more simulations of measurement setups are required to have a clearer picture of the design challenges. These findings could also be tested in a measurement setup with the IR camera. Finally, arbitrary sources and calibrations of the surface can be included.

#### REFERENCES

- [1] J. Lundgren, M. Gustafsson, D. Sjöberg, and M. Nilsson, “IR and metasurface based mm-wave camera,” *Applied Physics Letters*, vol. 118, no. 18, p. 184104, 05 2021. [Online]. Available: <https://doi.org/10.1063/5.0047315>
- [2] L. G. Gregoris and K. Iizuka, “Thermography in microwave holography,” *Appl. Opt.*, vol. 14, no. 7, pp. 1487–1489, Jul 1975. [Online]. Available: <https://opg.optica.org/ao/abstract.cfm?URI=ao-14-7-1487>
- [3] K. Muzaffar, L. I. Giri, K. Chatterjee, S. Tuli, and S. Koul, “Fault detection of antenna arrays using infrared thermography,” *Infrared Physics & Technology*, vol. 71, pp. 464–468, 2015.
- [4] K. Brown, “Far-field antenna pattern measurement using near-field thermal imaging,” *IEEE Trans. Antennas Propag.*, vol. 66, no. 3, pp. 1488–1496, 2018.
- [5] S. A. Kuznetsov, A. G. Paulish, A. V. Gelfand, P. A. Lazorskiy, and V. N. Fedorinin, “Bolometric THz-to-IR converter for terahertz imaging,” *Applied Physics Letters*, vol. 99, no. 2, p. 023501, 2011.
- [6] S. A. Kuznetsov, A. G. Paulish, M. Navarro-Cía, and A. V. Arzhannikov, “Selective pyroelectric detection of millimetre waves using ultra-thin metasurface absorbers,” *Scientific reports*, vol. 6, p. 21079, 2016.
- [7] K. Fan, J. Y. Suen, X. Liu, and W. J. Padilla, “All-dielectric metasurface absorbers for uncooled terahertz imaging,” *Optica*, vol. 4, no. 6, pp. 601–604, 2017.
- [8] J. Lundgren, T. Martin, H. Khalid, M. Zabihipour, D. Tu, I. Engquist, D. Sjöberg, and M. Gustafsson, “Real-time near-field mmWave measurements using screen-printed metasurfaces and IR camera,”

- TEAT Technical Report*, vol. 7282, pp. 1–26, 2024. [Online]. Available: <https://portal.research.lu.se>
- [9] K. Achouri and C. Caloz, *Electromagnetic metasurfaces: Theory and applications*. John Wiley & Sons, 2021.
  - [10] H.-H. Hsiao, C. H. Chu, and D. P. Tsai, “Fundamentals and applications of metasurfaces,” *Small Methods*, vol. 1, no. 4, p. 1600064, 2017.
  - [11] F. Boccardi, R. W. Heath, A. Lozano, T. L. Marzetta, and P. Popovski, “Five disruptive technology directions for 5G,” *IEEE Communications Magazine*, vol. 52, no. 2, pp. 74–80, 2014.
  - [12] (2022) FEKO. Altair. [Online]. Available: <https://altairhyperworks.com/product/Feko>
  - [13] B. A. P. Nel, A. K. Skriversvik, and M. Gustafsson, “Q-factor bounds for microstrip patch antennas,” *IEEE Trans. Antennas Propag.*, vol. 71, no. 4, pp. 3430–3440, 2023.
  - [14] J.-H. Deng, H. Xiong, Q. Yang, M. Suo, J.-Y. Xie, and H.-Q. Zhang, “Metasurface-based microwave power detector for polarization angle detection,” *IEEE Sensors Journal*, vol. 23, no. 19, pp. 22 459–22 465, 2023.



Doctoral Dissertation

No. 182

ISBN 978-91-8104-356-3 (print)

ISBN 978-91-8104-357-0 (pdf)

ISSN 1654-790X